UNIVERSIDAD MICHOACANA DE SAN NICOLÁS DE HIDALGO

INSTITUTO DE FÍSICA Y MATEMÁTICAS

Espectro total de energía de rayos cósmicos medido con el observatorio HAWC

TESIS

Que para obtener el grado de ***Doctor en Ciencias en el Área de Física***

Presenta:
M. C. Jorge Antonio MORALES SOTO

Director de tesis:
Dr. Juan Carlos ARTEAGA VELÁZQUEZ

Morelia, Michoacán. Agosto del 2025.

UNIVERSIDAD MICHOACANA DE SAN NICOLÁS DE HIDALGO

Instituto de Física y Matemáticas

Espectro total de energía de rayos cósmicos medido con el observatorio HAWC

por Jorge Antonio MORALES SOTO

Resumen

Este trabajo presenta la medición del espectro total de energía de los rayos cósmicos en la región de 10 TeV a 1 PeV, una de las regiones que han sido poco exploradas en las mediciones actuales del espectro de rayos cósmicos. El espectro se reconstruyó mediante el análisis de 5.3 años de datos del Observatorio HAWC (High Altitude Water Cherenkov), ubicado a gran altitud, medidos con ángulos cenitales de hasta 35°. El método de reconstrucción se basó en la técnica de deconvolución bayesiano, usando simulaciones Monte Carlo en el marco del modelo de interacciones hadrónicas de altas energías QGSJET-II-04. Uno de los resultados importantes de este trabajo es la confirmación de la presencia de un corte en el espectro de energía, cuya posición se estableció en $40.2 \pm 1.0(\text{stat.})^{+6.2}_{-6.4}(\text{sys.})$ TeV. Se observó que el cambio en el índice espectral es de $\Delta\gamma = -0.19 \pm 0.01$ (stat.) $^{+0.06}_{-0.07}$(sys.). Este estudio ofrece una contribución importante al conectar las mediciones de experimentos directos e indirectos, lo que es esencial para avanzar en la comprensión del origen, la aceleración y la propagación de los rayos cósmicos.

Palabras clave: HAWC, rayos cósmicos, espectro total de energía, método de deconvolución, chubascos atmosféricos extendidos de partículas.

UNIVERSIDAD MICHOACANA DE SAN NICOLÁS DE HIDALGO

Instituto de Física y Matemáticas

Espectro total de energía de rayos cósmicos medido con el observatorio HAWC

by Jorge Antonio MORALES SOTO

Abstract

This work presents the measurement of the total cosmic-ray energy spectrum in the 10 TeV to 1 PeV range, one of the regions with the one of the least explored regions of the spectrum in current cosmic-ray spectrum measurements. The spectrum was reconstructed by analyzing 5.3 years of data from the High Altitude Water Cherenkov observatory (HAWC), with zenith angles up to 35°. The analysis implements the Bayesian unfolding technique as the main reconstruction method, employing QGSJET-II-04 simulations. A key finding is the confirmed presence of a knee-like spectral feature, whose position was located at $40.2 \pm 1.0(\text{stat.})^{+6.2}_{-6.4}(\text{sys.})$ TeV. It is observed a variation in the spectral index $\Delta\gamma = -0.19 \pm 0.01$ (stat.) $^{+0.06}_{-0.07}$(sys.). This study makes an important contribution by connecting measurements from direct and indirect experiments, which is essential for enhancing our knowledge of the cosmic ray sources, their primary acceleration mechanisms, and how they travel across the Universe.

Key words: HAWC, cosmic rays, total energy spectrum, unfolding method, extensive air showers.

Auh néhuatl,
tlahtocani itlayohualiz,
tlauicani ipan xochmecacahuitl,
icone totli huehuenelhuayo,
tlaxochiocotl ic ilhuicapopoyecameh,
na nilhuicatlacatl itic yohualli.
-Pedro Martinez Escamilla, fragment from *TLAHTOCANI INCITLALHUAN*.

Y yo,
sembrador de la noche,
viajero en el tiempo,
hijo del sembradío de raíces antiguas,
ocote encendido por luciérnagas estelares,
centinela de la noche profunda.
Traducción al español por Pedro Martinez Escamilla.

Agradecimientos

Primero quiero agradecer a mi mamá y a mi papá por todo el apoyo, su infinita paciencia y esfuerzo por sacarme adelante. Se que no ha sido fácil para ninguno de ustedes y siempre estaré agradecido por todo lo que me han dado y han hecho por mi. Todo lo que soy se los debo a ustedes.

Dr. Juan Carlos Arteaga Velázquez, lo admiro y respeto mucho. Gracias a usted he alcanzado muchas metas y conseguido grandes logros. Muchas gracias por todo el apoyo durante estos últimos 10 años.

Un agradecimiento a la Dra. Karen Salomé Caballero Mora y a los Dres. Umberto Cotti Gollini, Cederik León de León Acuña y Humberto Martínez Huerta, integrantes de mi comité tutorial, por el tiempo dedicado a leer y revisar este trabajo, así como sus comentarios que ayudaron a mejorar el análisis. También un agradecimeinto especial al Dr. Adnan Bashir y a todos los maestros que tuve durante mis etapas de doctorado y maestría en el IFM.

A mi familia, quienes me apoyan a diario. Damian, tía Chayo y tío Obed, los quiero mucho. A la futura Dra. Carolina. Fany, Isai, Ali, Liam, Karen. A mi tía Martha y mi tío Germán, mi tío Toño y mi tía Gaby, mi tío Bertino y mi tía Pilar, Toñito, Vanessa, Rafita y Constanza, Jorge Iván y Kary, Gabrielito y Jorgito, Gabriel y Arantza, Germán y Aida, Juanito y Ceci, y Lalo. A mi tía Pupis y mi tío Alfredo, Selene, Mikol, Edgar, Frida y Anael. A mi tía Carmen y mi tio Baldo. A mi tío Teco, mi tía Laura, mi tía Chiri, Javi, Sofi y José. A mi tío Fidel y mi tía Paty, por la hospitalidad y las aventuras. A mi tio Robertinho. A mi primo JuanMa y toda la familia de Ixmiquilpan. Mis abuelitas y abuelitos. A los todos los Villas. A toda la familia Salomón en Hidalgo y el resto del país. Prima latosaaaaaaaaaaaaaaaaaa. Daisy, Haisser y Siler.

A mis amigos que siempre me han acompañado y apoyado: Kim, el Mike!, Rube, Aleeeeeeeeeeeeeee, Atziri, Manolooooooooo y Yunuen, Dulcesito, los Lauros (Fanita, Prima y Gera), Naila, Bosco y mi sobrino ahijado Esteban, Daniel Pellicer, Ceci y Teté, compa Iván, Iván y Dani, Itzayana, Sofi, Memo, Gonzalo, Misha, Gaby, Emilio, Richi, Jona, César, mis amiguitos del alma Juan e Izamar, Gus, Melanie, Venecia, Jeannine, Gabs, Leti y Gaby Fismat (aunque te enojes, Gaby Fismat), Thomai, Dra. Martha, Marcos, Kato, Michaele y Edgar. A mis amistades de HAWC, Sergio y Daniel, Tomás, Sara, Ibrahim, Paolo, Juan Carlos, Yunior, Ana.

Los que llevan aún más tiempo aguantándome, mis hermanos del alma, Nestor y Abraham. Y a quienes llevan un poco menos de tiempo aguantándome pero igual los quiero un montón, Erick, Zhava y el Sante.

A toda la colaboración de HAWC.

Por último, quiero agradecer a SECIHTI (antes CONACYT) y a la Coordinación de la Investigación Científica de la Universidad Michoacana por el apoyo brindado.

Contenido

List of Abbreviations

AGN	**A**ctive **G**alactic **N**uclei
asl	**a**bove **s**ea **l**evel
DAQ	**D**ata **A**c**q**uisition
EAS	**E**xtensive **A**ir **S**howers
FEB	**F**ront **E**nd **B**oard
FOV	**F**ield **O**f **V**iew
GRB	**G**amma **R**ay **B**urst
HAWC	**H**igh **A**ltitude **W**ater **C**herenkov observatory
IACT	**I**maging **A**ir **C**herenkov **T**elescope
ISM	**I**nter**s**tellar **M**edium
PE	**P**hoto**e**lectron
PMT	**P**hoto**m**ultiplier **T**ube
QCD	**Q**uantum **C**hromo**d**ynamics
RPC	**R**esistive **P**late **C**ounter
SBG	**S**tar**b**urst **G**alaxy
SNR	**S**uper**n**ova **R**emnant
TDC	**T**ime **D**igital **C**onverter
ToT	**T**ime **o**ver **T**hreshold
TS	**T**est **S**tatistic
VHE	**V**ery **H**igh **E**nergy
WCD	**W**hater **C**herenkov **D**etector

Dedicado a mi mamá y a mi papá,
mi abuelita y mi tía Mara,
mi familia,
y mi familia extendida: mis amigas y amigos.

Introduction

The all-particle energy spectrum of cosmic rays has been a subject of research due to its relation with the origin, acceleration, and propagation of this radiation [1–4]. In particular, the energy region between 10 TeV and 1 PeV has gained increasing interest over the years because it represents the overlap region for direct and indirect cosmic-ray observations. However, it remained poorly explored due to technological limitations in both methods.

The soviet program of the PROTON satellite series [5] started the exploration of this energy region in the 1960s. As part of these missions, the Proton-4 satellite [6], launched on November 1968, analyzed the all-particle cosmic-ray energy spectrum for energies between 300 GeV $\leq E \leq$ 1 PeV [6]. These results led the way for other direct experiments to further explore the energy spectrum of TeV cosmic rays, like the balloon-borne detectors ATIC [7], CREAM-II [8], MUBEE [9], JACEE [10], and RUNJOB [11], and the satellite mission SOKOL [12]. The data collected by these experiments in the TeV region suffers from large uncertainties due to statistical limitations. For detailed studies on the properties of cosmic rays with energies within 10^{13} eV $\leq E \leq 10^{15}$ eV, better statistics and lower systematic errors are needed. More recent direct detectors, like the satellite-borne experiment NUCLEON [13], have measured the energy spectrum of TeV cosmic rays with reduced statistical fluctuations.

Complementary to the direct measurements, there are indirect experiments dedicated to the observation of the spectrum around the knee covering the TeV region. Some of the early contributions of indirect cosmic-ray data in the TeV region were provided by Tien-Shan [14] and BASJE [15]. While indirect measurements offer better statistical precision than direct methods, their interpretation depends on hadronic interaction models, which are used for reconstructing data from earlier EAS experiments, like Tien-Shan and BASJE, are now considered outdated.

Recent technological and theoretical advances have led to the current generation of cosmic ray experiments, that contribute to reduce the gap between direct and indirect cosmic ray spectrum measurements in the 10 TeV $\leq E \leq$ 1 PeV range, with meaningful data comparisons. This experiments include satellite experiments such as NUCLEON [13] and DAMPE [16–18], and ground-base observatories like HAWC [19] and LHAASO [20], among others (see Fig. 1).

In particular, HAWC was designed for observing both gamma rays and cosmic rays, with a strong sensitivity to TeV cosmic rays. In 2017, a study of the all-particle cosmic-ray energy spectrum using HAWC data, between 10 TeV and 500 TeV, revealed a softening at 45.7 ± 1.1(stat) TeV, indicating a variation in the spectral index [22]. This scenario was later supported by NUCLEON with the observation of a softening at TeV energies [23]. To this date, the source of such spectral softening remains a mystery. Current experimental evidence from direct and indirect measurements suggests a correlation between the softening in the total spectrum and the presence of individual cutoffs observed in the proton and helium nuclei spectra at similar energies [23–26]. The first evidences of these structures came from the balloon-borne experiment CREAM-III data [27], and further observations made

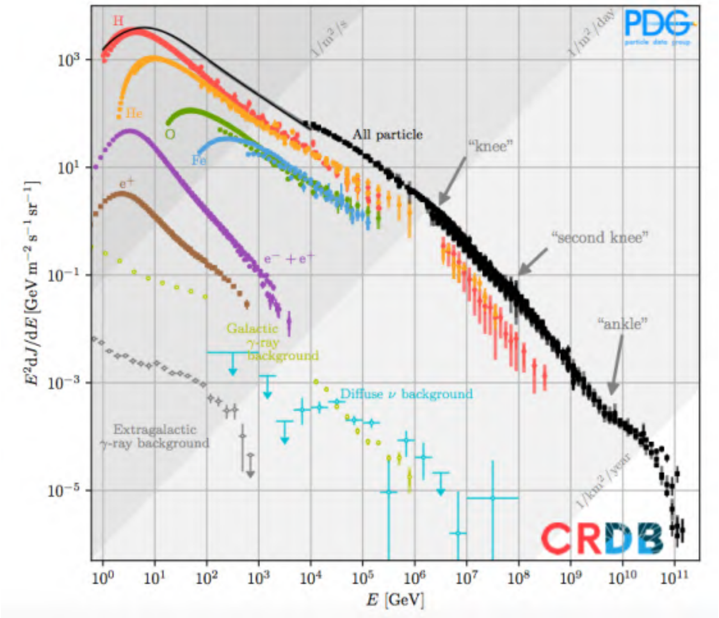

FIGURE 1: The all-particle energy spectrum and the individual elemental groups of cosmic rays are displayed in this graph. Also shown, the measurements of the intensity of charged and neutral particles. *Image source:* [21].

by ATIC-2 [7] and NUCLEON [24] supported such results. More recently, the direct measurements made by DAMPE [28, 29], NUCLEON [23] and CALET [30, 31] confirmed these steepenings in the light mass cosmic-ray components.

Cosmic-ray models, such as the one described in [32], propose that galactic cosmic rays up to PeV energies originate from violent galactic events like supernova explosions [33]. These models suggest that diffusive shock acceleration within the remnants of these supernovae (SNRs), potentially influenced by non-linear effects [34], is the primary mechanism for their origin [35–38]. After acceleration, these particles escape from the source and travel diffusively through the interstellar space, bouncing around as a result from the interactions of the cosmic rays with the Milky Way magnetic field [39–41]. All these models predict a flat cosmic ray spectrum across the TeV energy range. Thus, the presence of softenings in the total and light spectra of cosmic rays invites to revisit the current theories about this radiation, and also motivates further investigation with existing and future experiments. More intricate scenarios are needed, potentially incorporating: additional mechanisms at the production stage [42], different propagation effects [43, 44], and the possibility of multiple populations of cosmic ray sources [45–47].

The combined data from direct and indirect experiments provide crucial constraints for theoretical models of cosmic ray acceleration and propagation. Thus, the comparison between cosmic-ray data from direct and indirect experiments is essential to understand the nature of cosmic rays with energies within 10^{13} eV $\leq E \leq 10^{15}$ eV. In addition, this process helps to detect and understand any systematic uncertainties that might be present in either techniques, identify areas of improvements for the design of future experiments, cross-check the results from both techniques and increase confidence in the detailed measurements of the spectrum of TeV cosmic rays. Recognizing the importance of continuous improvement, driven by advancements in data analysis and the release of updated high-energy hadronic interaction models like QGSJET-II-04 [48], the HAWC collaboration is committed to updating its experimental simulations [49] and energy spectrum analysis. These updates motivated the present work, which revises and improves the study of the all-particle cosmic-ray energy spectrum measured with the HAWC observatory. In comparison to [22], this analysis

1. Employs an updated set of simulated data that include a description of the performance of the PMTS in HAWC and its effects in the reconstruction of the energy spectrum. The implementation of this simulations in the analysis helped to reduced the experimental systematic errors in comparison with [22]. In addition, this new MC simulations were produced with QGSJET-II-04[1], which is another advantage in comparison with the study of [22], where a previous version of QGSJET-II-04 was used. In addition, the new simulations.

2. Uses 5.3 years of HAWC data with zenith angles $\theta \leq 35^\circ$ for the analysis of the energy spectrum. In [22], 7.7 months of data with $\theta \leq 16.7^\circ$ were analyzed. The larger data sample increases the statistics in the final result, while the increase in the zenith angle range reduced the bias for the events with energies $E \geq$ 500 TeV due to saturation effects in the PMT.

3. As in [22], this study also employs the Bayes unfolding as the primary reconstruction method for the total energy spectrum [50–52].

Although the cosmic ray events measured with HAWC are reconstructed with energies up to 1.4 PeV, the previous result reported in [22] was shown up to 500 TeV due to large systematic uncertainties above $E > 10^{5.5}$ TeV caused by reconstruction effects and saturation in the PMTs. The improvements mentioned in the points 1 and 2 helped to reduce the systematic errors that affected the reconstruction of the energy spectrum at the highest energies, thus allowing to extend the analysis of the total energy spectrum measured with HAWC up to 1 PeV.

The structure of the present doctoral thesis is as follows: Chapter 1 summarizes the relevant historical background on cosmic rays, as well a description of the state of art on the field, while Chapter 2 covers the phenomenon of extensive air showers (EAS), how are they produced and how do they propagate through the atmosphere. Chapter 3 explores the experimental methods employed in cosmic ray research, as well as the description of some relevant detectors. Chapter 4 focuses in the HAWC Observatory, its instrumental characteristics, operations, main results, and the characteristics of the HAWC data as well as simulations employed in the present work. The reconstruction method of the energy spectrum is presented in detail in Chapter 5, and the unfolded spectrum obtained in this work is presented in Chapter 6, along with an analysis of the systematic uncertainties of the spectrum. The statistical and systematic analyses implemented to study the shape of the unfolded result are described in Chapter 7. Chapter 8 is dedicated to the discussion of the results obtained in this work, which includes a comparison of the HAWC spectrum with data from other experiments, and a review of potential physical models that provide new scenarios for the production of the recently discovered softening in the spectrum of TeV cosmic rays. To conclude this study, the final remarks and future work are presented in Chapter 9.

---

[1] QGSJET-II-04 is a post-LHC hadronic interaction model.

Chapter 1

Cosmic rays: historical background and physics models

Cosmic rays were officially discovered by the Austrian physicist Victor Hess more than 100 years ago when he reported the existence of a highly energetic type of *extraterrestrial radiation* coming outside of the atmosphere [53]. Ever since then, this unique type of radiation has been under the eye of scientists around the world due to the mysteries that surround its origin, production, and propagation in space. Throughout history, the exploration of cosmic rays has been shaped by influential scientists, contributing to its status as a multidisciplinary field of study.

This chapter outlines the most relevant milestones in the evolution of cosmic ray studies and offers a brief review of the state of art of the field.

1.1 Early studies

By the late XIX century, Charles de Coulomb, pioneer for its studies on the electrical properties of charged bodies, and Sir Charles Vernon Boys, known for the development of innovative experimental devices[1], observed, independently, a phenomenon related to metallic conductive bodies surrounded by air. In this particular case, it was observed that these objects were subject to an electrical discharge, even under controlled isolation conditions [54–56].

A clear example of this effect could be observed through an electroscope, a device employed to detect and quantify the electric charge on an object. The most common configuration of an electroscope involves a glass container housing a pair of metallic plates suspended from a metal bar standing out from the container, with insulation between the bar and the container. However, even under optimal conditions in which the loss of charge can be nearly eliminated, this device can't hold a charge forever. A challenging scenario, since a body with an electrical charge must retain it if it is isolated. Early attempts to explain this phenomenon were through the atomic properties of matter. Atoms were known to be neutral, unless ionized by loosing electrons. For example, a gas, such as air, is said to be ionized when its atoms lose electrons, becoming positively charged molecules (called ions). In addition, the free electrons may attach to other molecules, forming negative ions. It was proposed that the discharge effect observed in the metallic plates could be explained by the constant ionizitation of the air inside the electroscope could explain. Therefore, negative (positive) ions will be attracted to a positively (negatively) charged plate, causing their discharge. This effect was thoroughly explored with different

---

[1] For example, the radiomicrometer for measuring the discharge rate of charged objects

experiments and approaches, and encouraged the development of different theoretical approaches in the spirit to describe the behavior of ions in air and to determinate their source. Also, the observed discharge of electroscopes led to the creation of more sophisticated experimental devices, like the electrometers, in order to make more precise and reliable measurements of air conductivity.

The conductivity of the air became an active field of study by the end of the XIX century, lead by prominent contemporary scientists like the Scottish physicist C. T. R. Wilson, and the German physicists H. F. Geitel and J. Elster. In particular, J. Elster and H. F. Geitel, who were skilled experimentalists, inventors, and pioneer investigators in atmospheric electricity, made contributions in air ionization. In 1900, the experimental evidence produced by Elster and Geitel proved that air is an electrical conductor and the ionization of the atmosphere, which they assumed was due to the radioactivity[2] [58]. It was known by then the ionizing capabilities of radioactivity in gases. The idea of an ionizing radiation responsible for the air ionization was supported by Travis Rimmer and Heinrich Mache, who, in the summer of 1906, discovered that the intensity of the ionizing radiation fluctuated according to weather conditions [56]. The observations made by Rimmer and Mache provided strong evidence that the ionization in the air was probably due to radioactive substances in the environment, eventually leading to a better understanding of natural radioactivity and its role in atmospheric phenomena [56].

Another contemporary physicist whose research focused on atmospheric electricity and the radioactive releases from the soil, was Hermann Ebert [59]. He was pioneer in the measurement of ions at high altitudes and it is believed to be the pioneer of balloon-borne experiments for this purpose [56]. All of these studies led scientists to develop the hypothesis that the ionizing radiation had a terrestrial origin. Under this assumption, the effects of the radiation would be stronger near Earth's crust and decrease with altitude, as it was expected to be attenuated in the air. Mache continued his studies and later on stated that the ionizing radiation was made by one part coming from natural radioactive elements present on the superficial layers of the terrestrial crust, and a second contribution from the decay of atmospheric radioactive elements [56], after discovering seasonal fluctuations in a year cycle.

Following the spirit of the trending line of research, Arthur Stewart Eve proposed that due to the larger concentrations of radium in Earth crust relative to ocean water, the ionization levels observed over solid ground should be greater than at the surface of the ocean [60]. By 1899, one of E. Stwewart colleagues, the new zealander physicist Ernest Rutherford, had already discovered α and β particles as capable of ionizing gases, such as air [61], and later in 1900, Paul Villard discovered gamma rays [62], the most penetrating type of radiation known by then [63].

Theodor Wulf created an advanced and precise electroscope (see fig. 1.1) in comparison to the available models at the time. With this instrument, Wulf performed several measurements of the ionizing radiation across Europe, specifically in Belgium, Germany, and The Netherlands [56, 64]. In particular, in 1908, along with Albert Gockel, Wulf observed the ionizing intensity with two of his electroscopes at the Alps, at observation levels that ranged from 600 m to 3000 m [63]. The measurements from the electroscope showed no variation with altitude, which led them to the conclusion that the radioactive substances in the Earth's crust [65] were responsible for the production of the radiation. Moreover, from the Eiffel tower, Wulf made several measurements with the goal to demonstrate that the ionizing radiation decreased with altitude and, in consequence, confirm that it was originated

---

[2] Discovered by Henri Becquerel in 1896 [57].

FIGURE 1.1: The electroscope developed by T. Wulf was considered by his contemporary colleagues as a state of the art instrument. Its designed featured two quartz fibers for the measurement of the ionizing radiation. [64]. *Image source:* [66].

at the upper layers of Earth crust. However, his observations diverged from this hypothesis [56]. The fact that the radiation, considered mainly as gamma rays, at the top of the tower was reduced by $\sim 50\%$ in comparison to the measurements at ground level was in tension with the hypothesis of the ionizing radiation emerging from Earth's upper layer, and of the ionizing radiation. His findings derived into two possible scenarios: another source of radiation may exist in the atmosphere, or a lower-than-anticipated absorption coefficient for ionizing radiation in air.

1.2 Air balloon flights: early stages

As mentioned before, to demonstrate the veracity of the hypothesis that the ionizing radiation was produced by the radioactivity of the soil, many scientists developed novel experimental devices and techniques for this purpose. Probably one of the most relevant techniques are the balloon-borne measurements, which played a decisive role in the discovery of cosmic rays.

According to the records [56], the first balloon-borne measurements of the ionizing radiation phenomena were carried out by Hermann Ebert. In particular, between 1900 and 1901, H. Ebert performed 3 ballon-borne missions, and from the measured data he reported that the altitude and the weather can influence the rate of discharge. The measurements were taken at altitudes up to 3,700 m.

Between September 1900 and August 1903, the meteorologist and geologist Franz Linke conducted twelve balloon flights at high altitudes, six of which were made to measure the ionizing radiation with an electrometer provided by Elster and Geitel. His findings, widely unrecognized, showed that the ionization levels between 1000 m and 3000 m altitude were similar or greater than at ground level, and the amount of ionizing radiation increased significantly at 5500 m [63, 67]: *"Would one compare the presented values with those on ground, one must say that in 1000m altitude, where the measurements in general began - the leakage (ionisation) is smaller than on ground. It is between 1 and 3 km of the same amount, and above larger than on Earth, with values increasing up to a factor of 4 (at 5500 m altitude), if the mean value at our latitude is 1.5%. The uncertainties of the observations .... only allow the conclusion that the reason of the* *ionization has to be found first in the Earth"*[3]. This was probably the first evidence on how the ionizing radiation intensity increased with altitude, however his work was unnoticed by the contemporary scientists of Linke, and to the date his work is rarely mentioned.

Another pioneer in balloon-borne experiments was the German physicist Albert Gockel who dedicated his carrier to the study ionizing radiation phenomena. In particular, Gockel employed the balloon-borne technique [68]. On December 11, 1909, Gockel took off on his first balloon flight, equipped with a Wulf-electrometer, and reaching a maximum altitude of $4,500$ m approximately [68]. At low altitudes, near the ground, the data measured by Gockel was consistent with the theory that the radiation had a terrestrial origin, i.e, the intensity of the radiation was greater at ground level than at air; however, at greater heights, he noted an unexpected radiation increase, but the later was ruled out due to possible errors at the moment of the measurement [69].

Motivated by his first flight, Gockel conducted a second flight later in 1910, but this time the maximum altitude of the flight was 2000 m approximately [68]. The results gathered were consistent with his previous observations, to which Gockel concluded that [68]: *"an influence of the altitude on the ionization in the closed vessels was not seen. It can be concluded that cosmic radiation if it exists at all, can only be a negligible part of the penetrating radiation"*[4].

1.3 Discovery of cosmic rays and early years of research

On a different approach, the Italian physicist Domenico Pacini performed measurements on the ground, and on top and above the ocean to demonstrate the origin of the ionizing radiation [56, 70]. In 1910, Pacini conducted his first measurements below the water level at the Golfo Ligure [56]. The detectors were placed three meters under the surface. With this study Pacini inferred that the water layer absorbed the radiation from the Earth ground. Later in 1911, on board of a ship, Pacini measured the ionizing radiation on top of the ocean surface, expecting to find a smaller ionization rate than on ground. However, the measurements were consistent regardless of whether it was measured on ground or above the sea far from land. These results led Pacini to assume the presence of another source of the ionizing radiation within the air [56, 71], independent from the Earth crust contribution to this radiation.

Eventhough Theodor Wulf, Albert Gockel, and Domenico Pacini were firm believers of the terrestrial radiation hypothesis, their studies hinted the origin of this radiation somewhere else. These observations paved the way to the eventual discovery of the component of the cosmic radiation that we know today as *cosmic rays*, by Victor Hess in 1921, earning him the Nobel Prize from the Royal Swedish Academy of Sciences in 1936.

Victor Franz Hess was an Austrian physicist and Nobel Prize laureate, born on June 24, 1883, in the city of Styria, Austria. At the University of Vienna (under the advice of the Professors Franz Exner and Egon von Schwiedler) Hess developed an interest in the fields of radioactivity and atmospheric electricity. In 1910, Victor Hess got a position at the Institut fur Radiumforschung of the Austrian Academy of Sciences as an assistant of Stefan Meyer [56].

Later, in 1911, Victor F. Hess decided to perform ballon-borne measurements of gamma-ray radioactivity and its absorption coefficient in the atmosphere. For his

---

[3] Translated fragment taken from [63]

[4] Quote translated from German.

FIGURE 1.2: Photograph of Victor Hess dating to 1911. He is on board of one of his famous balloon-borne expeditions. *Image source:* [76].

observations, Hess employed [72]: "*two Wulf radiation detectors with three-millimeter thick walls, perfectly sealed and able to withstand all pressure variations during the ascents, for the observation of the penetrating radiation*". After his first observations, Hess identified variations between the experimental data and theoretical models. Motivated by his first flight (see fig. 1.2), Hess performed a series of 7 ballon flights during day and night throughout 1912. In particular, during a solar eclipse on April 17th, Victor Hess performed a balloon flight where he ascended to a maximum altitude of 2,750 meters. He determined that the radiation intensity levels were independent of the solar eclipse, thus excluding the Sun as the main main source of this ionizing radiation. In addition, Hess observations at the 2,000 m provided evidence that the radiation was higher than at sea level. On August 7, 1921, V. Hess repeated his observations on a balloon flight during a solar eclipse. This time, Hess reached a maximum altitude of 5,3000 m approximately. Convinced by the results of this and previous flights, Hess concluded the ionizing radiation increases as a function of the altitude [72]: "*The results of the present observations seem most likely to be explained by the assumption that radiation of very high penetrating power enters from above into our atmosphere, and even in its lowest layers causes part of the ionization observed in closed vessels*". In addition, from his results between day and night measurements, Hess discovered no significant differences [72–75].

To confirm Hess' results, the German physicist Werner Kolhörster made a several balloon-borne measurements between 1913 and 1914, Kolhörster also found that the intensity of the air ionization is a function of the altitude, becoming larger at the upper layers of the atmosphere. With his flights, Kolhörster hit the $9,300$ m a. s. l. mark, surpassing the altitudes reached by Hess [77].

On the other hand, contemporary scientists like the American physicist Robert Andrews Millikan were opposed to the idea of an *extraterrestrial radiation*. Instead, Millikan supported the hypothesis of radioactive substances of the air that produced radiation. Determined to prove his idea, Millikan set up electroscopes at varying depths up to 27 m inside the Mauir Lake and the Lake Arrowhead, both in California, USA[5]. Millikan conducted the experiment along with H. Cameron. They shared the objective to observe the variations in the radiation intensity at different water depth and altitude, thereby determining the origin of the ionizing radiation. They found that the electroscope discharge rate continuously decreased as the detectors were lowered deeper into both lakes [56]. Moreover, after correcting for the altitude difference between both lakes, the ionization rates recorded at both sites matched with each other. From these observations, Millikan and Cameron stated the following [78]: "*within the limits of observational error, every reading in Arrowhead lake corresponded to a reading 6 feet (1.8 m) farther down in Muir Lake, thus showing that the rays do come in definitely from above and that their origin is entirely outside the layer of atmosphere between the levels of the two lakes*". Convinced by his own experimental data, Millikan introduced the term *cosmic rays* [79] and accepted the presence of the cosmic radiation.

The charged nature of cosmic rays was proven in 1927 with the independent studies from the Russian physicist Dimitry Skobelzyn, and Bothe and Kolhörster. First, Skobelzyn analyzed the traces produced inside a cloud chamber, and determined these were induced by the passage of cosmic rays[80, 81]. Later, Bothe and Kolhörster that the influence of a magnetic field curved the traces left by cosmic rays [56, 82].

Later in 1930, the Italian physicist Bruno Rossi, based on the charged properties of cosmic rays, proposed a model of a geomagnetic effect. This model predicted that the flux of positively (negatively) charged cosmic rays would be greater from the West (East) in comparison with the East (West) direction [83]. This effect was confirmed by the experimental observations made by Arthur Compton and Luis Alvarez [84], and Thomas Johnson [85], respectively. These studies prove a dominant abundance of positively charged cosmic rays.

1.3.1 A new window for cosmic-ray observations: the Extensive Air Showers

The studies of air ionization measurements were significantly improved after the creation of a counting tube by Hans W. Geiger and W. Müller on July 7, 1928 [56, 86]. This new experimental device also had an impact on the designed and development of coincidence counting systems [56], and therefore, may scientists quickly adopted the counting tubes to their experimental set ups. In particular, B. Rossi often referred to the Geiger-Müller counter tubes as [83, 87]: "*an open window to a new and unknown territory, with unlimited opportunities for exploration*". Rossi employed coincidence counters for cosmic ray studies at high altitudes, like the experiment that he conducted in Eritrea, Italy, at 2,370 m a.s.l., during the fall of 1933. Even though his results were highly unnoticed by his contemporaries, his observations revealed the existence of a new phenomenon [83]: "*very extensive showers of particles*". Another contribution to the cosmic-ray field of study made by Rossi is the discovery of the *hard* and *soft* components of the cosmic radiation at ground level. The hard component is capable of penetrating a meter of lead, and Rossi identify it as muons. On the other hand, the soft component has a less penetrating power and can be stopped by a layer of dense material. This component is composed by gamma rays and $e^{\pm}$.

The observation of the extensive shower phenomena was confirmed by W. Kolhöster and Pierre Auger with independent experiments in 1938. With a setup of two

---

[5] Both lakes are located at an altitude of $3,540$ m a.s.l. and $1,530$ m a.s.l., respectively.

particle counters positioned 10 meters apart from each other, Kolhöster made the observation of a *shower* of secondary particles [88].

Later in 1938, motivated by the studies of Rossi on the hard and soft components of the cosmic ray radiation, Auger conducted and experiment to measure these components. The experimental set up consisted on an array of coincidence counters placed several meters apart ($\mathcal{O}(300)$ m). From the observations made in the particles counters, Auger and his team proposed the existence of extensive air showers[6] (EAS), and they speculated that this phenomena could extend for several hundreds of squared meters and were produced at higher altitudes [89]. In addition, Auger developed a method to calculate the primary cosmic-ray energy based on the lateral widespread of the shower secondary particles. The larger the distribution, the more energetic the primary particle was likely to be.

Nowadays, the pioneer constributions from B. Rossi and W. Kolhöster are recognized, however many authors still point P. Auger as the responsible for the discovery of the EAS. Without a doubt, this discovery is a cornerstone in the study of TeV and PeV cosmic rays. The EAS detection technique has been also applied to study astrophysical gamma rays from the sky. Gamma-rays are produced by two mechanisms, lepton emission and hadronic interactions. Hence, their study can reveal the source of cosmic rays. In 2021, the HAWC collaboration detected gamma rays with energies reaching at least 200 TeV emanating from the Cygnus Cocoon, a superbubble of massive star formation [90]. This analysis suggests that these high-energy gamma rays have an hadronic origin, i.e., they could be produced by cosmic rays with energies in the PeV range. In addition, this observations provide first evidence of cosmic ray production inside the regions of star formation. Later, in 2024, the LHAASO collaboration also reported the observation of an ultrahigh-energy gamma-ray bubble within the Cygnus X region [91]. Based on their analysis of this region, the authors propose the observation of a source of cosmic rays in the central region that accelerates protons to energies beyond 10 PeV and injects them into the surrounding medium, i.e. what is called a PeVatron.

Up to this point, the most iconic keystones and historical figures relevant in the discovery of cosmic rays. The present thesis doesn't intend to make a deeper analysis of the history of cosmic rays. For further details, the readers can refer to [56, 64, 83, 86, 92, 93] for additional information on cosmic-ray studies and related topics.

1.4 Cosmic rays

To this day we don't have full knowledge of the properties of this type of radiation. Where are cosmic rays produced? How are they accelerated? and how do they propagate in the universe remain as open questions. Thanks to observations made by Fermi-LAT we know that TeV cosmic rays can originate in SNRs [94]. More recently, the HAWC collaboration and the LHAASO collaboration reported evidence of a PeVatron inside the Cygnus that can potentially accelerate cosmic rays up to PeV energies [90, 91]. The energy spectrum of cosmic rays is extremely dependent on their acceleration and propagation mechanisms as well as the sources [95, 96]. Thus, the meticulous and detailed study of the spectrum is a key factor in the development and testing of the theoretical models that try to explain the origin, propagation, and acceleration of cosmic rays. Another key property of cosmic rays is their mass composition, which can provide insights on their source properties and the medium around it [97]. In addition, this type of radiation are essential to investigate

---

[6] At the time, Auger was unaware of the previous studies conducted by Rossi and Kolhöster.

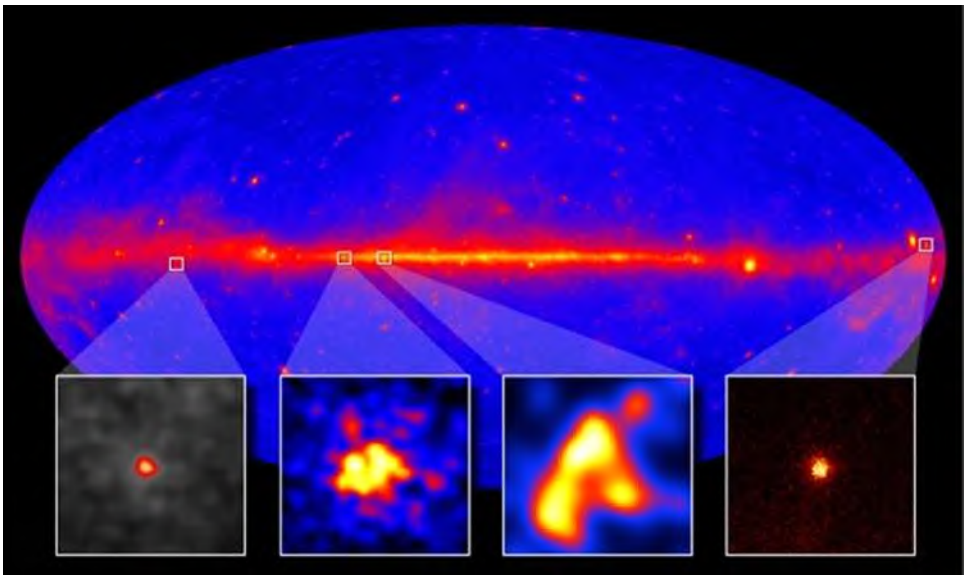

FIGURE 1.3: Gamma-ray sky map from Fermi-LAT data for energies between 50 MeV and 1 TeV. The location of four SNR's which are potential cosmic ray sources are also shown. The images of such SNR's are shown at the bottom. From left to right we have Cassiopeia A, W51C, W44, and IC443. The data was collected with Fermi's Large Area Telescope [94]. *Image source:* NASA/DOE/Fermi LAT Collaboration.

the physics of the high-energy processes that occur inside the galaxy. However, it is difficult to determine the sources of this radiation, due to their charged nature and to the fact that their trajectories are deviated by the influence of the magnetic fields throughout the interstellar medium (ISM). For this aim, the searches of cosmic-ray sources must be complemented with other astronomical windows.

In addition to cosmic rays, there are other types of radiation produced at the sources, e.g. neutrinos and gamma rays [95, 96]. These other particles travel in straight lines, and can also help to locate the sources of cosmic rays.

Thus, the observation of high-energy neutrinos, gamma- and cosmic-rays can offer new insights about accelerators of cosmic rays [96]. It is possible that these sources can be galactic (e.g. SNR [98]) or extragalactic (e.g. active galactic nuclei (AGN's) [99–101]). A discussion on possible galactic and extragalactic sources is given in section 1.6.

1.4.1 Energy spectrum of primary cosmic rays

Cosmic rays can be considered as a type of radiation with an extraterrestrial origin. Such radiation consists of neutrons, charged particles in general, e.g. electrons, antiparticles, and atomic nuclei. These particles, as they move across the ISM, can strike our atmosphere and can be categorized as primary and secondary cosmic rays depending on whether or not they had any type of interaction before arriving on Earth. Primary cosmic rays can be defined as those high-energy particles that are accelerated at astrophysical sources (E.g. supernova remnants, among others), like electrons and nuclei of different chemical elements as H, He, C, N, O, and Fe, all of which originate from nucleosynthesis processes inside stars. In contrast, particles and atomic nuclei that originate from the interaction between a primary and the

ISM (for example, interstellar gas) or our atmosphere are considered as secondary cosmic rays. Some of the secondaries are scarce products from the nucleosynthesis processes from the stars. Some examples are Li, Be, and B [96]. Antiprotons and positrons are considered as secondary cosmic rays, and whether these particles are produced at primary sources still remains an open question [96]. From the detailed study of the primary and secondary components constrains can be made on models about the origin, acceleration mechanism, and propagation of such radiation. One of the cosmic-ray properties that is important to measure and to study is the differential intensity, which describes how many particles reach a detector per unit area, energy interval, dΩ (solid angle of detection in sr), and time unit. Sometimes it is called the *energy spectrum* and is typically expressed as a function of the *energy per particle [E], energy per nucleon [E/A],* or *rigidity* [R] [102]. In the international system, the differential intensity has units of $[\mathrm{m}^{-2}\,\mathrm{s}^{-1}\,\mathrm{sr}^{-1}\,\epsilon^{-1}]$. In the later, ϵ corresponds to the unit measurements of E, E/A, and R, respectively.

Based on experimental measurements, the total spectrum of cosmic rays represents the sum of all individual nuclear spectra which extends from a few MeV up to several tens of EeV, and it is characterized by a power law

$$dN/dE \propto E^{\gamma}, \tag{1.1}$$

where γ corresponds to the spectral index and takes an approximate value of -2.7. This behavior of the total energy spectrum can be observed in Fig. 1.4 (left).

The energy spectrum has several prominent structures produced by important changes in the spectral index (see Fig. 1.4, right panel). These feature are:

Spectral feature	Position
Knee [103]	3×10^{15} eV
Low energy ankle [104]	2×10^{16} eV
Second knee [104]	1×10^{17} eV
Ankle [95, 105–107]	3×10^{18} eV

Thus, the spectrum of cosmic ray has small differences in the spectral index, γ, at different energy regions. Below the "knee," the spectrum has power law behavior with a spectral index $\gamma \approx -2.7$. It steepens to $\gamma \approx -3.1$ after the knee, and it becomes even steeper beyond the "second knee", $\gamma \approx -3.2$. After the "ankle", γ returns to approximately $\gamma \approx -2.7$ [105, 108].

The results from different air-shower experiments [109–114] indicate that the *knee* structure is due to a cutoff in the spectrum of light nuclei of cosmic rays [75]. EAS data also show that the second knee may be correlated to a cutoff in the iron nuclei energy spectrum. The *knee* and *second knee* seems to have their origin in a Peter's cycle derived from the efficiency loss at the source (or the galaxy) to confine the particles. Under this hypothesis, for each mass component of the PeV cosmic rays, the corresponding energy spectrum is expected to present a knee-like structure, which

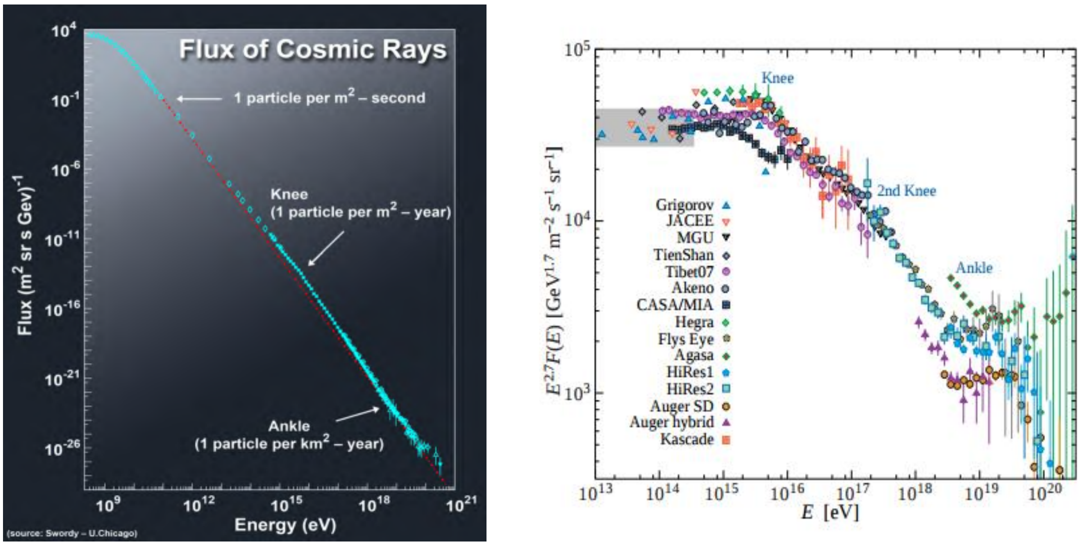

FIGURE 1.4: Left panel: All-particle cosmic energy spectrum as a function of the primary energy. It is observed that the spectrum decreases following a power law. In particular, low-energy cosmic rays, $E \sim 10^{11}$, eV arrive at Earth with a rate of 1 particle per m^2 per second, while at $E \sim 10^{15}$ eV the flux of cosmic rays $E \sim 10^{15}$ drops to 1 particle per m^2 per year. At the ultra high-energy regime, 10^{18} eV, the intensity corresponds to 1 particle per km^2 per year. *Image source:* [118]. *Right panel:* The energy spectrum of cosmic rays exhibits several structures at different energy regions: the *knee* (3×10^{15} eV), the *second knee* (1×10^{17}) and the *ankle* (3×10^{18}), among others. It is common to multiply the spectrum by a scale factor to highlight these features [102], in this case by $E^{2.7}$. *Image source:* [119].

is proportional to Z·E$_{knee}$ [115]. Here, E$_{knee}$ has an approximate value of 3×10^{15} eV [109], and the electric charge is represented by Z. This model is in agreement with the cosmic-ray data from the *KASCADE* [109] and *KASCADE-Grande* [111, 116, 117] experiments.

1.5 Cosmic ray primary composition

The chemical composition of the primary cosmic rays also holds insights about the production sites and its surroundings, and the relative abundance of the cosmic ray nuclei has an important roll in the formulation of propagation models. Given the advantages of direct cosmic-ray experiments, mass-composition measurements with these instruments enable the reconstruction of the energy spectra for different primary nuclei. For example, ATIC-02 [7], CREAM [120], PAMELA [121], AMS [122], PROTON [6], NUCLEON [23], DAMPE [18], CALET [31] have provided direct measurements of the spectra for primaries from protons up to Fe nuclei in different intervals below 1 PeV. For indirect cosmic-ray experiments, the composition studies of cosmic rays depend of comparisons of the data with the predictions of the hadronic interaction models. Such dependence introduce limitations in mass composition studies, which can only be done on a statistical basis. A further consequence is that the energy spectra is determined for elemental mass groups. This way, indirect experiments, like KASCADE [111], KASCADE-GRANDE [117], AUGER [89, 123], and

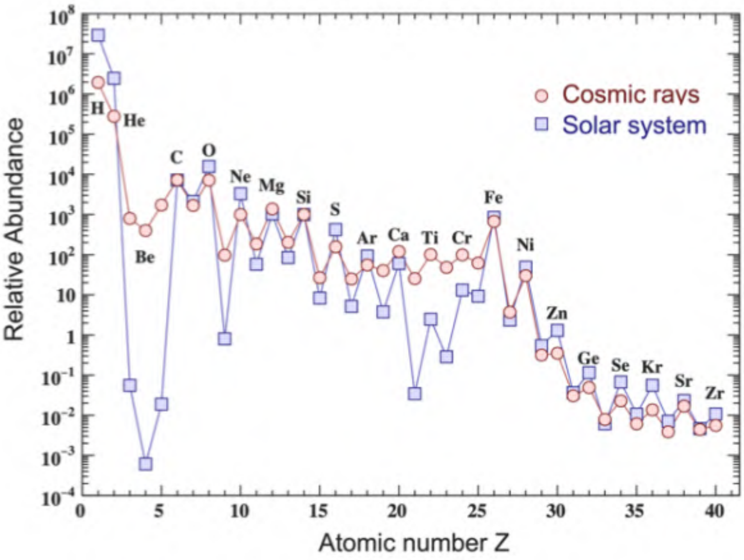

FIGURE 1.5: Relative abundances for $1 \leq Z \leq 40$ in cosmic rays and in the solar system. The plot was made using cosmic-ray data from AMS-02 [135], ACE/CRIS [136], and super-TIGER [137]. *Image source:* [125].

HAWC [26, 124], have measured the energy spectra for different mass groups of cosmic rays for energies below the knee, $E > 6$ TeV, up to 100 EeV.

Direct measurements suggest that protons constitute approximately 88% of the primary nuclei inside the galaxy, while He nuclei account for 9%. The other 3% is made up by heavier elements (like carbon, oxygen, neon, magnesium, etc.) and electrons [125].

The relative abundances of atomic nuclei in the solar system matches the mass composition of primary cosmic rays [125, 126], with a few exceptions for the Li, Be, B, Mn, V, and Sc mass groups. This scenario suggests that primary cosmic rays are produced by stars, while the observed differences for certain nuclei indicate the production of these elements by other secondary processes such as interactions with the interstellar medium (fragmentation or spallation).

Though they are considered mainly as secondary products, antimatter particles are also components of cosmic rays. Thus the precise measurement of the antimatter component and its characteristics (e.g. energy spectrum and relative abundances) offers a different approach to unveil the unanswered questions around cosmic radiation. In addition, these analyses can contribute for the discovery of new physical phenomena, like astrophysical objects made entirely out of antimatter [127–132]. To the date, there haven´t been any cosmic-ray experimental evidence that revealed the presence of antinuclei with masses greater than antihelium and antideuterium [131, 133, 134].

1.6 Sources

Where do cosmic rays come from? There are many assumptions about their origins based on the available data and our current knowledge of these energetic particles, though the full answer to this question still remains a mystery.

Cosmic rays are considered to be of galactic and extragalactic nature. Galactic cosmic rays have energies $E < 10^{18}$ eV, while extragalactic cosmic rays are more abundant in the region above 10^{18} eV [138, 139].

1.6.1 Galactic cosmic rays

The most common scenario on the origin of cosmic rays produced in the Milky Way involves supernova remnants (SNRs), that may be able to produce charged particles up to $\sim 10^{17}$ eV [140, 141]. In addition, thanks to the recent progress made in cosmic-ray and gamma-ray experiments (for example, HAWC [19] and LHAASO [20]), new sources of cosmic rays inside the Milky Way have been discovered [90, 91].

In 2021, the HAWC collaboration presented the observation of very energetic gamma rays ($E > 100$ TeV) originating from the Cygnus region. More recently in 2024, the LHAASO collaboration confirmed the observation of ultra-high-energy gamma rays from the same region. Both measurements support the presence of a PeVatron inside of the *Cygnus cocoon*, which is believed to be a starforming environment [90, 91].

In particular, the HAWC collaboration has made extraordinary contributions to the detection of PeV cosmic-ray production regions, for instance, the confirmation of a PeVatron inside of the galactic center [142], and more recently the measurement of ultra-high-energy gamma rays produced by the microquasar V4641 that provides evidence that this and other similar microquasars can contribute with PeV cosmic rays to the galactic population [143].

1.6.2 Extra-galactic cosmic rays

In order for an astrophysical entity to produce ultra-high-energy cosmic rays, i.e. particles with energies $E \gtrsim 10^{18}$ eV, there are some requirements it needs to fulfill [119, 144]:

- the necessary energy to accelerate particles,
- confine cosmic rays within the region of particle acceleration,
- and account for the observed ultra-high-energy energy spectrum, the chemical abundances of the elemental components, and the arrival directions, among others.

Our galaxy fails to confine cosmic rays above $\sim 10^{18}$ eV, thus the ultra-high-energy cosmic rays must have an extra-galactic origin. The analysis of the anisotropy at large above 4 EeV carried by the Pierre Auger collaboration in 2017 provided strong evidence that supports the extra-galactic origin of the most energetic cosmic rays [138]. Some astrophysical objects that can be responsible for producing very high energy cosmic rays are Active Galactic Nuclei (*AGN's*), Gamma Ray Bursts [145], Starburst Galaxies (SBGs) [144], and Blazars [101].

However, as a result of their charged nature, cosmic rays are scattered by the influence of the magnetic fields throughout the Universe and therefore it is a challenging task to trace back their sources though the measurements of this radiation. In contrast, particles like photons and $\nu(\bar{\nu})$, i.e. electrically neutral particles, have few to none interactions with the medium and therefore their trajectories, on average, remain the same and point directly to their origin. For example, neutrinos are purely products of hadronic interactions and in an astrophysical scenario, this neutral participles are likely to be generated near cosmic ray acceleration sites by the interaction of atomic nuclei with the surrounding medium. In addition, photons can originate from hadronic and electromagnetic processes, such as the decay process of neutral pions ($\pi^0 \rightarrow \gamma + \gamma$) and Compton scattering, respectively. In particular, the IceCube Neutrino Observatory is involved in multimessenger campaigns with several scientific missions, such as the observation of cosmic-ray production and acceleration regions through the observation of the high-energy neutrinos from astrophysical sources [146], among others. In 2018, the detection of TeV neutrinos from the vicinity of the blazar TXS $0506 + 056$ measured with the ICECUBE observatory determined that this blazar is an extragalactic accelerator of PeV cosmic rays [101].

1.7 Acceleration models

The observed energy spectrum, above 10 GeV, is fairly modeled with a power-law model with γ close to -2.7. Any model that tries to explain the particle acceleration mechanism must at least account for this feature.

The Italian physicist Enrico Fermi was a famous and prolific scientist known for his notorious contributions in particle physics [56, 86]. In particular, in the cosmic-ray field, Fermi developed an acceleration mechanism for this type of radiation. The first version of this model, currently known as *second-order Fermi acceleration mechanism*, was published in 1949. In this framework, Fermi proposed that cosmic rays are accelerated as they are repeatedly reflected by the interactions with magnetic interstellar clouds (or magnetic mirrors) [147]. In this model, the magnetic clouds move in a random-walk with a characteristic velocity V thus, at each collision, each particle will obtain a mean energy given by the following relation [148]:

$$\left\langle \frac{\Delta E}{E} \right\rangle = \frac{8}{3}\left(\frac{V}{c}\right)^2 . \tag{1.2}$$

The above expression clearly describes that the process of energy increase is of *second order* with respect to V/c. In addition, in the second order Fermi acceleration mechanism, at each collision with a magnetic mirror, the energy of the primary can increase or decrease. However, the mean energy increases on average because the probability of a head-on collision with the shock is larger in comparison to that of a tail-on collision [148].

It follows that the differential intensity of cosmic rays modeled by the second order mechanism is given by:

$$N(E)dE = \text{constant} \times E^{-(1+(\alpha\tau)^{-1})}. \tag{1.3}$$

In the above expression, $\alpha = \frac{4}{3}\left(\frac{V^2}{cL}\right)$, where L stands for the mean free path between the magnetic mirrors. Finally, the τ parameter represents the time a particle is trapped within the production source.

In this model, the galactic magnetic clouds within travel at a low velocity in comparison to c, $V/c \leq 10^{-4}$, thus there is a small energy gain for the charged particles in each collision. Moreover, to obtain an energy spectrum with a power law distribution, the particles need to be contained at the acceleration region for a characteristic escape time, τ_{esp}, while spectral index can take arbitrary values. In order to model γ as approximately -2.7, as indicated by the data (see section 1.4.1), this model requires specific constrains and physical assumptions.

Now, an alternative scenario is the *first-order Fermi acceleration mechanism*, which considers a charged particle that is accelerated by the collision with a front of a shock wave (for example, produced by SNRs, AGNs, etc.) that moves through the interstellar medium at supersonic velocities [119]. This configuration will produce a constant rate of energy increase on the (V/c) term. This improvement enhances the particle's acceleration. Now, the magnetic fields on each opposite side of the shock (in front of or behind it) are turbulent. After the first collision, these turbulent magnetic fields scatter the particle in a random walk throughout the field lines inside the shock region, reason why the first-order Fermi acceleration mechanism is commonly referred to as *diffusive shock acceleration* [149]. In the case particular case of no turbulent magnetic fields, the confinement time at the site would be very short. When a particle is scattered by the magnetic fields, there is a probability that it can pass through the shock from the upstream to downstream direction or downstream to upstream [119]. Both types of crossings will increase the particle's energy [119, 148]:

$$\left\langle \frac{\Delta E}{E} \right\rangle = \frac{4}{3}\left(\frac{V}{c}\right). \tag{1.4}$$

The particle is scattered again by the magnetic fields upstream or downstream, repeating the process many times, and with each crossing, it gains energy. With every cycle, the particle has a chance to escape the shock and become part of the population of cosmic rays. The particle escape probability from the shock is given by [148]:

$$P_{\text{esc}} = 1 - \frac{4}{3}\left(\frac{V}{c}\right). \tag{1.5}$$

Finally, the predicted particle energy spectrum is:

$$N(E)dE = \text{constant} \times E^{-2}dE. \tag{1.6}$$

In the above expression, the predicted spectral index differs from the experimental data. Some models like the ones in [119, 149] propose that the spectral index can be modified by means of the diffusive propagation of the particles across the Milky Way. In comparison to the second order mechanism, this model is more efficient at accelerating cosmic rays to the highest energies and can be present in different astrophysical sources.

1.7.1 Particle confinement and acceleration at the source

Probably the most popular plot that helps identify potential cosmic ray accelerators is the one proposed by Anthony Michael Hillas in 1984, the so-called *Hillas Diagram*. In this plot, Hillas establish a relation between the physical magnitude, $\mathrm{R}_{\text{source}}$, and magnetic field, B, intrinsic to the acceleration site for a given primary energy, without taken into account efficiency losses. Such relation is given by [150]:

$$E_{\text{max}} \simeq Z\left(\frac{B}{\mu G}\right)\left(\frac{R_{\text{source}}}{kpc}\right) \times 10^{18} eV. \tag{1.7}$$

In the previous expression, the maximum achievable is represented by E_{max}, while Z is the charge of the primary. From this relation, it is clear to identify that the spectra of light nuclei will have a cutoff at lower energies than in the case of the spectra for the heavy nuclei because the particles with lower electric charges escape earlier from the magnetic confinement at the source [151].

In the Hillas plot, $\mathrm{R}_{\text{source}}$ and B are also plotted for different astrophysical sources, which, together with relation (1.7), allows to identify different possible cosmic ray

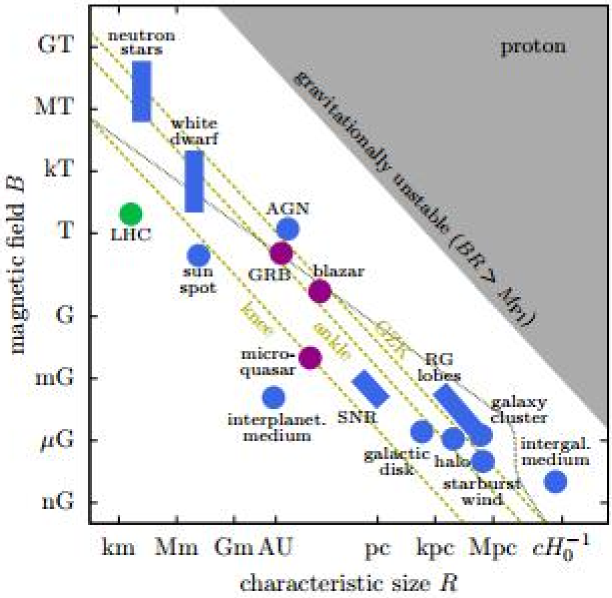

FIGURE 1.6: The Hillas plot identifies potential cosmic ray sources (blue objects) based on their characteristic magnetic field, B and their size, R [152]. From top to bottom, the dotted green lines represent the predicted maximum energies for proton acceleration sites. These correspond to the to the GZK limit (5×10^{19} eV), the ankle ($\approx 10^{18}$ eV), and the knee region, ($\approx 10^{15}$ eV), respectively. *Image source:* [153].

accelerators. Astrophysical objects like gamma-ray bursts, neutron stars, white dwarfs, sunspots, AGN, SNRs, galaxy clusters, and galactic disks and halo are some of the astrophysical objects that qualify as cosmic-ray accelerators. These and other objects are plotted in Fig. 1.6 where each source is indicated with its characteristic magnetic field at the site, B, as a function of its typical size. I addition, the model constraints, see Eq. (1.7), for cosmic-ray acceleration at the source are also shown.

All the cosmic ray source model must recover the measured energy spectrum with their predictions and explain all of its features. For example, the features in the energy spectrum of cosmic rays are a reflection of the cut-offs predicted by Eq. (1.7), and one possible interpretation is a magnetic rigidity cutoff in the source. Another classic example, is the three-population Hillas (H3a) model as described in [154]. In here, the total energy spectrum is described by the presence of three different categories of sources, each of them with different E_{max} efficiency:

Population 1: This population could be composed of supernova remnants spread all over the Milky Way. The position of knee represents the maximum efficiency of cosmic acceleration at the sources responsible for this group.

Population 2: The nature of this accelerator is unknown, however, it is assumed to be of galactic nature and would contribute to the intensity of cosmic rays inside the energy interval from 10 PeV to 1 EeV. The cutoff for protons would be located at $E = 2 \times 10^{15}$ eV.

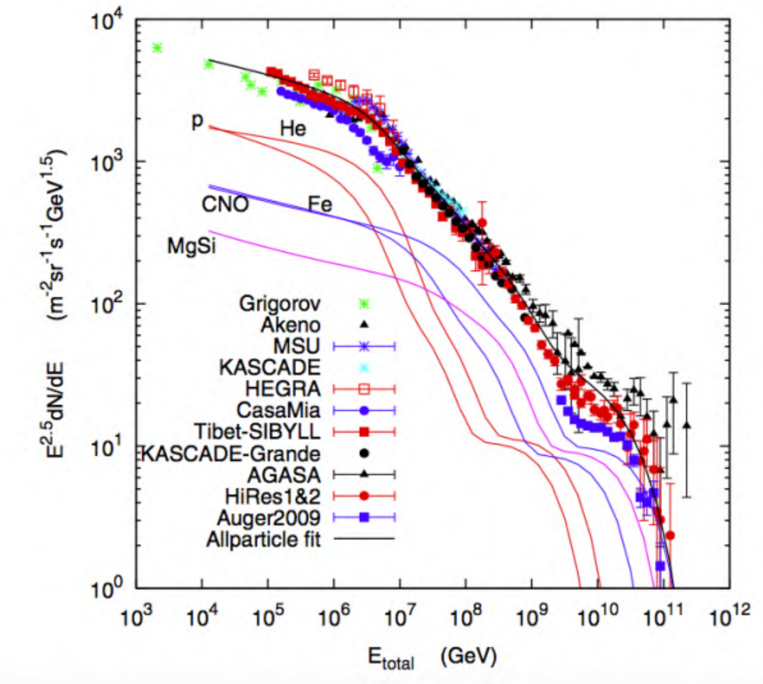

FIGURE 1.7: The spectral features observed in the measured in the all particle cosmic ray energy spectrum can be explain though the H3a model [154].

Population 3: This population would be of extragalactic nature and might generate cosmic rays at ultra-high energies. The cutoff for protons would be found at energies between 3 EeV and 60 EeV.

Under this model, it was expected that the spectrum of cosmic rays within the TeV - PeV energy range should behave as a power-law, however the latest results from HAWC [22, 124], NUCLEON [23], DAMPE [18, 29] and CALET [155, 156] revealed new features in the energy spectra of the different components of cosmic rays and the all-particle spectrum, situation that suggest possible new physical interpretations like, for example, the existence of a local nearby source of TeV cosmic rays [3, 45, 157, 158].

1.8 Propagation

Along their propagation inside the interstellar medium, cosmic rays undergo energy losses and additional acceleration phenomena that modify the initial spectral index spectrum intrinsic to the source.

Once the cosmic rays escape the source or acceleration region, these particles start their propagation through the cosmos. Given the fact that cosmic rays have an electric charge, they are diffusely deflected in a random walk caused by magnetic fields, making the particles deviate from their original trajectory. Only cosmic rays with E $\sim 10^{20}$ eV are not affected by these processes and retain their original trajectories. Through their propagation, primary cosmic rays can produce secondaries by means of different physical processes such as spallation, hadronic decay, gamma

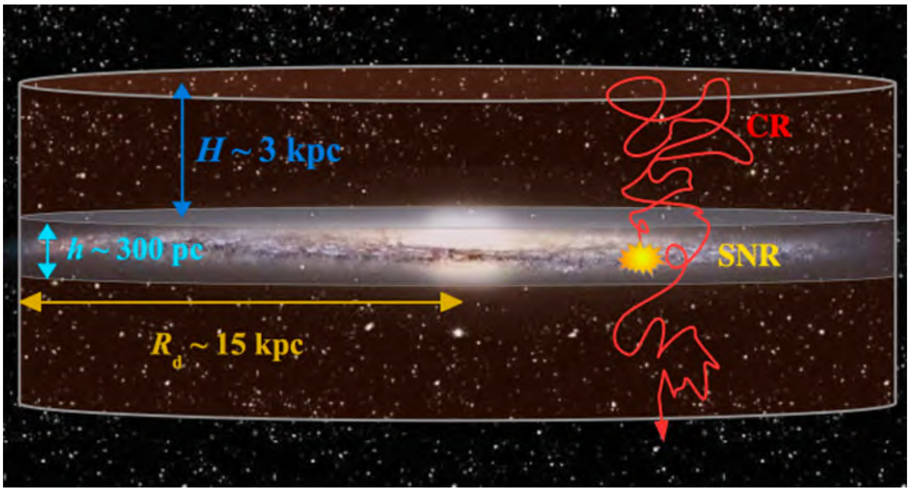

FIGURE 1.8: In this representative picture of the leaky box model, the galaxy is represented by a cylindrical shape with a diameter of D_d = 30 kpc and 3 kpc in height. Inside the box (galactic disk), cosmic rays travel in all directions driven by the turbulent magnetic field of our galaxy and by the interactions with the ISM. As shown here, a small fraction of cosmic rays have a small probability to escape the confinement [149].

rays, neutrinos, Compton scattering, pair production ($p + \gamma \rightarrow p + e^+ + e^-$), and pion production ($p + \gamma \rightarrow \pi + N$) [150].

A simple propagation model for cosmic rays confined in the Milky Way is the Leaky box model (see Fig. 1.8), where the Milky Way is modeled like a cylinder with a height $\sim 3\,kpc$, and $15\,kpc$ in radius [149]. The galactic sources of the cosmic radiation are equally distributed inside the galactic disk of $300\,pc$ of thickness. Due to the galaxy's total magnetic field, the charged particles are confined inside the box, where they are accelerated and diffusely propagated. However, when a cosmic ray interacts with the galaxy's frontier it has a small probability of escaping, otherwise it is bounced back inside the box. A numerical interpretation of this model is the GALPROP code [159], which allows the user to simulate the diffusion of primary and secondary cosmic rays and their interactions accross the galaxy.

Chapter 2

Extensive air showers

The previous chapter covered the historical breakthroughs of cosmic-ray science, and how some of the scientists from the late XIX and early XX centuries came up with pioneer techniques to overcome the observational and theoretical challenges of the field. In particular, Bruno Rossi [83, 160], Werner Kolhörster [88], and Pierre Auger [89] contributed to the field of study of Extensive Air Showers, a phenomena caused by the interaction of primary cosmic rays and the air molecules. The study of EAS, how are they described and their impact to cosmic rays research are detailed in this chapter.

Cosmic rays measurements are performed directly outside of Earth's atmosphere or indirectly at ground level. Direct measurements are carried out with particle detectors attached to air-balloons, airplanes, spacecrafts, and artificial satellites, and their primordial task is the observation of primary cosmic rays near the upper layers of the atmosphere. On the other hand, when a primary cosmic ray makes its way through the interstellar medium and impinge over our atmosphere it will interact, at some atmospheric depth that depends of its kinetic energy, with the nitrogen and oxygen molecules of the atmosphere. The result of this interaction is what we commonly know as *Extensive air showers* (EAS) of secondary particles, and the experimental observations of this phenomenon are called indirect measurements. One effective way to measure an EAS is by setting up a ground-base particle array detector.

The first evidences of EAS observations were made by Bruno Rossi [83, 160], Werner Kolhörster [88], and Pierre Auger [89]. Historically, Auger has been recognized by many authors as the pioneer of the air shower phenomenon. By the year of 1938, Auger carried out the experiment that led him to this discovery at the Jungfraujoch[1], Switzerland. The experimental setup consisted on cloud chambers and G-M counters spaced by distances of the order of 10 meters (up to 300 m) [89]. The detectors were run simultaneously and were employed to analyze the charged component of cosmic rays at ground level. The data showed the simultaneous arrival of charged particles at the particle counters within a time window of approximately $\sim 1\mu$s. From these observations, Auger concluded that high-energy primary cosmic rays triggered atmospheric showers located at the top layers of the atmosphere. At that time, Auger and his team were not aware of the previous work made by Bruno Rossi and Werner Kolhörster on the same matter.

All together, the contributions from Rossi, Kolhörster and Auger have began a new method of observations in astroparticle physics. The method, however, rely on the detailed description of the hadronic interactions involved in this phenomenon, which is a challenging task.

---

[1] At an altitude of 3450 m a.s.l.

It is important to point out that extensive air showers are not exclusive to cosmic rays, there are showers induced by gamma rays as well, and are purely electromagnetic.

Meanwhile, the showers generated by cosmic ray nuclei are constituted by three components: hadronic, electromagnetic, and muonic. Each of them will be described in the following sections.

2.1 Hadronic component

This component is composed by mesons, baryons, antibaryons and atomic nuclei. Among the mesons we found pions, kaons and charmed particles, and as a part of the baryons, neutrons and protons. Such particles are produced in hadronic interactions between the shower particles and the atmospheric molecules or by hadronic decay. Hadronic collisions with momentum transfer $Q^2 \approx 0$ produce particles with small transverse momentum, which moves along the direction of the primary particle. These interactions happen in the non-perturbative region in quantum chromodynamics (QCD). They must be described with phenomenological models, whose parameters are tuned with accelerator data. On the other hand, hadronic interactions with large Q^2 generates particles with large transverse momentum, which moves away from the main shower axis. Such processes can be determined through perturbative QCD (pQCD). Neutral and charged pions are generated in abundance in the hadronic collisions of the shower particles [161]. The decay of these mesons feed the electromagnetic and muon components in the EAS, respectively [96].

2.2 Electromagnetic component

As mentioned before, this component is mainly a product of the electromagnetic decays of kaons and pions in the EAS. The neutral pion decay through the channel $\pi^0 \rightarrow \gamma + \gamma$, which directly contributes to the electromagnetic component [21, 96]. The most prominent physical process involved in the evolution of this component in the atmosphere are the photon pair production and the *bremsstrahlung* of electrons. In addition, other physical processes that affect the development of the electromagnetic component of the air shower are the radio emission, energy loss by interactions with the medium (ionization), production of Cherenkov photons, and the photoelectric effect [95, 148].

2.3 Muonic component

The charged pions and kaons of the EAS commonly decay into muons and neutrinos, feeding the shower muonic component. The decay channels are shown below [21, 96]:

$$\pi^+(\pi^-) \rightarrow \mu^+(\mu^-) + \nu_\mu(\bar{\nu}_\mu), \tag{2.1}$$

$$K^+(K^-) \rightarrow \mu^+(\mu^-) + \nu_\mu(\bar{\nu}_\mu), \tag{2.2}$$

Muons can pass through significant amounts of matter before interacting, which represents a challenge for its detection. For this reason, a common muon detector is equipped with a thick shielding or is buried underground. A thick shielding or underground placement effectively blocks the less penetrating particles, considered as background noise, and isolates the muon signals for more accurate measurements. On average, muons are produced at an elevation of approximately 15 km into our atmosphere. If there is no decay, a muon can experience a decrease in its energy of approximately 2 GeV before it reaches ground level [162]. The decay of the muon can contribute to the electromagnetic component, however its contribution is small [163]. Finally, the muonic component is closely related to the primary mass. For the same primary energies and a fixed observation level, a heavy-primary induced air shower will contain on average a larger number of muons than a light-primary induced air shower [164–166]. Thus, the precise measurement and description of this component is relevant for mass composition studies of cosmic rays.

Neutrinos evade most of the particle detectors as they only interact by means of the weak force, however it's important to recall that an accurate representation of the development of the shower and its energy estimation must consider the contribution from the neutrinos. [164–166]

2.4 Air shower properties

The precise measurement and reconstruction of the EAS is crucial to determine the composition of the primary particle, mass composition and arrival direction. The reconstruction of the main properties of the cosmic ray depends on the characteristics of the detector.

Some of the most relevant air shower features to measure in relation with the primary cosmic ray are described below:

Shower axis: This parameter corresponds to the path that a primary particle would have taken to the point at the observation level where it would have arrived, assuming no interactions with the atmosphere molecules. It provides the arrival direction of the primary particle (c.f. Fig. 2.1, left panel).

Lateral density distribution: Purely electromagnetic showers have, on average, representative characteristics that allows us to recognize them from cosmic-ray induced events [167]. This differences can be observed though the lateral spread of secondary particles. This parameter describes how the density of particles produced by the shower varies with their distance to the shower axis at the EAS plane [168]. In particular, cosmic-ray induced event on average will present an irregular and uneven lateral distribution of secondary particles; meanwhile, a pure electromagnetic EAS is characterized by a smooth and even lateral profile.

Shower maximum: This parameter marks the point of maximum development of the shower. Here, the production of secondary particles has reached its maximum and the particle multiplicity is the highest [95, 169].

Depth of maximum development, $X_{\mathbf{max}}$: It represents the relation between the maximum particle multiplicity and the atmospheric depth. This parameter is sensitive to the energy of the primary particle, and can also vary with its mass composition [169, 170].

Shower core: Considered as the point in which the shower axis meets the with the observation plane. This region has the highest particle density [95]. A common procedure to estimate the coordinates of the core consists on a fit to the measured lateral distribution of the secondary particles with a proper function

[95, 169]. The particle distribution at the shower core, its shape and broadness is directly related to the nature of the primary particle that triggered the event. For example, an hadronic shower induced by an iron nuclei will result in a flat and broad shower core in contrast to a proton-induced event.

The central region of a pure electromagnetic EAS is compact and well defined. On the other hand, hadron induced air showers can exhibit *multi-cores* due to fluctuations, scattering of nuclei fragments surviving from the spallation of the primary particle, high concentration of muons, and secondary particles with high momentum [169].

Shower front: This conceptual surface marks the leading edge of the EAS event as it propagates and expands outwards into the Earth atmosphere [95]. The secondary particles that are close to the shower axis are characterized by small values of transverse momentum, travel longitudinally and arrive almost simultaneously, creating a uniform shower front. However, the secondary particles far from the central region will travel longer distances. This effect gives the shower front a slight curvature.

Arrival direction: It is typically determined by fitting the distribution of the recorded arrival times from each of the observed secondary particles at the shower front. Most procedures parametrize the shape of the shower front to a plane or a cone due to its curved nature [169, 171]. Once the shower front shape is determined, the shower axis is calculated. The axis is usually defined by the unitary vector perpendicular to the shower plane (cone) [95, 169, 171]. The reconstructed direction of the primary particle is estimated from the azimuthal and zenithal angles of the shower axis. The later are represented by ϕ and θ, respectively.

Longitudinal age, s: The longitudinal age of an EAS describes its development stage across the atmosphere by tracking the variations in the number of secondary particles (photons and $e^{\pm}$) (see Fig. refFig:showerSketch, right panel) [95, 172]. The initial interaction inside the atmosphere is represented by $s = 0$. At the shower maximum, the longitudinal age takes a value of $s = 1$. After the maximum development, this parameter has values $s > 1$ [172].

Lateral age parameter: Like the longitudinal age, this parameter was developed for pure electromagnetic shower to characterize the development stage, however this concept can be extended to hadronic EAS for the same purpose [172]. The lateral age parameter is a measure of the lateral shape of the secondary particles distributions at the detector observation level as a function of the radial distance to the EAS axis. Mathematically, this parameter is an expression of the slope of the lateral distribution of secondary particles [167, 172, 173]. For example, a small (large) value of the lateral age parameter describes an EAS event that started deeper (shallower) into the Earth atmosphere and the lateral distribution of its secondary particles at the observation level has a steeper (flatter) profile. On average, this EAS events are induced by light (heavy) primaries with high (low) energies, and are called as *young* (*old*).

2.5 Air shower development

So far, the importance of a detailed description of the extensive air shower's development and its components through their passage across the atmosphere have been

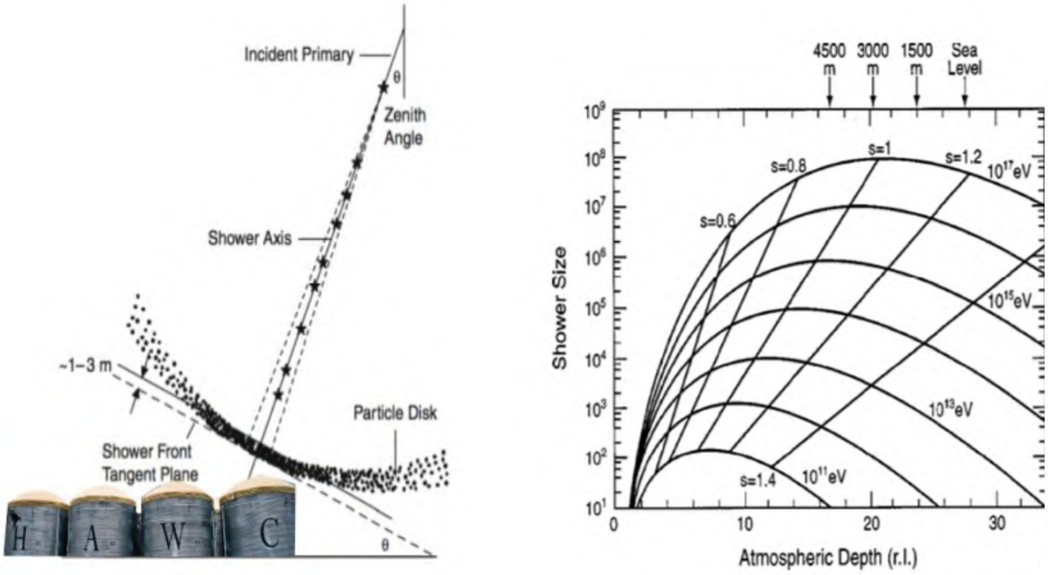

FIGURE 2.1: *Left panel:* Simple diagram of an EAS. The primary particle, zenith angle, shower axis, particle disk and shower front are shown. A small number of particle detectors are exhibited at the bottom as a reference. *Image modified from:* [95]. *Right panel*: In here, the curves represent the longitudinal development for purely electromagnetic EAS with different primary energies. *Image source:* [174].

addressed. Nowadays, there is a plethora of models and software packages dedicated to this particular matter.

2.5.1 The Heitler model

It is a basic approach to understand the evolution of electromagnetic showers and their main features [175]. Despite the fact that the predictions from this model are not the most accurate when treating real data, the Heitler model illustrates the air shower development and the physics involved [176].

The model considers

- $\gamma + \gamma \rightarrow e + e^{+}$ (pair production),
- $e^{\pm} + \gamma \rightarrow e^{\pm} + \gamma$ (braking radiation).

as the main processes for the development of the electromagnetic shower. The process starts with a photon, γ, of energy E_0. This photon initiates a cascade by splitting into a e e^{+} pair each with energy $E/2$, after traveling a fixed interaction length, λ_e, through the atmosphere (see Fig. 2.2, left panel). Then, a photon will be emitted by an individual positron or electron. This step increases the number of particles in the shower by a factor of two. Each new generation will continue to repeat the process, with each particle producing two new particles of half its energy. In particular, if this process is repeated n times, the shower will contain a total of 2^n secondary particles. Moreover, it is possible to know the total number of generated particles for a given atmospheric depth, X, with the following relation

$$N(X) = 2^n = 2^{X/\lambda_e}. \tag{2.3}$$

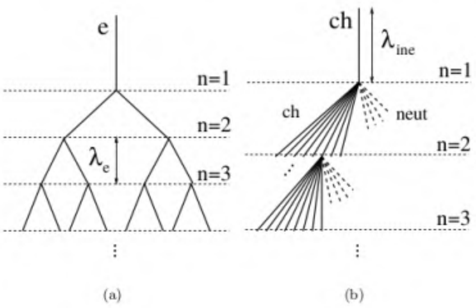

FIGURE 2.2: *Left panel:* Model for the evolution of a purely electromagnetic air shower. Electrons and photons are represented equally by solid lines, while λ_e is the electromagnetic interaction length. *Right panel:* Same, but for an hadronic induced EAS. In here, the solid lines represent charged particles, neutral particles are represented by the doted lines, and the primary particle interaction is represented by λ_{ine}. *Image sources:* [176, 177].

where $X = n \cdot \lambda_e$. In this approach, the energy E per secondary particle at an atmospheric depth X is dependent of the primary energy, E_0, and it is estimated through the mathematical expression:

$$E(X) = \frac{E_0}{2^{X/\lambda_e}}. \tag{2.4}$$

The maximum development of a pure electromagnetic event is reached at the *critical energy*, E_c. In this development stage, the main production processes are constrained by the energy loss. This point is located at an altitude

$$X_{max}(E_0) \sim \lambda_e \cdot \ln\left(\frac{E_0}{E_c}\right). \tag{2.5}$$

In addition, the maximum number of secondary particles produced at the maximum development of the EAS is given by the relation

$$N_{max} = \frac{E_0}{E_c}. \tag{2.6}$$

The copious production of secondary particles (electrons, positrons and gammas) will abruptly end after the critical energy is reached [169, 176, 177].

With this model, it is possible to get a relation between the depth X and the number of shower particles and estimate the depth of maximum development of the EAS. However, it is employed for EAS created by photons. For hadron-induced EAS, the Heitler model can be modified [176, 177], as will be described next.

2.5.2 Modeling of hadronic induced air showers: the Heitler-Matthews model

In the context of this framework, an hadron with primary energy E generates a total of N_{tot} new particles with energy E/N_{tot} in one interaction after traveling a distance equivalent to an interaction length λ_{ine}. The dominant component of secondary particles will be charged pions, N_π, accounting for $2/3$ of the total, while the other third will be neutral pions, N_0 (see Fig. 2.2). Thus $N_{tot} = N_\pi + N_0$. Neutral pions will decay mainly into two photons, and charged ones, into muons and neutrinos. From here, it is quickly deduced that the hadronic component will transfer one third of its energy to the electromagnetic sub shower after every interaction. If this process continues n times, the energy per secondary hadron-induced or electromagnetic shower particle is expressed as [176]:

$$E_h = \left(\frac{2}{3}\right)^n E_0, \tag{2.7}$$

$$E_{EM} = \left[1 - \left(\frac{2}{3}\right)^n\right] E_0, \tag{2.8}$$

where $E_0 = E/N_{tot}$.
After several generations, in an hadronic EAS, the electromagnetic component will carry a large fraction of the energy of the primary particle. For instance, after 6 interactions within the atmosphere, this component will bear $\sim$ 90% of the primary energy on average [176]. For this reason, the maximum shower depth of an hadron induced event will correspond to the depth of the electromagnetic component, X^e_{max}. So, an approximate expression for the maximum shower depth of the hadronic EAS is given by [176]:

$$X_{max}(E_0) \sim \lambda_{ine} + \lambda_e \cdot ln\left(\frac{E_0}{N_{tot}E_c}\right), \tag{2.9}$$

where N_{tot} is the total number of secondary particles produced in the first hadronic interaction, and E_0 is the energy fraction for each of the secondaries.

Below the critical energy E^π_c, after n_c consecutive interactions, the charged pions no longer undergo hadronic interactions, and decay into muons. In particular, the total number of charged pions is $N^{n_c}_\pi$, with energy $E/N^{n_c}_{tot}$. Thus, the total number of muons resulting from a number $N^{n_c}_\pi$ of charged pions in an interaction can be approached by:

$$N_\mu = N^{n_c}_\pi = \left(\frac{E_0}{E^\pi_c}\right)^\alpha, \tag{2.10}$$

where α = ln(N_{ch})/ln(N_{tot}). According to [176, 177], $0.82 \leq \alpha \leq 0.95$.

The present model applies only to EAS generated by nucleons. In order to extend the formalism to the case of a primary nuclei with atomic mass A and energy E_0, the supperposition model is used. The main idea is to consider the incident nucleus as an ensemble of A individual nuclei, each carrying a fraction of the primary energy, given by E_h = E_0/A. Therefore, under this hypothesis, the shower's parameters will be:

$$X^A_{max} \approx X_{max}(E_0/A), \tag{2.11}$$

$$N^A_\mu \approx A \cdot \left(\frac{E_0/A}{E_{dec}}\right)^\alpha = A^{1-\alpha} \cdot N_\mu. \tag{2.12}$$

The present model allows to describe the basic properties of the EAS induced by cosmic rays. It also provides basic basic relations between the parameters that describe the longitudinal development of the EAS with the atomic mass and the energy of the primary nucleus.

However, when it comes to the description of real extensive air shower events, the Heitler-Matthews model does fails to offer a precise description of the measurements. In addition, it only depicts the longitudinal growth of hadronic showers in 1D, ignoring the lateral development of the shower. The first studies of the lateral spread were made for showers of electromagnetic nature by Nishimura, Kamata and Grisen in the mid 50's [167, 173]. Such treatment can be extended to hadron induced showers. The lateral spread or lateral distribution is a key parameter that must be considered for the correct understanding of the extensive air showers.

However, for a more realistic description of the complex three-dimensional development of hadron induced EAS, hadronic interaction models have been developed with the purpose to describe particle interactions, predict the shower properties such as the lateral distribution, longitudinal profile, and the primary energy, and ultimately to interpret high-energy physics results at energies inaccessible for particle accelerators.

Therefore, the high-energy hadronic interaction models are essential tools in the simulation of the interaction of cosmic rays and air molecules. A number of simulation packages have been developed, incorporating these models alongside Monte Carlo techniques for this purpose.

2.6 Simulation packages for high-energy hadronic interactions

With technological developments, nowadays there are numerical event generator packages that make more realistic simulations for the probabilistic nature of particle interactions and predict their outcomes through random sampling techniques (Monte Carlo approach), and the implementation of theoretical and empirical models of particle physics.

In 2009, the results from high-energy physics experimental runs at the Large Hadron Collider (LHC) were publicly released [178–180]. Some of the most relevant results include the measurements of the proton-proton collisions up to a center-of-mass energy of $\sqrt{s} = 7$ TeV. These results were important to improve the descriptions of particle production in hadronic collisions at high energies within the new generation of MC cosmic-ray event generator packages. The post-LHC era has seen the development and refinement of high-ernergy hadronic interaction models like EPOS-LHC, QGSJET-II-04, and SIBYLL 2.3, which incorporate constraints from LHC data [181, 182].

The production of secondary particles and development of hadron induced extensive air showers are ruled by hard and soft scattering processes. The hard processes are characterized by a large momentum transfer (Q^2), and are well described with perturbative treatments of QCD. On the contrary, the accurate description of the soft part of hadronic interactions, for which the momentum transfer is small $Q^2 \ll 1\ \text{GeV}^2$ [183, 184], is a major challenge that require special theoretical treatments different from the pQCD, and generally involve empirical parametrizations. Take for example the Gribov-Regge theory [185], developed for the description of the exchange of microscopic parton showers with small transverse momenta in hadronic interactions (soft processes). Within this framework, these processes are mediated by the exchange of hypothetical effective objects known as *Reggeons*. In particular, the *Pomeron* is introduced to explain the diffraction and elastic scattering at high energies. This object is a special type of Reggeon, characterized by no color, electric charge, or flavor, and can be considered as an hypothetical particle formed by gluon chain. Event generator models like EPOS-LHC [186] and QGSJET-II [187] employ the Gribov-Regge theory for their respective calculations. An alternative to the Gribov-Regge theory is the QCD eikonal mini jet approach, which treats hadronic collisions as sequence of mini-jet interactions with low transverse momentum between the incident particle (seen as a small probe) and the target hadron. This theoretical framework is the base for event generator packages like SIBYLL [188].

Some of the most popular high-energy hadronic interaction models which have been employed for the simulation of cosmic-ray interactions and related phenomena are DPMJET II.55 and III [189], EPOS-LHC [186], QGSJET-II-04 [48], and SIBYLL 2.3 [188]. All of these models accurately reproduce particle accelerator data up to LHC energies, E_{cm} = 10 TeV [190–192]. However, their high-energy extrapolations, relevant for indirect studies of cosmic rays, diverge significantly and represent an important cause of systematic uncertainties. These inconsistencies lead to differences in predicting the EAS observables and its development through the atmosphere, and may induce a bias in cosmic-ray studies.

The most representative high-energy hadronic interaction models, commonly employed for cosmic-ray analyses, such as EPOS-LHC, QGSJET-II, and SIBYLL are described and compared to each other.

2.6.1 EPOS-LHC

Overall, it is a reliable tool that provides results of the soft particle production in hadronic interactions, and cosmic ray phenomena [193]. The goal of EPOS is to describe soft particle production for any system and energy with minimum bias, including rare particles (like charmed particles) and the distributions of all possible final-state particles. It takes into account various nuclear effects such as parton saturation, screening, and high density effects in heavy ion collisions [191, 193]. Like other hadronic interaction models models, EPOS-LHC is based in the Gribov-Regge theory however, in this framework, the energy conservation is considered in the particle production and for the estimation of the cross-section while other models don’t consider this for the cross-section analysis [191, 194].

nucleus and nucleus, hadron and hadron, and hadron-nucleus

2.6.2 QGSJET-II

The latest version of this Monte Carlo event generator package is *QGSJET-II-04* [48], which is based on the Quasi-Gaussian String Jet (QGSJET) model, a non-perturbative QCD approach that incorporates elements from the Gribov-Regge theory. A key feature of QGSJET-II is its explicit treatment of the multi-Pomeron exchanges and related screening effects, which are fundamental in nuclear collisions to regulate the growth of cross-sections and particle production. It can simulate cosmic-ray air showers at different depths in the atmosphere with energies from 10^{10} eV to 10^{20} eV, interactions between nucleus with nucleus, hadron with hadron, and hadron with nucleus, and the production of secondary particles based on fragmentation functions and conservation laws. While its reliance on phenomenological parameters for aspects of non-perturbative QCD introduces uncertainties, QGSJET-II is recognized for its detailed treatment of baryon-number transfer and forward particle production, which are crucial for the development of air showers along the shower axis [190, 191].

2.6.3 SIBYLL

SIBYLL, or Simulating Interactions of High-Energy Beams with Matter, is a high-energy hadronic interaction model widely employed for the simulation of extensive air showers and particle accelerators physics [195]. The predictions from this model are in good agreement with LHC data for particle production. It models collisions involving protons, neutrons, pions, and other hadrons at energies ranging from GeV to PeV. This event generator employs the minijet model for hard interactions, and adopts some aspects of the Gribov-Regge theory to describe pomeron exchanges for the case of multiple soft interactions, and uses the Lund model for the string hadronization. Nonetheless, it also implements different theoretical approaches that include parton-based models, quark string models, and phenomenological parameters from empirical data.

2.6.4 Differences between post-LHC hadronic interaction models of high energies

It is stated that the modeling of hadronic collisions are crucial for understanding the physics behind the evolution of cosmic-ray EAS events. Even at the LHC energy scales, where there is experimental data available, the predictions among the different hadronic interaction models have some differences, for example, regarding the average number of produced secondary hadrons [182, 195]. These deviations increase with the energy and are a consequence of the different theoretical treatments, empirical parametrizations and extrapolations beyond LHC energies. Confronting the predictions made by the different models with each other, and comparing the model predictions with experimental measurements, are crucial to test the efficiency of the hadronic interaction models at the highest cosmic ray energies.

The EAS parameters are constrained by the high-energy hadronic interaction model predictions and the results may differ from model to model. Thus, several comparative analysis of the main high-energy hadronic interactions models have been carried out in order to comprehend their impact on EAS observables. Some of the most relevant parameters for the shower's development are the particle multiplicity, depth of the shower maximum, X_{max}, elasticity (largest energy fraction carried by the leading particle of the shower after the initial interaction), and the number of muons reaching the ground, N_{μ}. For energies closer to 1 PeV, EPOS-LHC has a larger multiplicity of secondary particles in comparison to QGSJET-II-04 and SIBYLL 2.3c, being the last one with the lowest multiplicity, however, in this energy regime the differences are small [181, 191]. On the other hand, SIBYLL 2.3c has the largest elasticity among the models described [196]. For instance, the multiplicity and elasticity effects have a direct influence in the shower development, thus modifying the position of the shower's maximum depth. According to [181], the predictions for the depth of shower maximum made by QGSJET-II-04 and SIBYLL 2.3c differ by approximately ± 20 g/cm^2 from the calculated value of EPOS-LHC. The same study reports that the differences in the predicted number of muons observed at ground level (1500 m a.s.l.) by these three models are no greater than 10% for inclined EAS, $\theta = 40^{\circ}$. However, for vertical events, EPOS-LHC generally predicts the highest number of muons, followed by QGSJET-II-04, and SIBYLL 2.3 with the lowest. In addition, EPOS-LHC and QGSJET-II-04 differ in their predictions for shower events below the knee, with EPOS-LHC indicating more electromagnetic energy measured at the particle detectors.

Overall, these and other differences indicate the need for further theoretical development of hadronic interaction models and more precise experimental measurements of air shower observables at high energies to better constrain these models and, therefore, improve the understanding of cosmic ray properties and the physics involved in the hadronic interactions. Finally, table 2.1 includes a comparison of the EAS characteristics predicted by the simulation packages for high-energy hadronic interactions from above, highlighting their main differences.

TABLE 2.1: Main characteristics of the QGSJET-II-04 [48], EPOS-LHC [186, 193], and SIBYLL 2.3c [195] simulation packages of high-energy hadronic interaction models.

Características	QGSJET-II-04	EPOS-LHC	SIBYLL 2.3c
Theoretical framework	Pomeron exchange + Regge-Grigorov + Parton model	Pomerons + Regge-Grigorov + Energy conservation + Parton model	Mini jets + String hadronization (Lund model) + Regge-Grigorov
Average multiplicity in p-p collisions $@\sqrt{s} \leq 10^3$ GeV [192]	Similar to EPOS and SIBYLL	Similar to QGSJET-II and SIBYLL	Similar to QGSJET-II and EPOS
Muon number at 1500 m a.s.l. for proton induced EAS with $\theta = 40^\circ$ $@E = 10^{15}$ eV [192]	Slightly smaller in comparison to EPOS and SIBYLL	Similar to SIBYLL	Similar to EPOS
Elasticity for p-p interactions $@\sqrt{s} = 10^4$ GeV [192]	Highest elasticity	Higher elasticity in comparison to EPOS	Lowest elasticity
$\langle X_{\max} \rangle$ $@E = 10^{17}$ eV [192]	Shallow $X_{\max}$ predictions	Deeper predictions in comparison to QGSJET-II	Deepest $X_{\max}$ predictions

Chapter 3

Cosmic-ray detection techniques

Long before the discovery of cosmic radiation and its components, there were countless efforts for the improvement and creation of instruments for the measurement of the ionizing radiation phenomena observed in closed and isolated detectors observed by end of the XIX century [56, 169]. Once Victor Hess discovered the cosmic rays, the following experimental efforts were extended to develop and apply particle-physics detectors to study the properties of this type of radiation. From the simplest electroscopes to ground-base particle detector arrays, to cloud chambers and nuclear emulsions, the way humans have measured cosmic rays has rapidly evolved through time [56, 63, 96, 197, 198]. The accurate measurement of the properties of these high-energy particles is crucial for a complete description of their production and propagation in space. Cosmic-ray observations can be performed with direct or indirect detection methods, both with unique characteristics. This chapter describes the cosmic-ray detection techniques, and some of the most relevant cosmic-ray experiments that have measured the spectrum within the energy interval $10\,\text{TeV} \leq E \leq 1\,\text{PeV}$ energy interval, which is of interest for the present study.

3.1 Direct measurements

Cosmic ray observations can be made at ground level, on the surface or underground, at high altitudes in the atmosphere, or on top of or outside the atmosphere for the observation of cosmic rays before their atmospheric interactions. The later are known as *direct measurements*, and are performed with instruments that are carried on airplanes or on board of air balloons, or installed at satellites or space ships [95, 169]. Typically, direct measurement experiments are distinguished for possessing an excellent energy and angular resolution, large duty cycles. In general, space- and air-borne missions are able to detect cosmic rays before colliding with the atmosphere, thus making this type of instruments ideal for the measurement of the chemical composition of galactic cosmic rays, in addition to reconstruct the total and individual spectra. Moreover, most of the time they don't require the implementation of hadronic interaction models for data reconstruction.

The direct detection method offers the opportunity to measure cosmic rays before their interaction with or before their attenuation by the atmosphere. Once a primary impacts our atmosphere it will interact with it multiple times, losing energy in the process or fragmenting into less energetic secondary particles. Low energy cosmic rays are most likely to be absorbed by the atmosphere after some consecutive interactions without reaching ground level. The *interaction length* represents the average path length a particle traverses in the atmosphere before undergoing a nuclear interaction. For example, a proton that travels vertically through Earth's atmosphere can traverse the equivalent of up to 10 interaction lengths on its way down to the sea level, while heavier elements have shorter interaction lengths that translates into a faster energy loss. On average, the proton will retain approximately 0.001% of its primary energy at the end of its path to ground level for vertical incidence [169].

Operational difficulties to transport big objects up to the space or to the upper layers of the atmosphere set an immediate restriction on the physical dimensions of direct cosmic-ray detectors and their effective areas (≤ 1 m^2) [169]. The observations made with this technique can detect particles with a maximum energy in the interval from dozens of TeV up to 1 PeV. This is a consequence of the constraint on the size of the detectors and that the flux of cosmic rays rapidly decreases beyond PeV energies.

The physical set up of a direct detection experiment typically include one or more of the following detectors:

- *Magnetic spectrometers:* This experimental instruments work by using an intense magnetic field, generated by magnets placed within the experimental arrange, to bend the paths of the incoming cosmic ray particles, and then measuring how much they were deflected as they cross the detector. This information can then be used to measure the main observables like the charge, primary energy or chemical composition [169].

- *Plastic scintillators*: Plastic scintillators emit light when they are exposed to ionizing radiation, such as cosmic rays [199]. The light emission is in proportion to the electric charge and primary energy. These detectors are widely used due to their low cost and easy to mold into different shapes. The implementation of plastic scintillators in an experimental setup is useful in the measurement of the primary energy and the time of flight of charged particles, just to mention a few [199].

- *Emulsion chambers*: These detectors are commonly composed of thick stacked layers of emulsion plates interleaved with target plates or X-ray films, among others [200]. The interaction of a charged particle and the top layers of the detector creates a shower of secondary particles, that is developed through the different layers of the instrument. The three-dimensional evolution of the secondary particle shower is engraved into the emulsion plates in the form of traces and is analyzed to estimate the nature of the primary cosmic ray by the distinctive features left along the detector layers. Also, these traces contain information about the nuclear interactions between the secondary particles and the multiple target plates (or dense matter), and about the direction of the particle. Analogous to the case of extensive air showers, the primary energy is estimated from the recorded density of secondary particles (usually at the lower plates). However, the particle's energy can also be estimated by the radiation length of the particles [199, 200].

- *Calorimeters*: The calorimeters are layered detectors, similar to the structure of an emulsion chamber. The simple structure of a calorimeter consists of layers of very dense materials (absorption layers) interleaved with particle detectors such as scintillators, photomultipliers, and charge detectors among others [169]. These detectors are optimized for measurements of the primary energy and chemical composition. In addition, calorimeters can determinate the primary cosmic ray direction with precision. A cosmic ray that interacts with a calorimeter collides with the multiple detector inner layers, depositing its energy into the detector at each interaction [169, 199].

During the last and current centuries, there have been many experiments developed for the direct observation of cosmic rays. Some of them are the magnetic spectrometers AMS [122], ATIC [201, 202], BESS [203] and PAMELA [121], and the calorimetry experiments CALET [31, 156, 204], CREAM [8, 120, 205], DAMPE [16–18] and NUCLEON [13]. At the moment of the writing of this work, the experiments that are still running operations are AMS-02 [135], CALET, DAMPE and NUCLEON.

3.2 Indirect measurements

As mentioned in Chapter 2, the interaction between a cosmic ray and the air molecules distributed in the atmosphere triggers the production of an EAS of secondary particles that spreads through its way to ground level, where it can be measured by particle detectors distributed over large areas of land. This type of cosmic-ray observations are known as *indirect measurements*, and are applied to detect shower events generated by primaries with energies greater than 10 TeV up to several tens of EeV [95]. However, the reconstruction process of the EAS event and the estimation of the properties of the primary cosmic-ray particle, like kinetic energy or atomic mass, are complex as they heavily depends on the simulation and the correct interpretation of the hadronic interactions involved. Thus, indirect measurements are subject to fluctuations intrinsic to the event modeling and reconstruction. These uncertainties are reflected in the final reconstructions of the shower's main parameters, e.g. the primary energy, or the shower maximum [206].

In general, a ground-based detector can measure different air shower properties such as the lateral density distribution, shower size, shower age, particle content, arrival direction, among others, from which the characteristics of the primary cosmic rays can be inferred, like primary energy and mass composition. According to the science goal of the research team, the indirect experiments are equipped with different kind of detectors tailored to measured several components of the EAS. The detectors are generally located at ground level and are organized in groups. For EAS measurements from ground level, usually the following detection systems are employed:

- *Air fluorescence telescopes:* The air fluorescence telescopes share some characteristics with the IACTs, an improved angular and energy resolutions, and the need for good observing conditions, as cloudless moonless nights. These telescopes measure the emissions of florescence light. These physical phenomena is a result of the interaction between atmospheric nitrogen and the shower's secondary cosmic rays. This process excites nitrogen molecules, thus creating florescence emissions, which are characterized by wavelengths ranging from approximately 290 and 430 nm [207]. This technique does not depend on predictions from interaction models to determinate with accuracy the primary energy of an event. The Telescope Array and the Pierre Auger observatory employ this technique [100, 208].

- *Imaging Air Cherenkov Telescopes (IACT):* These detectors are designed for the observation and recording of the Cherenkov light emissions generated in the air when charged particles of the EAS crosses the atmosphere at speeds exceeding the phase velocity of the light in the atmosphere. Atmospheric Cherenkov light emissions are typical observed for wavelengths between 300 nm and 500 nm. In contrast to the particle arrays, an IACT requires very specific conditions to perform measurements. These include: a cloudless sky without rain, good air quality, and moonless nights to reduce light pollution as minimum as possible [95]. Despite these kind of instruments posses a limited field of view, these instruments have an improved angular and energy resolutions in comparison with air-shower detectors [95]. In addition, IACTs measure the primary energy of the particles that initiate EAS through a detailed analysis of the intensity and shape of the Cherenkov light image captured by the telescope. Some of the observatories that have employed IACT detectors for the observation of cosmic rays are H.E.S.S. [209–211], VERITAS [212, 213], and MAGIC [214, 215]. The Cherenkov Telescope Array observatory (CTA) is a next-generation observatory for astrophysical gamma-rays that will use IACT's at the northern and southern hemispheres, but will also have sensitivity to hadronic EAS [216].

- *Particle detector arrays:* They are composed of clusters of individual particle detectors that are deployed in different geometrical arrangements over large areas at ground level to carry out cosmic-ray measurements at energies where the intensity is low. The detectors that are employed are selected according to the component of the air shower that is going to be studied [95]. The most common types of detectors installed in particle arrays are photomultipliers, scintillator Cherenkov detectors, as well as resistive plate counters, among others. One of the main advantages of the particle detector arrays is their large duty cycle, as they can take data during day and night. In addition, they possess a large field of view, allowing them to survey large portions of the celestial vault over the time. However, the reconstruction of the shower parameters strongly depends on comparisons with hadronic interaction models. HAWC [217], IceTop [218], LHAASO [219], and the Pierre Auger Observatory [100] are indirect cosmic-ray detectors that contain particle detector arrays.

- *Radio antennas:* Tailor-made for the detection of radio frequency pulses, typically inside the frequency interval from 30 to 30 MHz [220, 221], produced by air showers [95], this technique provides another energy calibration method, as well as information about the arrival direction of the primaries. In addition, it allows to measure very inclined air showers. The radio technique is effective for showers with primary energies $\geq$ 100 PeV [220]. Recent technological advances in digital electronics and the improvement in data analysis have increased the accuracy of radio arrays for the study of EAS [222]. In recent years, the implementation of hybrid detection methods, like radio antennas integrated into particle detector arrays, has improved cosmic-ray studies, see for example Pierre Auger [100] and TUNKA-Rex [223]. Finally, LOPES [224] was a pioneer in the implementation of radio antennas for the measurement of cosmic rays, followed by other experiments such as LOFAR [225].

3.3 Cosmic-ray experiments

This section focuses on experiments that have performed measurements of the energy spectrum of cosmic rays for energies 10 TeV $\leq E \leq$ 1 PeV, since this interval is of particular interest to the objective of this analysis. Therefore, a simple overview of the key experiments that have contributed to the understanding of the energy spectrum of TeV cosmic rays is presented.

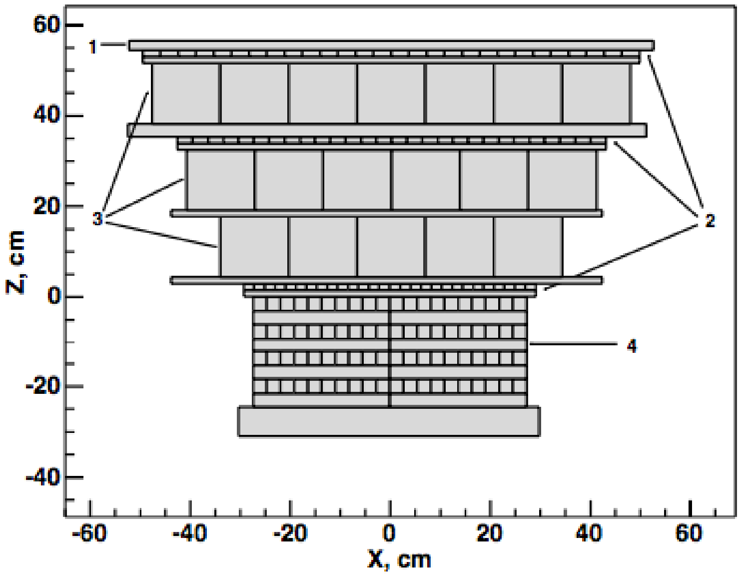

FIGURE 3.1: Diagram of the experimental set up of ATIC. This configuration was employed in the different flights from the ATIC missions. The instrumental components are: a silicon detector for tracking (1), scintillation hodoscopes for triggering and timing (2), a graphite target for particle interactions (3), and a BGO calorimeter for energy measurement. *Image source:* [201].

3.3.1 The Advanced Thin Ionization Calorimeter (ATIC)

Exclusively created for cosmic ray studies, the ATIC mission operated at high altitudes via balloon-borne flights. The purpose of ATIC was to determine the relative abundance and energy spectra of the most representative nuclei of cosmic rays, which include H, He, C, O, Ne, Mg, Si, and Fe, as well as the intensity of all-nuclei for energies $50\,\mathrm{GeV} \leq E \leq 200\,\mathrm{TeV}$ [7, 201]. ATIC design integrated a layered structure including: silicon matrix for precision tracking, fast-response scintillators for event triggering, carbon targets, and a high-density bismuth germanate calorimeter for accurate energy deposition measurement (see Fig. 3.1) [201].

The first experimental mission, known as ATIC-1, was launched on December 28th, 2000 as a flight test [7]. It was concluded that the calorimeter was too thin and could only record a fraction of the primary particle's energy. For the second flight, on December 29th of 2002, the calorimeter was recalibrated and its thermal sensitivity was enhanced. This was the ATIC-2 mission. In December 2005, the launch of ATIC-3 was a failure due to a damage to the air balloon at the takeoff moment [226]. Finally, on December 26th, 2007, ATIC-4 was successfully launched [227].

In particular, the energy spectrum reconstructed from the data obtained by the ATIC-2 mission spans from 100 GeV up to 150 TeV [7]. It was derived by summing the spectra obtained for the different nuclei species measured by the experiment.

3.3.2 DAMPE

Under the name of *DArk Matter Particle Explorer* (DAMPE), this space-borne telescope was specially designed for the measurement of γ-rays and charged particles

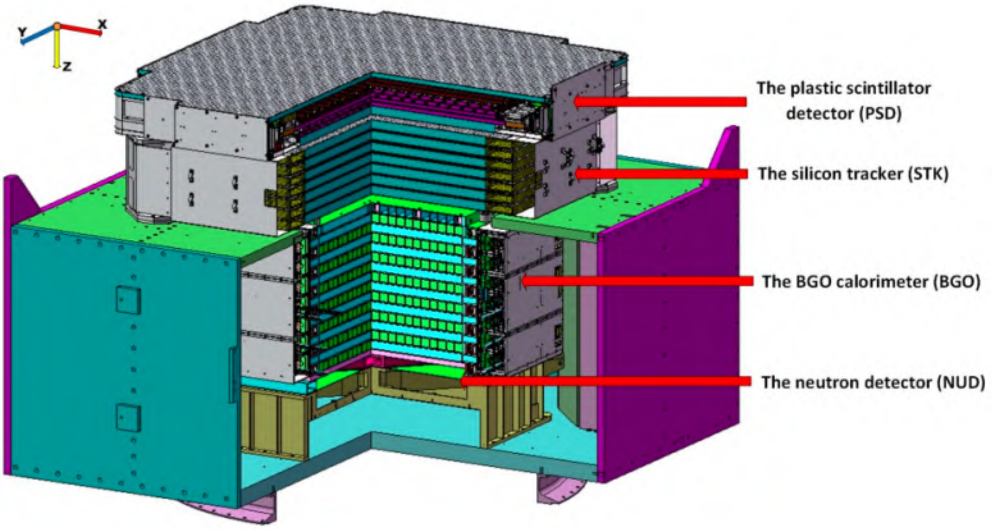

FIGURE 3.2: Graphical representation of the DAMPE detector. The four sub-detector systems are labeled in the image.
Image source: [229].

such as electrons, protons, and heavy ions [228]. It was launched on December 17th, 2015, with the primary mission of identifying possible signatures of dark matter. Its main array has a modular design and consists of four instrumental sub-systems: a bismuth germanium oxide calorimeter, two layers of plastic scintillator, a neutron detector, and a silicon-tungsten tracker (see Fig. 3.2).

Thanks to its instrumental characteristics, DAMPE is sensitive to cosmic rays with primary energies inside the interval $100\,\text{GeV} \leq E \leq 500\,\text{TeV}$ [230]. In the cosmic-ray research field, the DAMPE collaboration has contributed with measurements on the spectra of protons [28], helium [29], and H plus He nuclei [230]. Over the last couple of years, the DAMPE collaboration reported at [231, 232] preliminary results of the total energy spectrum of cosmic rays, highlighting the presence of a spectral feature around 30 TeV. It is expected that this result will support that there exists a knee-like structure located in the TeV energy region (see Fig. 3.3).

3.3.3 NUCLEON

Launched on 26 December, 2014 on board of the RESURS-P satellite (see Fig. 3.4), with a 5-year duty cycle, NUCLEON aims to measure cosmic rays to discover new insights into their physics, among other scientific goals.

The NUCLEON detector has a multi-layer design that includes a hharge measurement system (ChMS) for particle identification, two complementary energy measurement systems: a Kinematic Lightweight Energy Meter (KLEM) system and an ionization calorimeter, and a trigger system. The experimental layout is shown in Fig. 3.4. In particular, the KLEM system module includes carbon targets located on top, and thin tungsten layers that are inserted between six silicon detectors. These modules are employed for determining the primary energy of a cosmic ray by analyzing the angular distribution of secondary particles produced when the particles

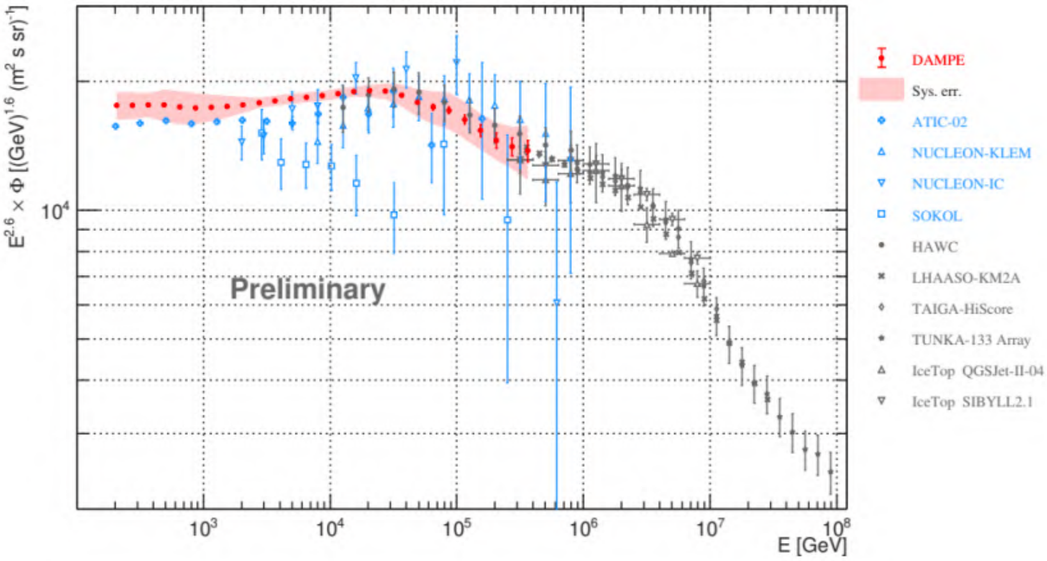

FIGURE 3.3: Preliminary result of the total energy spectrum as measured with DAMPE [232]. *Image Source:* [232].

interacts with a target material [233]. Overall, the instrument was designed to increase the number of secondary particles at the tungsten converter by electromagnetic and hadronic interactions, which are recorded by the ionization calorimeter.

NUCLEON aims to measure cosmic rays to discover new insights into their physics, among other scientific goals. In particular, the NUCLEON experiment measured the cosmic-ray energy spectrum and chemical composition inside the interval 10 TeV $\leq E \leq$ 1 PeV [13, 23].

In 2019, the NUCLEON collaboration reported the reconstruction of the total cosmic-ray energy spectrum in the energy range from 8 to 800 TeV, with evidence of a spectral index change near 10 TeV. This result is shown in Fig. 3.11.

3.3.4 ARGO-YBJ

The Astrophysical Radiation with Ground-based Observatory at YangBaJing (ARGO-YBJ) was an EAS experiment sensitive to cosmic-ray events in the energy range between 3 TeV and 5 PeV, and high-energy γ-rays. It was located in the YangBaJing region of Tibet. ARGO-YBJ began operations in November 2007 and closed in February 2013.

The ARGO-YBJ experimental facility was able to carry out precise measurements of the shower front thanks to its experimental setup and high altitude (4300 m a.s.l.). The central array consisted of a flat layer of 1560 resistive plate counters (RPCs) that covered an area of approximately 5772 m^2 [234], and it was surrounded by a partially instrumented ring-like array, which consisted of 23 clusters, each equipped with 12 RPCs (see Fig. 3.5). In 2007, as part of an experimental campaign of the LHAASO collaboration, two wide-field-of-view Cherenkov telescopes were installed and tested at the ARGO-YBJ facilities [235]. The telescopes and the experiment run in parallel, detecting several cosmic-ray events simultaneously [235, 236].

Two of the most significant contributions from the experiment, was the measurement of the cosmic-ray spectra of $H + He$ within 3 TeV $\leq E \leq$ 300 TeV [238] and

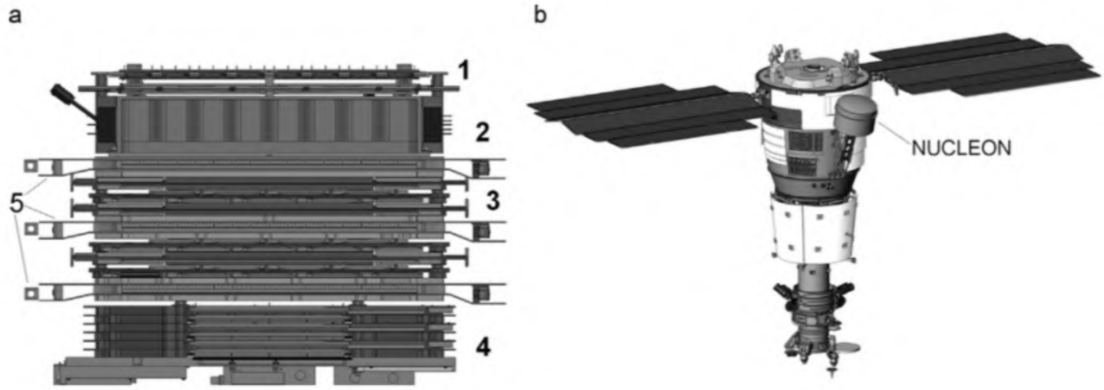

FIGURE 3.4: *Left panel:* Layout of the NUCLEON experiment. The detector was conformed by four silicon detector layers for the spatial measurements and charge determination (1), the KLEM module for the energy measurement (2), silicon detectors alternating with wolfram converters to increase the number of secondary particles (3), six layers of scintillators (5), and the ionization calorimeter (4). *Right panel:* Diagram of the RESURS-P satellite, where the NUCLEON experiment was mounted.
Image source: [13].

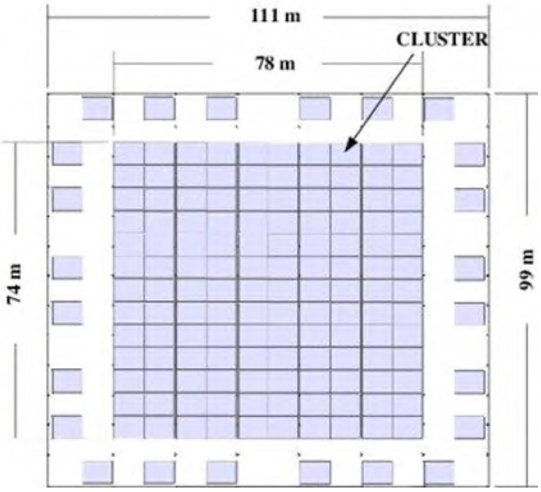

FIGURE 3.5: Representation of the physical distribution of the experimental setup of ARGO-YBJ. Each cluster was composed of 12 RPCs.
Modified from: [237].

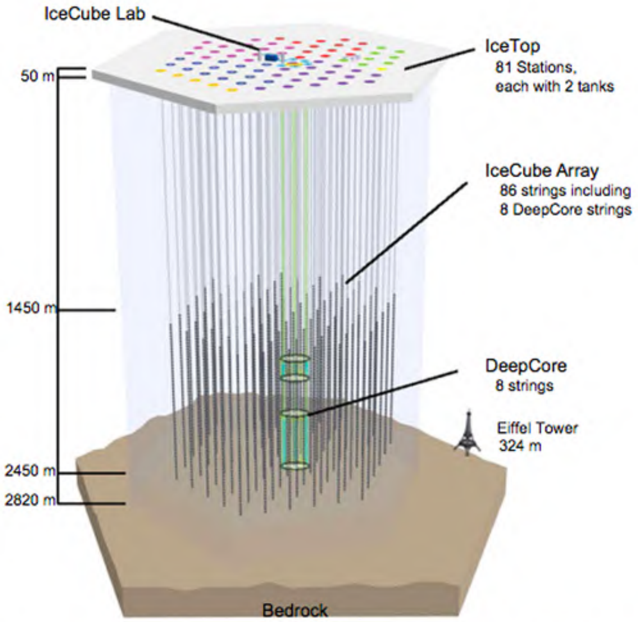

Fig. 1. The IceCube detector with its components DeepCore and IceTop in the final configuration (December 2010).

FIGURE 3.6: This diagram illustrates the main components of the IceCube observatory. The IceTop experimental facility is located in the ice surface above ICECUBE detector.
Image source: [242].

the all-particle component for energies 80 TeV $\leq E \leq$ 20 PeV [239]. This result is shown in Fig. 3.11.

3.3.5 IceTop

The IceCube observatory is an underground neutrino experiment equipped with 5160 optical detectors distributed over a volume of approximately 1 km^3, installed at the Amundsen-Scott South Pole Station, Antarctica. It measures high-energy astrophysical neutrinos by observing Cherenkov emission from their interaction with the surrounding medium [240, 241]. Moreover, it can also measure cosmic rays through IceTop, an outer array of Cherenkov detectors installed above the main array of IceCube. The IceTop site is situated at an elevation of 2835 m, and is composed of 162 Cherenkov tanks contain transparent ice [242]. Each of these tanks has two standard IceCube digital optical modules [242]. The tanks are paired and located at 81 different stations across a surface of 1 km^2. IceTop will undergo an upgrade to include cosmic-ray radio emission detectors and scintillation stations [243, 244].

Due to its characteristics, this detector is dedicated to the study of cosmic rays with energies 100 TeV $\leq E \leq$ 1 EeV [242]. This studies include the measurement of total energy spectrum and complementary analyses of the mass composition of cosmic rays [245, 246]. For the mass composition studies, the observations of IceTop are complimented with the simultaneous information gathered in the IceCube's detectors from the EAS event [246, 247]. Moreover, the reconstructed total energy spectrum of cosmic rays with IceTop from 250 TeV to 10 PeV is reported in [245] , and it is shown in Fig. 3.11 along with other measurements of the spectrum.

3.3.6 KASCADE

The *Karlsruhe Shower Core and Array Detector* was an experimental facility for the measurement of cosmic rays with energies $100\,\text{TeV} \leq E \leq 100\,\text{PeV}$ [248], with the mission to discover the physical phenomena behind the spectral softening at ~ 4 PeV that had been found in the all-particle cosmic-ray spectrum, in addition to measure the individual components of the mass group of cosmic rays within the energy interval $100\,\text{TeV} \leq E \leq 100\,\text{PeV}$ [109, 116]. It performed observations of cosmic rays in the time period from 1996 to 2013. The experiment was located at an altitude of 110.0 m a.s.l., and consisted of an array of 252 scintillation detectors, both shielded and unshielded. The separation between the detectors was 13 m. In addition, KASCADE was sensitive to the electromagnetic, muon, and hadronic components of EAS events due to its calorimeter (placed in the center of the experimental facility) and muon tunnel detector [248]. The different detectors from the array were installed inside an area of 40000 m^2 at the Karlsruhe Institute of Technology (KIT), Germany (1022 g/cm^2).

KASCADE had a major upgrade in 2003 in order to extend its maximum energy observation limit from 10^{17} eV to 10^{18} eV by extending its physical area from 40000 m^2 to 490000 m^2. The expansion was made by the installation of 37 detector clusters across a surface of $700 \times 700\ \text{m}^2$ [115] around the old array. The electronics for the additional detector stations were inherited from the EAS-TOP experiment [115]. After the upgrade, the new array received the name *KArlsruhe Shower Core and Array DEtector with Grande extension* (KASCADE-Grande), and was able to perform cosmic ray studies inside the energy interval from 10^{16} to 10^{18} eV [111, 115, 117].

The KASCADE and KASCADE-Grande analyses of the energy spectrum [109, 111], anisotropies [249], and mass composition [250] of cosmic rays have contributed to a better understanding of the physics of these radiation. In particular, the measurement of the total energy spectrum made with KASCADE demonstrated that the *knee* is a superposition of cutoffs in the individual spectra for different nuclear groups [109]. These cutoffs are proportional to the electric charge of the cosmic ray nucleus times $\text{E}_{knee} \approx 3 \times 10^{15}$. This result is supported by the KASCADE-Grande measurements [111, 116, 117].

The energy spectrum measured with KASCADE [109, 111] is shown in Fig. 3.11, as part of a compilation of spectrum measurements.

3.3.7 TAIGA

The *Tunka Advanced Instruments for cosmic rays physics and Gamma Astronomy* (TAIGA) is ground-base observatory sensitive to high-energy cosmic radiation. Its elevation is 675 m, and it runs operations at the Tunka Valley, Russia. Some of the cosmic ray studies performed with the data from TAIGA are measurements of the energy spectrum and their mass composition. As shown in Fig. 3.8, TAIGA is a hybrid experiment composed of different detector systems of EAS that which operate independently in terms of data acquisition, but are designed to provide complementary and correlated measurements for a complete analysis of EAS events. Here below, we list the main detector systems for cosmic-ray observations that are located at the TAIGA complex [252, 253]:

- **TUNKA-133:** This array covers a surface of 3 km^2, and has a total of 175 wide-angle air Cherenkov telescopes. These telescopes are arranged into 25 clusters (seven detectors per cluster). Each cluster has its own trigger system that allows it to work as a single array. The clusters are separated by 85 m from

FIGURE 3.7: Physical location of KASCADE in Karlsruhe, Germany. In the photo, the central detector (central building) and the 252 scintillation detector stations (white boxes) are shown [251].

each other. TUNKA-133 studies events with energies within the interval from 6×10^{15} eV to 1×10^{18} eV [254]. From 2012 to 2019, TUNKA-133 also operated with 63 radio antennas. This array was known as TUNKA-Rex, and is sensitive to cosmic rays in the energy interval $100\,\mathrm{PeV} \leq E \leq 1\,\mathrm{EeV}$ [255].

- **TUNKA-Grande:** The components of this array are scattered inside the physical area of TUNKA-133 and it consists of 19 scintillation stations. The physical area of each scintillation station is 10 m^2. TUNKA-Grande also has 8 underground muon counters. Its scientific goal is to measure cosmic rays within the $10\,\mathrm{PeV} \leq E \leq 1\,\mathrm{EeV}$ energy range [256, 257].

- **TAIGA-HiSCORE:** The *High Sensitivity Cosmic Rays and gamma Explorer* measures the Cherenkov emission from the air showers with its wide-field optical stations composed of 4 PMTs each. TAIGA-HiSCORE has a total of 120 stations installed within an area of 1.1 km^2, and is divided into four clusters. It is sensitive to cosmic rays that have energies ranging from approximately 20 TeV to 1 EeV [258, 259].

TAIGA has provided measurements of the spectrum of the all-particle component of cosmic rays through individual or simultaneous observations from its different detector systems [261]. In particular, TUNKA-Grande contributes to the measurement of the total energy spectrum within $1 \times 10^{16}\,\mathrm{eV} \leq E \leq 1 \times 10^{18}\,\mathrm{eV}$ [262]. Moreover, the measurement of the spectrum with TUNKA-133 ranges from 6×10^{15} eV to 1×10^{18} [263], meanwhile the corresponding measurement from TAIGA-HiSCORE covered the energy interval from 2×10^{14} eV to 1×10^{17} eV [259]. Finally, the combined observations from TUNKA-133 and TAIGA-HiSCORE extends from 2×10^{14} to 1×10^{18} eV [259].

The individual results from TUNKA-133 and TAIGA-HiSCORE were selected for the compilation of spectra measurements made for this work (see Fig. 3.11).

3.3.8 TIBET

The TIBET experiment was constructed in 1990 in the region of Yangbajing, Tibet at an altitude of 4300 m. This observatory is mainly dedicated to gamma-ray observations for energies between 3 TeV and 450 TeV approximately [264], and cosmic-ray

FIGURE 3.8: The TAIGA observatory is a hybrid detector composed of different arrays: TUNKA-133, TUNKA-Grande, TAIGA-HiSCORE, and TAIGA-IACT. Images of these detector systems are shown in the pictures above.
Image source: [260].

measurements between 10^{14} and 10^{17} eV [265, 266]. The TIBET contributions to astroparticle physics include the analysis of the chemical composition of elemental cosmic rays [267], their arrival direction anisotropies [268], and the measurement of the cosmic ray energy spectrum [265]. In particular, TIBET measured the energy spectrum of cosmic rays around *knee* provided valuable data for understanding this phenomenon, helping to determine whether this spectral feature is caused by limits on particle acceleration in galactic sources or by propagation effects [266]. It has gone through different construction stages: TIBET-I (1990), TIBET-II (1994), TIBET-III (1999) [265]. The TIBET-III configuration consists of 761 fast-timing (FT) counters with one Hamamatsu H1161 fast-timing photomultiplier (FT-PMT) each, 28 density counters (D), and 249 sets of detectors each equipped with one Hamamatsu H1161 density photomultiplier (D-PMT), distributed over an octagonal grid with an area of 36900 m^2 as observed in Fig. 3.9. The FT counters consist of a plastic scintillator contained within a steel housing, and coupled to a photomultiplier. Meanwhile, the D counters are also scintillation detectors, but they are optimized for measuring particle density in an EAS event. Similar to FT counters, these are a plastic scintillator coupled to a density photomultiplier (D-PMT), but are designed to have a larger detection area and measure all of the emitted photons by the particles [269].

Among different results, the TIBET collaboration has reported measurements of the total energy spectrum within 100 TeV $\leq E \leq$ 100 PeV using data from the TIBET-III experimental array, assuming different composition abundances of the primary cosmic rays [265]. In addition, it has studied the influence on the reconstructed all-particle spectrum of cosmic rays by the implementation of different hadronic interaction models [265].

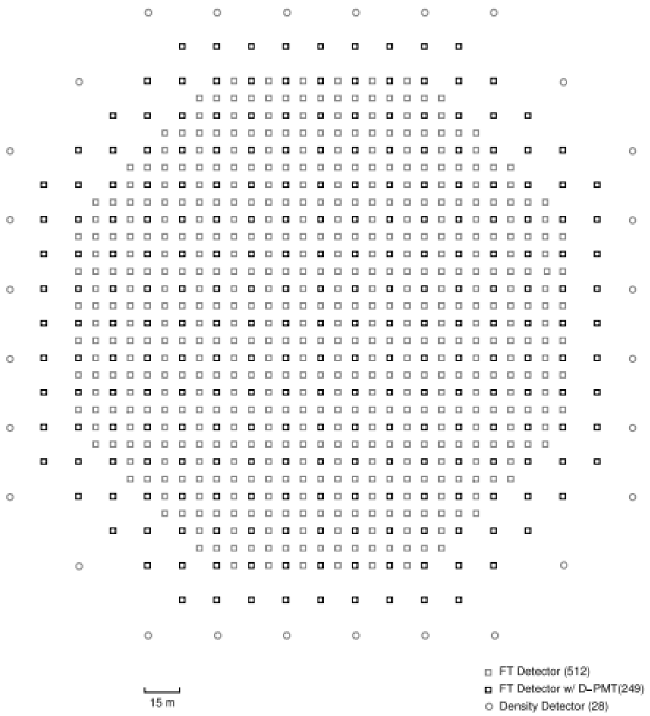

FIGURE 3.9: Layout of the TIBET-III detector. The core of the array is an ensemble of 512 standard FT detectors (light squares) and 249 FT detectors equipped with a D-PMT (dark squares), distributed in a surface of 36900 m^2. The central array is surrounded by 28 density detectors (circles).
Image source: [265].

3.3.9 LHAASO

The *Large High Altitude Air Shower Observatory* is an operational high-altitude hybrid experiment [20] that measures cosmic ray events within the $1\,\mathrm{TeV} \leq E \leq 1\,\mathrm{EeV}$ energy interval, and TeV-PeV gamma rays. The construction stage of LHAASO began in 2017, and the complete deployment and installment of all of its different components ended in 2021 [20].

The complete experimental setup of LHAASO consists of three detector arrays [20]:

KM2A: This is an array of 5195 electromagnetic particle detectors (EDs) distributed over an area of 1 km^2 optimized for gamma-ray observations above 10 TeV energies. The array also includes 1188 muon detectors (MDs). The EDs are composed of plastic scintillator, and designed for the measurement of the density distribution of charged particles in an EAS. In addition, the MDs are RPC detectors for the measurement of the muon density in EAS events. The sensitivity of the KM2A complex for cosmic ray detection covers the energy interval from 10 TeV to 100 PeV [20].

WCDA: The *Water Cherenkov Detector Array* is distributed over a surface of $78,000$ m^2 and 3120 detector units (each unit has two PMTs facing upwards) distributed among three ponds filled with ultra-pure water: WCDA-1, WCDA-2, and WCDA-3. Along with the KM2A array, the WCDA is optimized for gamma-ray observations, however, both arrays can also record hadronic air showers. For cosmic rays, the WCDA has an energy threshold of approximately 1 TeV [270].

WFCTA: The *Wide Field-of-view Cherenkov Telescope Array* is composed of 18 IACTs, mainly designed for the measurement of the primary energy of cosmic rays from 10 TeV to 100 PeV [20]. The 18 IACTs are distributed within the total area of the observatory, next to the WCDA. These instruments, are calibrated to observe cosmic-ray events ranging from 10 TeV - 1 EeV [271].

The spatial distributions of the KM2A, WCDA, and WFCTA detectors in LHAASO are shown in Fig. 3.10.

The LHAASO collaboration has made significant breakthrough contributions on high-energy astroparticle physics, especially in the gamma-ray field [272]. Regarding the study of cosmic rays, The LHAASO collaboration has recently presented results on the reconstruction of the all-particle spectrum within $0.3\,\mathrm{PeV} \leq E \leq 30\,\mathrm{PeV}$ [114]. Moreover, this analysis included measurements of the mean logarithmic mass, $\langle \ln A \rangle$, relevant for mass-composition studies. These measurements are important because they contributed with experimental constrains on models that describe the propagation of cosmic rays and their sources. For example, the variation of $\langle \ln A \rangle$ with energy can indicate changes in the composition of cosmic rays, and it can suggest the presence of different sources or acceleration mechanisms, like the observed spectral bump in proton and helium data that is likely caused by a source in our galactic neighborhood [273].

To conclude this chapter, a compilation of some of the most relevant measurements of the total energy spectrum is shown in Fig. 3.11. Here, the energy range under consideration spans from 1 TeV to 10 PeV. It is evident that, below the knee, most of the observations have poor statistics, with exception of the recent high-precision measurements made by the HAWC and NUCLEON experiments, which have begun to fill the gap between direct and indirect measurements. Therefore, there is a

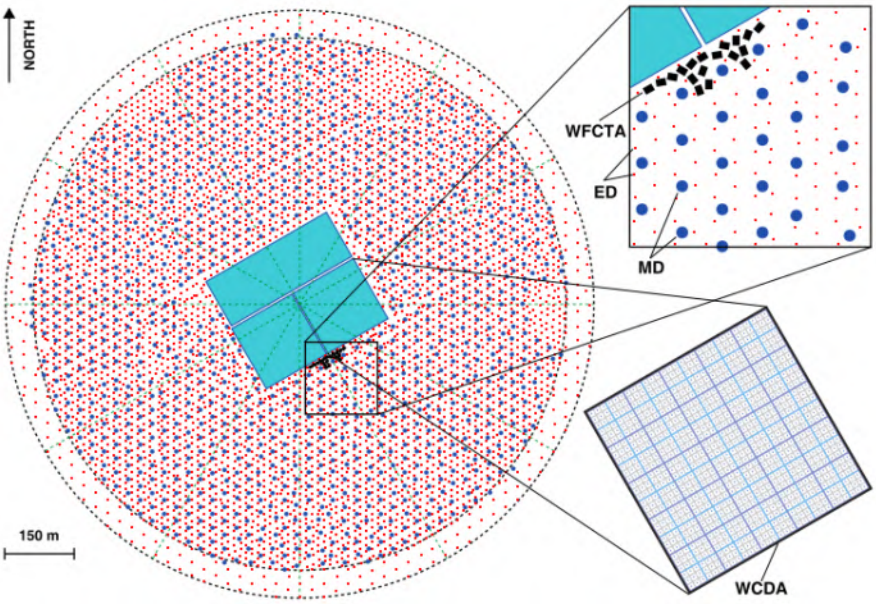

FIGURE 3.10: Layout of LHAASO's experimental facility. The WCDA (light blue rectangle) complex detector is placed at the central region, while the WFCTA (black squares) is installed southeast, near the periphery of the WCDA. In addition, the MDs (blue circles) and the EDs (smaller circles in red) are distributed around the WCDA.
Image source: [20].

clear need to obtain additional measurements with high precision and statistics in this energy range, in order to deepen our knowledge of the physical phenomena that occur within it. Therefore, to increase the understanding of cosmic rays within 10 TeV $\leq E \leq$ 1 PeV, it is essential to perform high-precision and high-statistics measurements, which will help to validate theoretical models, and the potential discovery of new phenomena in this energy region. The characteristics and main contributions of the HAWC observatory are detailed in the next chapter.

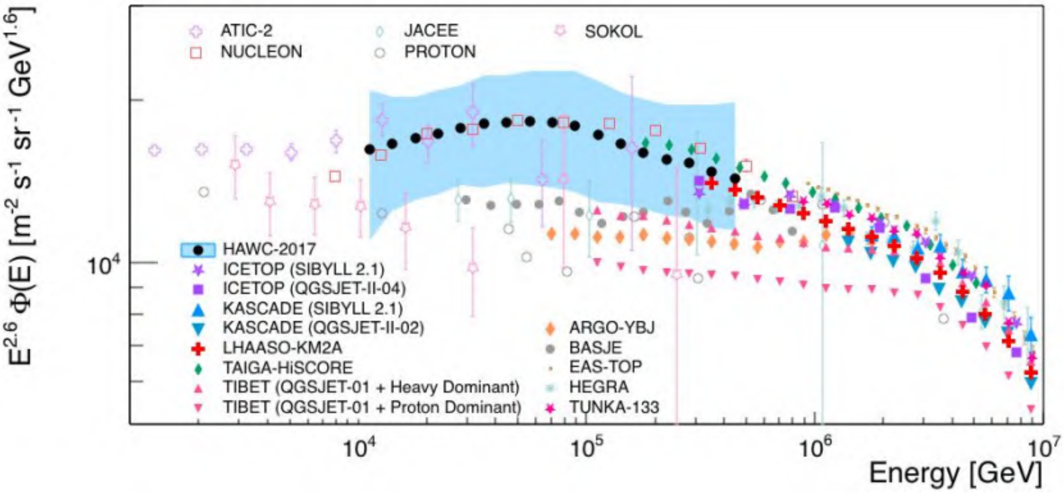

FIGURE 3.11: Here, ATIC-2 (light violet open crosses) [7], JACEE (light teal open diamonds) [274], NUCLEON (red open squares) [23], PROTON (gray open circles) [5] and SOKOL (light pink open stars) [275], ARGO-YBJ (orange full diamonds) [239], BASJE (gray full circles) [15], EAS-TOP (brown dots) [276], HEGRA (cyan asterisks) [277], ICETOP (SYBILL 2.1, violet full stars; QGSJET-II-04, violet full squares) [245], KASCADE (QGSJET-II-02, down-facing full triangles in azure; SYBILL 2.1 full up-facing triangles in light azure) [109, 111], LHAASO-KM2A (red full crosses) [114], TAIGA-HISCORE (teal diamonds) [259], TIBET (QGSJET-01 + Heavy Dominant, up-facing full triangles in pink; QGSJET-01 + Proton Dominant, down-facing full triangles in pink) [265] and TUNKA (pink full stars) [263]. Also, the energy spectrum measured by HAWC from the analysis of [22] is shown as reference (black full circles) with its corresponding systematic error band in blue. All the measurements were multiplied by $E^{2.6}$ to enhance and visualize their features. For all data points, the vertical error bars correspond to statistical uncertainties.
Modified from: [278].

Chapter 4

The High Altitude Water Cherenkov observatory

Motivated by the progress made with the Milagro observatory in the field of very-high-energy (VHE) gamma-ray astronomy using the water Cherenkov technique [279], the High Altitude Water Cherenkov observatory (HAWC) was planned as a new generation experiment with a modular arrange of water Cherenkov detectors (WCDs) for the detection of EAS, sensitive to VHE gamma-rays and high-energy cosmic rays, in particular those with TeV energies.

HAWC detects the Cherenkov light created by secondary charged particles from electromagnetic and hadronic EAS as they interact with the WCDs. To maximize the potential of this technique, HAWC needs to be installed at the highest altitudes as possible, where the amount of secondary gamma rays and electrons is higher. This is one of the reasons of why it was decided to install the HAWC observatory at the Pico de Orizaba National Park (19° N, 97° W) in Puebla, Mexico [19]. The construction of HAWC was carried out through different stages thanks to its modular design. The first phase began in 2011, consisting of the assembly of 30 WCDs on site, and was finished in September 2012. The installation of additional WCDs was kept until the goal of 300 detectors was achieved. The complete array of HAWC oficially started operations in March 2015 and is expected to end by 2027, although a possible time extension is expected [217].

Since 2015, HAWC has been continuously taking data and surveying the high-energy universe. With exhaustive analyses of the measured data, the HAWC collaboration has contributed significantly to the comprehension of astrophysical γ- and cosmic rays. Some of the most relevant contributions made by the HAWC collaboration are:

- The discovery and study of galactic TeV sources of gamma rays like TeV halos such as the extended regions around Geminga and Monogem pulsar [280, 281], PeVatrons such as the regions HAWC J2019+368 and HAWC J2016+371 associated with the Dragonfly nebula and the SNR CTB 87, respectively [282, 283], the HAWC J2227+610 region linked with SNR G106.3+2.7 [284], the star cluster Cygnus OB2 [90], and our galactic center [142]. Moreover, HAWC has observed very-high-energy gamma-ray emissions from pulsars such as the CRAB [49, 285]. HAWC has also discovered gamma rays with TeV energies emitted by the Sun [286]. HAWC has observed TeV gamma-ray emissions from microquasars like SS 433 [287], V4641 Sgr [143] , which are considered as possible hadronic acceleration regions. In addition, it has observed TeV gamma rays from extragalactic sources, in particular, AGNs like Mrk 421, MRK 501 [288, 289], VER J0521+211 and 1ES 1215+303 [290], and M87 [291].

- The detection of +100 VHE gamma-ray sources for the first time, which are reported in the latest *Third HAWC Catalog of Very-high-energy Gamma-Ray Sources* (3HWC) [292].

- The measurement of the energy spectrum, mass composition and arrival directions of cosmic rays at TeV energies. For example:
    - The measurement of the energy spectrum of the all-particle component with HAWC. The first measurement of spectrum was published in 2017 [22]. This result covered the energy range 10 TeV $\leq E \leq$ 500 TeV, and it was reconstructed with 8 months of HAWC data using the Bayesian unfolding technique as the main method [50–52]. Following an update to the spectrum study, the results were published in early 2025 [278]. The updated analysis presents the measurement of the total spectrum extended up to 1 PeV using a larger data sample of HAWC (5.3 years of effective observational time), and an updated set of MC simulations and reconstruction algorithms, reconstructed with the same unfolding technique. Both measurements of the spectrum reveal a new spectral feature at $\log_{10}(E/\mathrm{GeV}) = 5.9 \sim 4.6$ that resembles the *knee*.
    - The measurement of the light mass group (H + He) energy spectrum between 6 and 158 TeV, using the Bayesian unfolding [124].
    - The report of a composition model of cosmic rays using HAWC data [26]. From this composition result, the corresponding spectra for the different mass groups of cosmic rays were derived, including protons, helium, and heavy nuclei ($Z > 2$) within 10 TeV $\leq E \leq$ 1 PeV [26]. The analysis was performed with the Gold unfolding method [293].
    - An analysis of the cosmic arrival distributions of cosmic rays in the energy interval 2.0 TeV $\leq E \leq$ 72.8 TeV. This energy-dependent anisotropy is characterized by a dominant dipole moment primarily at 2.0 TeV $\leq E \leq$ 30 TeV [294]. Furthermore, HAWC and IceCube collaborated on a joint observation of the cosmic-ray anisotropies in the arrival direction, using data from both Earth's hemispheres. These observations were conducted for energies around 10 TeV [295].

- Contribute to frontier physics with experimental evidences. Some of the leading analyses in this area include the search for the violation of Lorentz Symmetry, and the search for cosmic radiation traces linked to dark matter [296, 297]. While no definitive confirmations of these scenarios have been found, HAWC analyses have placed significant constraints on the parameters of these models.

It is important to mention that HAWC it is currently part of multi-wavelength sky survey campaigns with other existing experiments to map the VHE universe. In these campaigns, the experiments survey the sky in different wavelengths and types of particles (such as neutrinos and cosmic rays), expanding the current understanding of the physics around high-energy steady and transient phenomena.

In particular, HAWC takes part in the *Astrophysical Multimessenger Observatory Network* (AMON) [298]. Other participating experiments include IceCube [218], Pierre Auger Observatory [299], Fermi-LAT [300], LIGO [301], and Virgo [302], among others. This network enables coordinated follow-up observations of interesting events, such as gravitational wave detections and neutrino emissions from active galactic

FIGURE 4.1: The HAWC observatory, its geographic location is in Puebla, Mexico, at a saddle on the slopes of the Sierra Negra Volcano. The Pico the Orizaba Volcano, covered by the snow, is observed in the background, as well as traces of an old lava eruption from the volcano. *Image credit:* HAWC collaboration.

nuclei (AGN), leading to a more comprehensive understanding of these phenomena [298, 303].

4.1 Particle detector array and electronics

The experimental facility of the HAWC gamma-ray and cosmic-ray observatory is installed in a saddle at the slopes of the Tliltepetl (Sierra Negra) volcano, next to another volcano, which is known as Ciltlatepetl[1] (Pico de Orizaba), both located in the *Parque Nacional del Pico de Orizaba*, Mexico (see Fig. 4.1). The primary detector array of HAWC is composed by a compact modular arrangement of 300 WCDs filled up with ultra-pure water (each filled with $\sim$ 180000 liters of water), distributed over a flat area of 22000 m^2 (with 62% of physical coverage) at an altitude of 4100 meters (637 $\mathrm{g/cm}^2$ of grammage or 17.4 radiation lengths) [217]. This is a privileged position since it is near the position of the maximum development of TeV events, increasing its sensibility to detect these events and to measure in detail the lateral spread of the EAS. With a wide FOV of 2 sr at any moment, HAWC is able to map two-thirds of the sky in a time-lapse of 24 hours.

In addition, the compact distribution and modular design of the WCDs, the large physical coverage of the experiment, its high altitude, and the number of detectors, enhance HAWC's capability to measure in detail the lateral distribution of secondary particles at ground level, and to successfully discriminate gamma-ray induced EAS from hadronic events [49, 124, 217, 285, 304].

---

[1] The Nahuatl words Tliltepetl and Ciltlatepetl mean *black mountain* and *star mountain* in english, respectively.

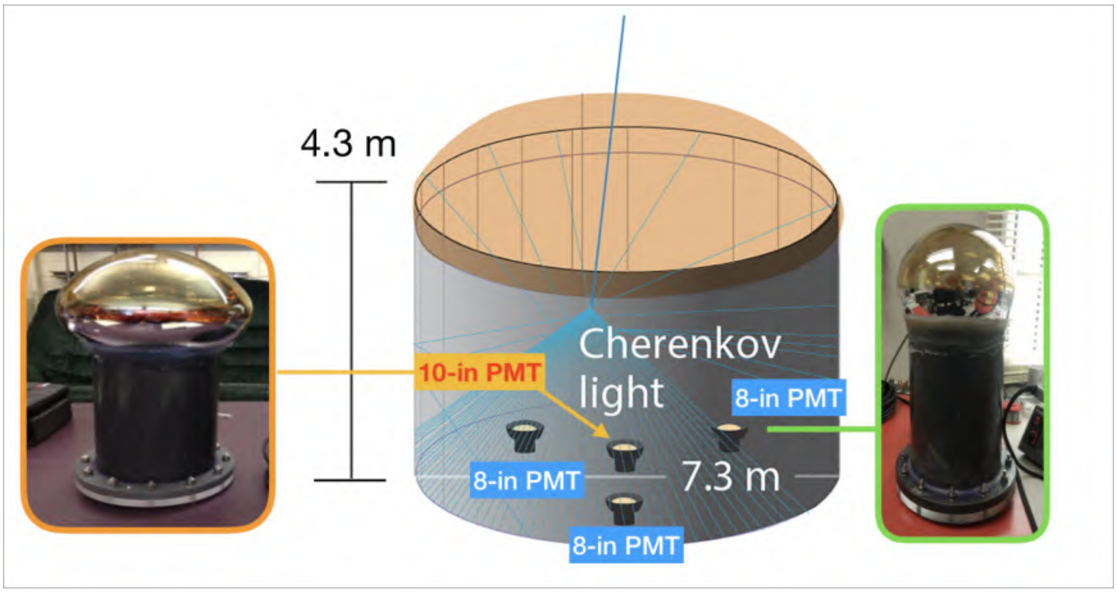

FIGURE 4.2: Each WCD is 4.3 m high, and have 7.3 m in diameter. The inner bladder can hold $\sim 180,000$ L of ultra-pure water [217]. The image shows a close-up to an 8-inch Hammamatsu R5912 PMT. *Image credit:* HAWC collaboration.

4.1.1 Water Cherenkov detectors and photomultiplier tubes

The WCDs are cylindrical structures fabricated with steel sheets coated with Zn [217], and sheltered with a vaulted vinyl polyester fabric roof to protect them from rain, snow, and other weather phenomena. Each WCD is 4.3 m high, and have 7.3 m in diameter. The WCDs are set apart from each other by at least 0.6 m. Each WCD has a polyethylene bladder in the interior to store around 180000 L of ultra-pure water, and to prevent water leakage.

Inside the WCDs, the relativistic particles produce Cherenkov light, which is measured by the photomultiplier tubes attached at the bladder's base [217]. The PMTs are enclosed by the bladder to protect them from external light, ensuring accurate measurements of the Cherenkov light. In particular, HAWC is equipped with two PMT models: an 8-inch Hammamatsu R5912 with 340 cm^2 of photocathode area, and a 10-inch Hammamatsu R7081 with 530 cm^2 of photocathode area [305]. The 8-inch PMTs were donated by the MILAGRO collaboration [217]. In total, HAWC has 900 8-inch PMTs in addition to 300 10-inch PMTs.

In particular, each WCD has three Hammamatsu R5912 PMTs anchored at the bottom of the tank in an equilateral triangle grid, with an additional Hammamatsu R7081 PMT anchored at the center of the array [217] (see Fig. 4.2). The 10-inch PMT enhances HAWC's response and sensitivity to low energy shower events due to its larger photocathode area [217].

Each PMT has a semi-conductive film, known as photocathode, at the top (see Fig. 4.2). The interaction between the photocathode and the Cherenkov photons produces free electrons, according to the photoelectric principle, which are accelerated towards a chain of dynodes placed at the center of the tube by a high voltage potential applied between the dynodes [306]. Both PMT models have a 10 stage dynode chain [217, 305]. In particular, the interaction of an incoming electron and the first dynode produces a shower of new electrons into the second dynode, where the process is repeated and the electron channel is amplified and accelerated towards the third dynode, and so on until the tenth plate of the dynode chain [306]. All the electrons that were generated in this process are collected at the anode, and their signal is sent to the PMT output channel via an RG-59 coaxial cable to HAWC's data acquisition center (DAQ) [217]. Due to their nature, one single air shower event can spread and cover large distances and therefore interact with multiple WCDs.

4.1.2 Cherenkov radiation

This type of radiation was first proposed by the English physicist Oliver Heaviside by the year of 1888 [307, 308] and later on it was experimentally observed by Pavel Alekseyevich Cherenkov [309], in whose honor this type of radiation receives its name.

The Cherenkov is generated by an electrically charged particle, such as e^-, with relativistic speed u as it makes its way accros a transparent medium with a characteristic refraction index n [86, 148]. The particle's interaction with the medium generates Cherenkov radiation, which is emitted in a small cone concentric to the propagation trajectory of the particle (see Fig. 4.3), with an emission angle given by:

$$\cos\theta = \frac{c}{un} = \frac{1}{\beta n}. \tag{4.1}$$

In the above expression, c represents the speed of light in the vacuum. The term β corresponds to the velocity of the particle relative to c inside the dielectric (β=u/c) [86, 95]. For example, for water $n = 1.33$, then, and a charged particle with a travel speed $u \approx c$, the Cherenkov light will be emitted at $\theta \sim 41°$. Cherenkov radiation represents a minor portion of the total energy lost by charged particles in the medium ($\approx 0.1\%$). This is significantly less than ionization energy loss, which is the dominant energy loss mechanism.

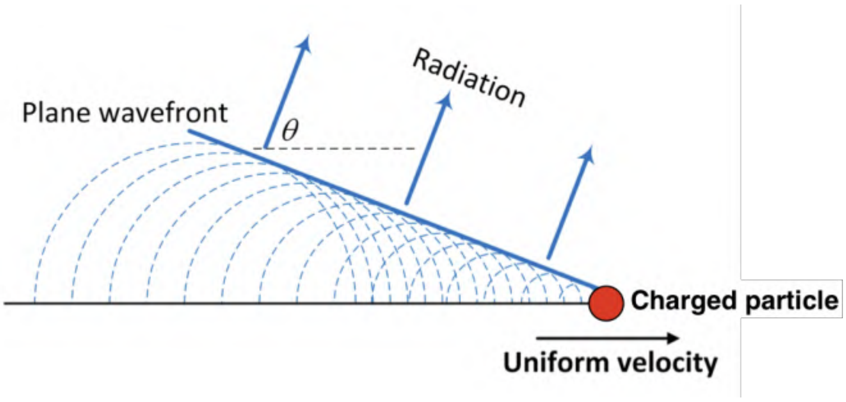

FIGURE 4.3: Sketch of the conical wave fronts of Cherenkov light generated from an electrically charged particle that moves across a dielectric with a velocity greater than the phase velocity of light within the same medium. In here, the emission angle of the Cherenkov radiation is represented by θ. It is observed that θ is relative to the trajectory of the charged particle *Image source:* [310].

Moreover, the phase velocity of the particle in the medium, β, is a key factor for Cherenkov production. The emission of this radiation in a transparent medium happens if β is grater than $1/n$ (see Eq. (4.1)) [86].

As mentioned before, the HAWC observatory employs the water Cherenkov method for the EAS measurement at ground level. In particular, HAWC records the radiation produced relativistic charged particles from the air shower, mostly $e^{\pm}$, as they propagate through the WCDs. For an electron, the threshold kinetic energy for the emission of Cherenkov photons is described by [86]:

$$E_{th} = 511 \ \ keV \left[\left(1 - \frac{1}{n^2} \right)^{1/2} - 1 \right]. \tag{4.2}$$

An electron produces N_f photons proportional to the path length traveled l [86]:

$$N_f = 2\pi \cdot z^2 \cdot \alpha \cdot l \cdot \left(\frac{1}{\lambda_2} - \frac{1}{\lambda_1} \right) \cdot \left(1 - \frac{1}{\beta^2 n^2} \right). \tag{4.3}$$

Here, z represents the particle charge, n is the refractive index of the medium, while λ_1 and λ_2 are the minimum and maximum wavelengths of the emitted radiation, respectively. Lastly, α is the constant of fine structure.

Moreover, the total quantity of photons produced by an electron can be expressed in terms of the emission angle θ (Eq. (4.1)):

$$N_f = 2\pi \cdot z^2 \cdot \alpha \cdot l \cdot \left(\frac{1}{\lambda_1} - \frac{1}{\lambda_2} \right) \cdot sin^2(\theta). \tag{4.4}$$

Table 4.1 presents a list of the parameters for the production of Cherenkov photons by means of an electron in two different mediums, air and water, respectively.

Parameter	Air	Water
Refraction index	1.00029	1.33
Emission angle	∼1.3°	∼41°
Energy threshold	21 MeV	263 keV
Photons emitted per meter	∼ 27	∼ 40000

TABLE 4.1: Cherenkov radiation production parameters for an electron in air and water as mediums [86, 217, 311].

4.2 Data Acquisition System

The DAQ electronics are located inside the *counting house*, right in the heart of the physical array of HAWC. Here, the *front end boards* (FEBs) process the signals sent by the PMTs generated by the detection of the shower particles [217]. First, the analog electronics receive the signal from the PMT output channels, where it is amplified and shaped. The electronics include a Time over Threshold (ToT) circuit. The ToT compares the incoming signal with two characteristic voltage limit values [217]:

- 1/4 photoelectrons (PEs), that corresponds to the low threshold,
- and 4 PEs for the high voltage threshold.

When the signal crosses one of the thresholds, the ToT generates a distinctive pulse as an output, whose amplitude is related to the time a signal spent above the specified threshold. For instance, if the input signal exceeds the lower threshold, the output from the ToT circuit will be a two-edge signal, T_0 marks the signal pass-through the threshold and T_1 when the signal falls through it. Analogously, for the

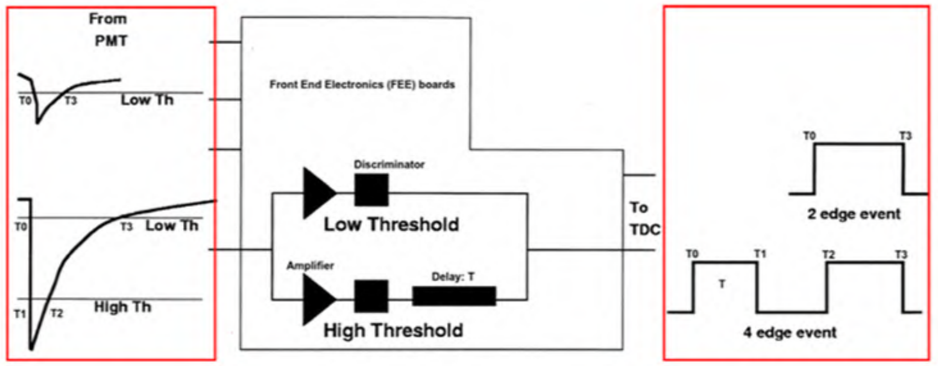

FIGURE 4.4: The left diagram shows two different PMT signals crossing the low threshold (top) and the high threshold (bottom), respectively. The central panel is the ToT circuit, where the signals are amplified and processed. Finally, the right panel shows the two-edge (top) and four-edge (bottom) output signals, respectively. *Image source:* [217].

higher threshold, the output will be a four-edge signal, T_0 and T_3 correspond to the times when the signal crosses the lower threshold (going up and down, respectively), while T_1 and T_2 correspond to the times when the signal exceeds the higher threshold up and down, respectively (see Fig. 4.4). The output is stored at a Time Digital Converter (TDC), which also converts the processed signal into a binary system. As a final step, the information is transferred to a server physically located on the site.

HAWC operates continuously day and night, meaning a large data payload. For this purpose, the on-site servers run a software trigger criterion for a fast event selection to lower the data flow from a rate of ∼450 MB/s down to ∼20 MB/s. Only an event that hits at least 28 PMTs (from the active PMTs that are available at the moment of the detection) in a time window of 150 *ns* is logged in a *raw* format for its posterior offline analysis and shower reconstruction. The corresponding trigger rate is 25 *kHz* [217, 312]. On average, HAWC's measurements generate 1.7 TB of data per day.

4.3 Data offline reconstruction

Once the *raw* data has been successfully saved into hard drives, the next step is to reconstruct the shower parameters for gamma and hadron-induced showers [22, 49, 124, 304]. Within the HAWC collaboration, this process is known as offline reconstruction. The reconstruction procedures for these observables are described next.

4.3.1 Core position

At the observation plane, the shower core is the region with the highest particle density. In general, the particle density at the EAS plane decreases as the distance to the core increases. These information is crucial for reconstructing the properties of the primary cosmic ray that initiated the shower, such as its energy and arrival direction. Thus, it is a primordial task to reconstruct the shower core with the lowest bias possible as it stands as the cornerstone for the subsequent air shower reconstruction steps. In HAWC, the reconstruction algorithm of the core position takes the lateral distribution of an event as an input, and the lateral distribution is defined as the Q_{eff} distribution with respect to the lateral distance from the shower core within the shower front plane [49].

To provide a quick estimation of the shower core position, the lateral distribution of the deposited charge of the event is fitted with a modified NKG-like function using the χ^2 minimization method, the *Super Fast Core Fitter*, defined as [304]:

$$S_i = S(A, \vec{x}, \vec{x}_i) = A\left(\frac{1}{2\pi\sigma^2}e^{-|\vec{x}_i-\vec{x}|^2/2\sigma^2} + \frac{N}{(0.5+|\vec{x}_i-\vec{x}|/r_0)^3}\right). \tag{4.5}$$

In the above expression, $\vec{x}$ is position vector of the shower core, while S_i corresponds to the recorded signal at a given $i-th$ PMT that is triggered by the event, $\vec{x}_i$ is the position vector of the i-th PMT, and A is the amplitude of the function. The Molière radius is given by $r_0 = 124.21$ m (approximate value at HAWC site). Here, σ = 10 m and $N = 5{\cdot}10^5$.

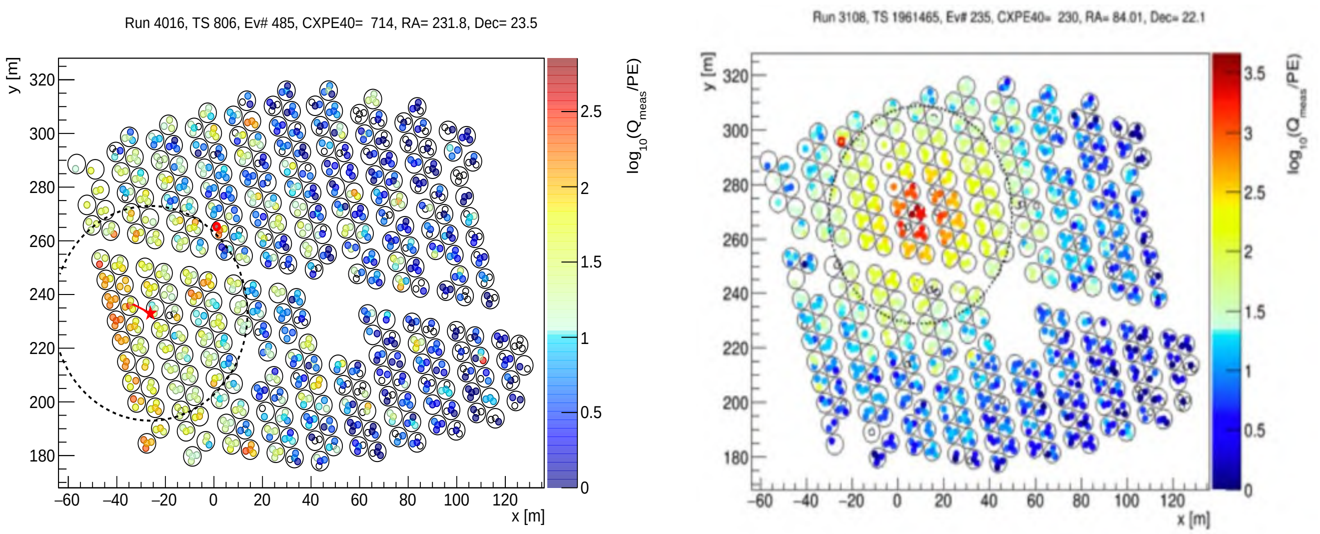

FIGURE 4.5: *Left panel:* Effective charge distribution observed in HAWC for an hadronic induced EAS with an energy of $\log_{10}(E/\mathrm{GeV}) = 4.9$. *Right panel:* Same, but for a gamma ray induced EAS and an energy of $\log_{10}(E/\mathrm{GeV}) = 4.7$. In both panels, each WCD is represented by the big circles, while each PMT and its corresponding position at the detector are illustrated by the smaller circles. For both events, the reconstructed shower core position is represented as a red star. The core is located within the dotted circle with a radius of 40 meters. The color gradient represents the base 10 logarithm of the effective charge of the hits within the event. *Image source:* [313].

4.3.2 Arrival direction

In HAWC, the arrival directions of the shower events are reconstructed from the measured arrival time distributions, respectively. Near the shower axis, the relativistic secondary particles travel longitudinally in directions similar to that of the primary, creating a flat shower front. However, the secondaries that are further from the shower axis undergo more scattering interactions and attenuation as they traverse longer leaned depths through the atmosphere. The later creates a curved

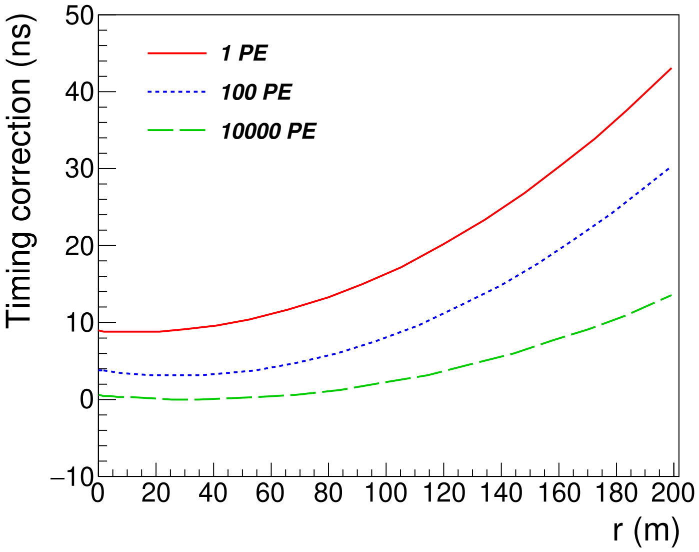

FIGURE 4.6: Timing correction, $T(r, Q_{\text{eff}})$, as a function of the radial distance of the measured signal to the shower core and the effective charge, Q_{eff}, which is applied to the arrival time distributions of the EAS during the reconstruction procedure to estimate the arrival direction of the shower events. The curves correspond to the timing correction performed over the arrival times of shower events for 1 PE (red curve), 100 PE (blue dashed curve), and 10000 PE (green long-dashed curve). *Image source:* [278, 316].

shower front [314, 315]. In addition, the arrival times of the leading particles that are detected by the electronics of the detectors are affected by statistical fluctuations, modifying the curvature of the EAS front and the estimation of the primary cosmic-ray direction [304]. This is known as a *sampling* effect. Thus, the measured arrival time distributions must be corrected for the curvature/sampling effects that cause time delays for hits in the shower front tail by means of a correction term $T(r, Q_{\text{eff}})$ [316] for the correct estimation of the EAS arrival direction. $T(r, Q_{\text{eff}})$ is a function that relates the effective charge, Q_{eff}, of the observed hits to their radial distance, r, from the shower core. The algebraic expression of $T(r, Q_{\text{eff}})$ was established through detailed studies of simulated air showers, and the parameters of the functional form were optimized using measured data [49, 278, 304].

After the measured arrival time distributions are corrected for the curvature and sampling effects, the shower front is fitted fitted to a plane with a χ^2 minimization to estimate the arrival direction angles of the EAS event [49, 304], namely the azimuthal and zenithal angles, represented by ϕ and θ, respectively.

4.3.3 Energy reconstruction

The primary energy of hadronic showers is estimated by using a maximum likelihood procedure [22], which compares the measured lateral distribution of the EAS secondary particles to MC templates for proton-induced EAS[2] at different zenith angles. The production of the MC templates was performed under the framework of

---

[2] According to [317, 318], the galactic population of TeV cosmic rays are dominated by the proton mass group. Therefore, this energy estimator is calibrated with these primaries.

the simulation software distribution CORSIKA [319], using the simulation packages for hadronic interactions FLUKA [320] and QGSJET-II-03 [321, 322] (for hadronic energies $E_h < 80$ GeV and $E_h \geq 80$ GeV, respectively) with primary energies 70 GeV $\leq E \leq 1.4$ PeV and zenith angles $0^\circ \leq \theta \leq 70^\circ$.

The MC templates predict the likelihood that the observed lateral distribution of charged particles are produced by protons of different energies. The probabilities are computed and then stored in tables composed by 3 zenith bins ($\theta \in [0^\circ, 16.8^\circ]$, $[16.8^\circ, 35.2^\circ]$, $[35.2^\circ, 60^\circ]$), 40 effective charge, Q_{eff}, bins ($Q_{eff} \in [1, 10^6]$ PE, whit a bin width of $\Delta Q_{eff} = 0.15$), 44 primary energy bins ($E \in$[70 GeV, 1 PeV], with $\Delta \log_{10}(E/\mathrm{GeV}) = 0.1$), and 70 radial bins ($R \in [0, 350]$, with $\Delta R = 5$ m).

For a measured EAS event, a probability value is assigned to every PMT,drawn from the previously mentioned tables, representing the likelihood of its observed signal. The PMTs with no signal at all during the EAS measurement also contribute with a probability value. To estimate the shower energy, a likelihood function is estimated for each possible energy by multiplying the probability values of all PMTs. The optimal energy estimator corresponds to the energy bin at which the likelihood is maximal [22, 124].

The base 10 logarithm of the primary energy, measured in eV units, estimated with the algorithm is stored in the variable called

```
rec.protonlheEnergy
```

This variable is used in the analysis of the reconstruction of the total energy spectrum of cosmic rays. Further details about the energy estimator for cosmic ray events can be found in [22].

The Monte Carlo simulations employed in the present analysis of the energy spectrum measured with HAWC were generated with the implementation of simulation package QGSJET-II-04 for high-energy hadronic interactions [48]. The detector response, the trigger and detection efficiencies necessary for unfolding the measured energy spectrum were derived with these simulations. In addition, the final energy scale of the unfolded differential intensity was calibrated with QGSJET-II-04. Furthermore, the QGSJET-II-04 simulations were also employed to study the impact of the event selection criteria, and to evaluate the systematic uncertainties present in the reconstruction of the energy spectrum. These particular set of QGSJET-II-04 MC simulations are detailed next.

4.3.4 Monte Carlo simulations of extensive air showers at HAWC

As the understanding of the HAWC detector and the physics involved are improved, the reconstruction software is updated and refined. These different versions of the processing are often referred to as "passes" or with a representative name. Each new pass typically incorporates improvements to the algorithms used for calibration, event reconstruction, background rejection, and energy estimation.

The simulated data set employed for the unfolding procedure described in this doctoral thesis were generated using the fourth version of the HAWC data reconstruction software, known as *pass4*, with the *daqsim* configuration that was produced to analyze the systematic uncertainties intrinsic of the PMTs [49]. These simulated data set are an updated version compared to the ones used in the analysis from [22]. With the selection of these MC simulations, it was possible to lower the total systematic uncertainty in the unfolded result when compared to [22]. In addition, as further improvement, the study was performed using the simulation package QGSJET-II-04 for high-energy hadronic interactions [48]. The MC simulations were generated for zenith angles smaller than 65° with CORSIKA v7.40 [319] using the hadronic interaction models FLUKA [320] and QGSJET-II-04 [48] for hadronic energies $E_h < 80$ GeV and $E_h \geq 80$ GeV, respectively. Meanwhile, HAWC's response to the passage of EAS particles was simulated with GEANT4 [323].

According to direct measurements made by CREAM I-II [8, 205], PAMELA [121] and AMS-2 [324, 325] of the cosmic radiation and their chemical abundance, the most representative atomic nuclear species are: ^{1}H, ^{4}He, ^{12}C, ^{16}O, ^{20}Ne, ^{24}Mg, ^{28}Si and ^{56}Fe. Thus, these eight nuclei species were simulated in HAWC. The primaries were reproduced with $5\,\text{GeV} \leq E \leq 3\,\text{PeV}$ using an energy spectrum that follows a power-law of the type E^{-2}. The cores were uniformly distributed over a circular area of radius equal to 1000 m centered at HAWC.

At this stage, the simulated distributions for the different mass groups don't describe any natural physical scenario, thus to represent more realistic distributions the simulated data is weighted with the Software for Weighting Events and Eventlike Things and Stuff (SWEETS) [326, 327] to model a flux with more realistic energy/spatial distributions. In particular, with SWEETS, the energy spectra of the individual mass groups in MC simulations are weighted after the cosmic-ray mass composition model of cosmic rays described in [22]. The sweets.IWgt variable is used for weighting purposes in the MC data sets. The cosmic-ray data measured by CREAM I-II [8, 205], PAMELA [121] and AMS-2 [324, 325] (see Fig. 4.7), were fitted with a broken power-law function. The results from the fit were employed to parametrize the corresponding weights for each mass group, respectively. The equation for the broken power-law function is [22]:

$$\Phi(E) = \begin{cases} \Phi_0 \left(\frac{E}{E_0}\right)^{\gamma_1} & \text{if } E < E_{\text{break}}, \\ \\ \Phi_0 \left(\frac{E_{\text{break}}}{E_0}\right)^{(\gamma_1 - \gamma_2)} \cdot \left(\frac{E}{E_0}\right)^{\gamma_2} & \text{if } E \geq E_{\text{break}}, \end{cases} \tag{4.6}$$

where Φ_0 is a normalization constant, E_{break} defines the energy at which the spectral break occurs, γ_1 is the spectral index before the break E_{break}, and γ_2 is the corresponds to the spectral index after E_{break}. For the fit, the parameter E_0 was set to a constant value of 1×10^{11} eV for H and He primaries, respectively. In addition, for the C, O, Ne, Mg, Si, and Fe nuclear species fits the corresponding values are 1200, 1600, 2000, 2400, 2800, and 5600 [22, 328]. Additional details of the fitting procedure the readers can refer to [328].

This is the cosmic-ray mass composition model of references [22, 124], and from this point the term *nominal composition model*[3] will be coined to refer to it throughout this work, and will be used for the nominal calculations presented in this work.

From Fig. 4.7 it is possible to observe hardenings in the energy spectra for the elemental mass groups of the nominal model at energies $\log_{10}(E_{\text{rec}}/\text{GeV}) < 4.0$. These phenomena are observed in the data from CREAM I-II [8, 205], PAMELA [121] and AMS-2 [324, 325], and have also been measured by ATIC-2 [329], CALET [30, 330], and DAMPE [232]. The origin of these spectral structures is uncertain, however there are different theoretical models that propose scenarios for their origin based on experimental evidence. These models can be grouped into 3 categories:

- acceleration at the source or new galactic sources [331–336].
- propagation through the ISM [337–340].

---

[3] or *nominal model* for short.

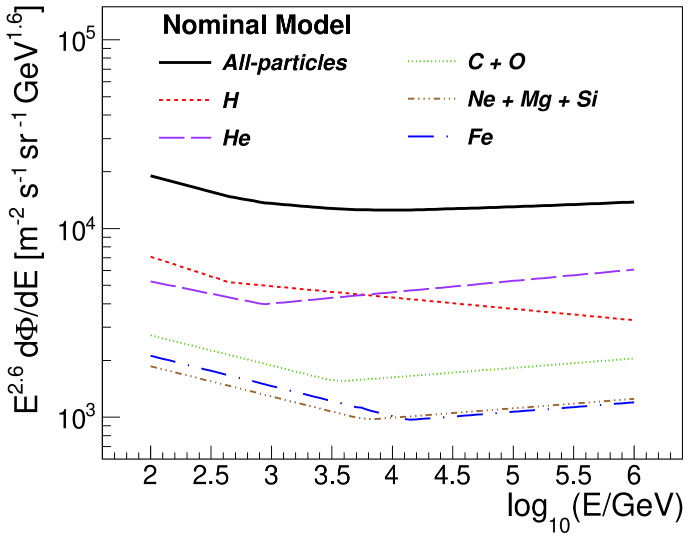

FIGURE 4.7: The above spectra for protons (dashed lines), helium (long-dashed line), C+O mass group (dotted line), Ne+Mg+Si nuclei (dash dot dot dot line), and iron (dash-dotted line) are derived from our nominal cosmic-ray mass composition model [22, 124]. In addition, the total energy spectrum is shown (bold line). *Image source:* [278].

- nearby sources [341, 342].

In addition to the nominal composition model, other alternative descriptions of the mass composition of cosmic rays were employed in the present study for the analysis of systematic uncertainties (see Chapter 6). These are the Polygonato model [343], the GSF model [344], and two models calibrated with ATIC-2 data [317], and ATIC-2 plus JACEE measurements [345], respectively. For consistency, the cosmic-ray composition models chosen for this study are the same as those used in the H+He spectrum analysis [124].

The *pass4−daqsim* simulations were produced with a total of 3×10^{10} and 1.3×10^{10} showers induced by hydrogen and helium nuclei, respectively. Moreover, a total of 1×10^9 showers were generated for each of the remaining mass groups.

At HAWC, the experimental data and MC simulations are reconstructed using the same algorithm and format.

4.3.5 Observables

The experimental and simulated data files contain multiple information stored in different fields, like the EAS observables per event for physics analysis, or information on the detector performance. Both experimental and simulated data files contain fields with the prefix *rec* for reconstructed variables. The names and descriptions of the main reconstructed EAS observable that we employed for the analysis will be shown below:

rec.angleFitStatus This variable reflects the outcome of the angular reconstruction process, with values of 0 (successful), 1 (failed), 2 (there is no information available), and 3 (the method failed to find a stable solution).

rec.coreFitStatus This variable allows to recognize the event that had a successful shower core reconstruction (with a value of 0), from those that doesn't (with a value of 1).

rec.coreFiduScale Related to the physical dimensions of HAWC, this scale factor indicates the landing point of the shower core within the detector array. It is useful to separate *on-array* from *off-array* events. For example, to select only off-array events, one would choose rec.coreFiduScale > 100.

rec.coreX Related to the reconstructed core physical coordinates at HAWC's observation level, this variable stores the corresponding X coordinate. It is computed with the coordinate system of HAWC, measured in meters.

rec.coreY Related to the reconstructed core physical coordinates at HAWC's observation level, this variable stores the corresponding Y coordinate. It is computed with the coordinate system of HAWC, measured in meters.

rec.CxPE40XnCh This variable is helpful to distinguish on-array events, and it is estimated as the number of activated channels within 40 m of the shower core.

rec.nChAvail This variable stores how many HAWC channels were active at the moment when the event was detected.

rec.protonlheEnergy Base 10 logarithm of the reconstructed primary energy, as obtained with the log-likelihood method (see 4.3.3), measured in eV.

rec.zenithAngle The air shower zenith angle is stored in here. This observable is measured in radians.

rec.azimuthAngle The air shower azimuth angle is stored in here. This observable is measured in radians.

Moreover, the prefix *mc* is employed for the variables that contain the true simulated values of the physical quantities of each EAS event. In addition, the *sweets* prefix is employed to distinguish the weights generated with the SWEETS software, exclusive to MC simulations. The variables *mc* and *sweets* are only found in the Monte Carlo data sets of HAWC. Here is a list of the most representative ones:

mc.coreX This is a variable defined for MC EAS events that represents the core's true X physical coordinate at HAWC's observation level. It is computed with the coordinate system of HAWC, measured in meters.

mc.coreY The core's true Y position of of MC events at ground level. It is computed with the coordinate system of HAWC, measured in meters.

mc.corsikaParticleId This variable stores the corresponding tag for each primary particles in MC simulations that is used internally in CORSIKA. For example,

mc.logEnergy Represents the true energy (in GeV units) of the primary particle that triggered the simulated EAS. of the MC air-shower event. It is expressed as a base 10 logarithm.

mc.zenithAngle True arrival zenith angle of the simulated primary particle that triggered the EAS (radians).

Primary Particle	mc.corsikaParticleId
Proton	14
Helium	402
Carbon	1206
Oxygen	1608
Neon	2010
Magnesium	2412
Silicon	2814
Iron	5626

mc.azimuthAngle True arrival azimuth angle of the simulated primary particle that triggered the EAS (radians).

sweets.IWgt This weight, produced by SWEETS, is applied to simulations in order to reproduce the nominal composition model (see section 4.3.4) with an isotropic flux.

4.3.6 Selection Criteria

The position of the core, the direction of arrival, and the primary energy are some of the most relevant reconstructed shower observables for this analysis, which are susceptible to systematic effects that can propagate to the energy spectrum and distort it. To minimize the systematic effects, the HAWC experimental and simulated data were treated with a set of specific selections designed to minimize the impact of these uncertainties. The majority of these cuts were developed and applied in the earlier analysis of the total spectrum with HAWC [22]. Some of those event selection conditions were modified for this analysis like that over the zenith angle, in addition, we also imposed additional cuts, for example, on the numer of PMTs that were hit.

The set of conditions imposed for the event selection in this analysis and their descriptions are listed below:

- **rec.angleFitStatus** $= 0$ **& rec.coreFitStatus** $= 0$ These cuts select events for which the shower core and arrival direction were successfully reconstructed.

- **rec.nChAvail** > 0**.** This cut removes events that have no available channels registered.

- **rec.CxPE40XnCh** ≥ 40**.** Events are selected if they triggered at least 40 channels within a 40 m radius of the EAS core. Only EAS events that were reconstructed within the physical area of the observatory were selected, in addition to those events whose from which the core was reconstructed within 20 m of the HAWC border are included.

- **rec.zenithAngle** $\leq 35^\circ$**.** Only those EAS that have $\theta \leq 35^\circ$ are selected. This angular range was proposed and discussed in a Cosmic-ray group call [346], since it increases statistics and reduces systematic uncertainties at high energies by including more inclined showers, which are less susceptible to PMT saturation near the core in comparison to the first HAWC analysis [22].

- **rec.nHit/rec.nChAvail** ≥ 0.2. This cut reduces migration effects at low energies and improves the energy resolution around 10 TeV. Only the events within the region of HAWC's maximum trigger efficiency are selected. The low-energy EAS with large fluctuations are ruled out with this cut.

- 3.8 $\leq$**(rec.protonlheEnergy-9)**$\leq$ 6.15.

  This cut restricts the analysis to events within the energy range where the trigger and reconstruction efficiencies are higher, removing low-energy ($\leq$ 6.3 TeV) and high-energy events ($\geq$ 1.4 PeV).

4.4 Precision in the reconstruction of the EAS observables

The quality of the selected data was evaluated through an analysis of the average of the bias distribution (mean bias) and the 68% containment value of the bias distribution (resolution) of the arrival direction, shower energy, and EAS core position versus the base 10 logarithm of the measured primary energy using the nominal simulated data set. The bias was calculated as the difference between the input (true) and reconstructed values of an observable for a given MC event, and the mean bias is just the average of the bias distribution for a given energy interval. Only for the primary energy, the standard deviation of the bias distribution corresponds to the resolution.

From now on, the *rec* subscript will stand for the **reconstructed** variable.

4.4.1 Angular bias and resolution

The angle, Ψ, amid the true and rec shower axes defines the angular bias, and it was estimated by means of the following formula

$$\Delta\Psi = \cos^{-1}[\sin\theta_{rec}\sin\theta\cos(\phi - \phi_{rec}) + \cos\theta\cos\theta_{rec}]. \tag{4.7}$$

Here, the shower's true arrival direction is expressed as the unit vector $\overrightarrow{\alpha}$ with its corresponding azimuth angle ϕ and zenith angle θ. And the reconstructed arrival direction is represented by the unit vector $\overrightarrow{\alpha}_{rec}$ with its corresponding angles θ_{rec} and ϕ_{rec}. Figure 4.8 shows the average of the bias distribution and the resolution of the shower's arrival direction against the base ten logarithm of E_{rec}. At 6.3 TeV $\leq E_{\mathrm{rec}} \leq$ 1.4 PeV, the average of the angular bias distribution is smaller than 0.52°, while the angular resolution is less than 0.33°.

4.4.2 Precision in the reconstruction of the core position

The average of the core position bias distribution is computed according to:

$$\Delta R = \sqrt{(X - X_{rec})^2 + (Y - Y_{rec})^2}. \tag{4.8}$$

In the above expression, the X and Y variables correspond to the true ordered pair that describe the position of the EAS core at the observation level, while (X_{rec}, Y_{rec}) are the corresponding reconstructed coordinates.

Fig. 4.9 shows the average of the bias distribution corresponding to the EAS core position and the 68% containment of the EAS core bias distribution versus the base ten logarithm of E_{rec}. From here, it is observed that both quantities are less than 18 m for energies 6.3 TeV $\leq E_{\mathrm{rec}} \leq$ 1.4 PeV.

In addition, Figs. 4.8 and 4.9 indicate an increasing behavior of the bias at the highest energies ($E_{rec} >$ 100 TeV), derived from the action of two effects. The first one is attributed to the air shower front extending beyond the central detector array,

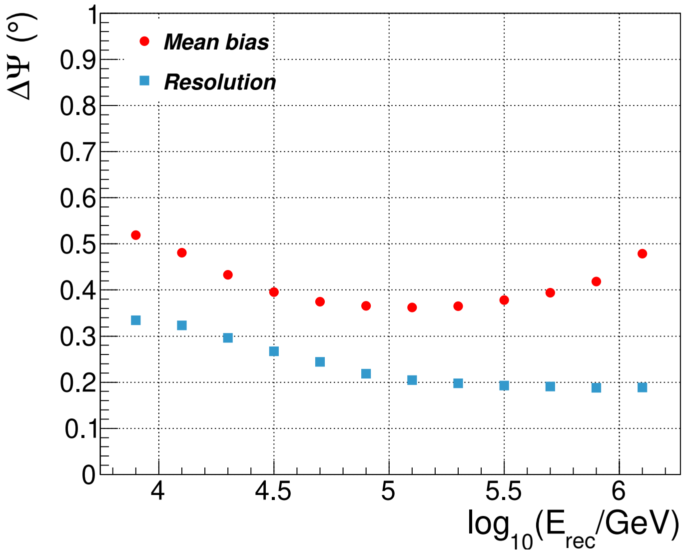

FIGURE 4.8: Predicted average of the bias distribution (full circles in red) and resolution (full squares in azure) for the shower's arrival direction against the base ten logarithm of E_{rec}. The plot was created using the nominal simulated data set with the predictions from QGSJET-II-04 and the nominal composition model from section 4.3.4, after applying selection cuts. *Image source:* [278].

and the second is a consequence of a cut that rules out PMTs with effective charges above 10^4. These PMTs are primarily near the shower core.

4.4.3 Precision in the reconstruction of the primary energy

Finally, Fig. 4.10 shows the estimated mean bias and the one-sigma errors on the measured primary energy in a base ten log scale against the measured primary energy, as predicted by the QGSJET-II-04 simulations. The bias is defined as

$$\Delta \log_{10}(E) = \log_{10}(E) - \log_{10}(E_{rec}). \tag{4.9}$$

In the above expression, the true energy of the primary cosmic ray that triggered the simulated EAS is represented by E. In particular, within the energy interval $6.3\,\text{TeV} \leq E_{\text{rec}} \leq 1.4\,\text{PeV}$, the average bias for $\Delta \log_{10}(E_{\text{rec}})$ ranges from -0.01 up to $+0.15$, with a resolution between $+0.1$ and $+0.33$. While both bias and resolution generally improve with energy, the bias increases slightly near 1 PeV.

4.5 Experimental data

The measured data analyzed in this work has a total effective time of $\Delta t = 1932$ days. The events were collected in the time lapse from June 11th, 2015 to December 31st, 2020. The experimental data used in this analysis were processed using the *pass4* reconstruction.

The EAS events from the measured data sample were selected according to the conditions listed in section 4.3.6.

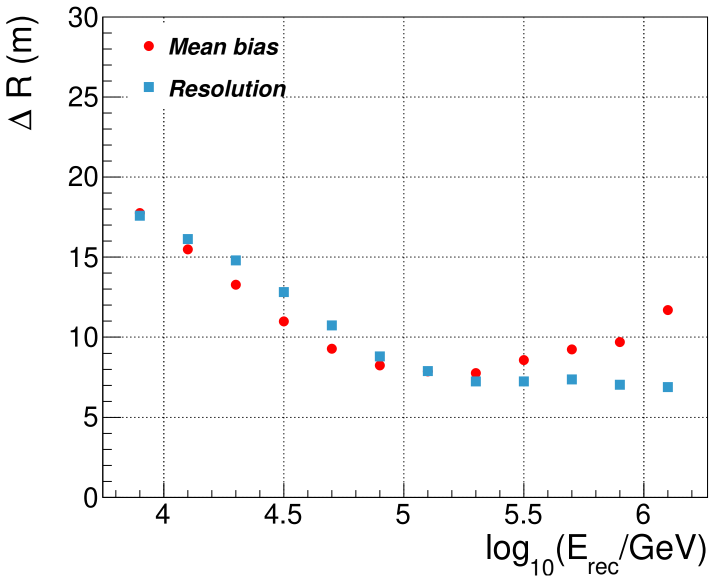

FIGURE 4.9: Predicted average of the bias distribution (full circles in red) and resolution (full squares in azure) of the shower core position in HAWC against the base ten logarithm of E_{rec}. The plot was created using the nominal simulated data set with the predictions from QGSJET-II-04 and the nominal composition model from section 4.3.4. *Image source:* [278].

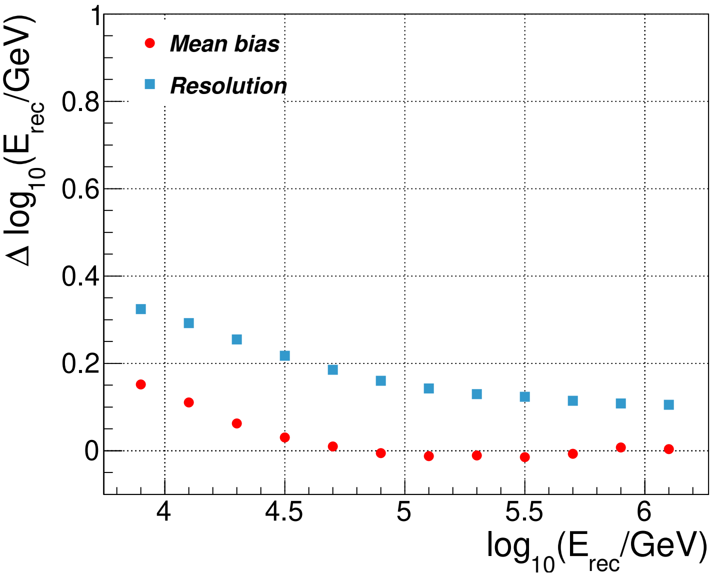

FIGURE 4.10: Predicted average of the bias distribution (full circles in red) and one sigma error (squares) for the estimated energy in logarithmic scale versus $\log_{10}(E_{\text{rec}})$. The plot was created using the nominal simulated data set with the predictions from QGSJET-II-04 and the nominal composition model from section 4.3.4, after applying the selection criteria from section 4.3.6. *Image source:* [278].

TABLE 4.2: The selection efficiency is presented as the percentage of the relative change in event counts after the application of two successive selection cuts, for both simulated and measured data computed with the nominal composition model.

Selection parameter	Relative change in the event counts after the application of two successive selection cuts [%] MC simulations	 HAWC data
Trigger	100%	100%
Arrival direction and shower core reconstruction	100%	94.9%
$N_{\mathrm{r}40}$	8.1 %	6.6%
Zenith angle	81 %	79.5%
Fraction hit	30.3 %	35.2%
Estimated EAS energy	62.3 %	64.9%

Before the implementation of the selection criteria, the selected experimental data sample had a total of 4.1×10^{12} EAS events, and after the selection criteria, such sample remained with 4.7×10^{10} EAS events. The final events in the data sample represent 1.1% of the original size of the sample.

To quantify the efficiency of the selection criteria, the percentage of the relative change in the event counts after the application of two successive selection cuts was estimated for both measured and MC data. The corresponding results are shown in table 4.2. From here, it is observed that the application of each successive cut yields comparable efficiencies for both data sets, with only small differences.

It is important to mention that in the analysis of the H + He spectrum measured with HAWC [124], the analysis of the selection efficiency yielded similar results, and the observed differences, particularly in the values of the fraction hit , $N_{\mathrm{r}40}$, and the estimated EAS energy selections, were attributed to the shape of the spectrum. This effect was also quantified in [278] for this analysis. While the true energy spectrum from the MC simulations follows a flat distribution, the spectrum from the measured data does not, thus the true energy spectrum was weighted accordingly to the ratio between the measured and simulated detection rates in order to recreate the observed distribution [278]. With this modification, the selection efficiency analysis for the MC simulations was repeated, and the following list shows the percentage of the relative change in the event counts after the application of two successive selection cuts

- Trigger → 100 %.
- Successful reconstruction of the shower core → 100 %.
- Successful reconstruction of the arrival direction → 100 %.
- $N_{\mathrm{r}40}$ → 7.5 %.

- Zenith angle → 79.5 %.
- Fraction hit → 34.8 %.
- Estimated EAS energy → 64.3 %.

Moreover, the results for the measured data are more consistent with the predictions from these results. This observation is proof that the behavior of the spectrum is related to the selection efficiencies.

In addition, the bias due to the variations in the predictions from different mass-composition models (c.f. section 4.3.4) was also studied. It was found that the uncertainty from the mass composition of cosmic rays has a small effect in the selection efficiencies as it can be seen in table 4.3.

TABLE 4.3: The selection efficiencies for the MC simulations computed with the nominal composition model (see Fig. 4.7) are compered to the results derived with the composition models described in section 4.3.4.

Selection parameter	Relative change in the event counts after the application of two successive selection cuts [%]				
	Nominal simulations	ATIC-02	GSF	JACEE	Polygonato
Trigger	100%	100%	100%	100%	100%
Arrival direction and shower core reconstruction	100%	100%	100%	100%	100%
N_{r40}	8.1%	7.9%	8.1%	8.7%	9.1%
Zenith angle	81%	80.3%	80.9%	81.2%	81.5%
Fraction hit	30.3%	32.1%	30.6%	29.1%	28.1%
Estimated EAS energy	62.2%	63.3%	62.5%	61.2%	60.2%

The reconstruction of the energy distribution of the measured events after applying the quality selection (c.f. section 4.3.4), and in the description of the unfolding technique employed to obtain the total energy spectrum with HAWC data are described in the next chapter.

Chapter 5

Unfolding method for the reconstruction of the all-particle energy spectrum

In the present study, the energy spectrum of the all-particle component of cosmic rays measured with HAWC is reconstructed though the implementation of the Bayesian unfolding [50–52] that has already been employed in previous cosmic-ray analyses of the spectrum in HAWC [22, 124]. The main characteristics of this method are described in this chapter. In addition, the Bayesian unfolding method is applied to the MC simulations to validate its implementation to the measured data.

5.1 Energy spectrum reconstruction

The reconstruction of the energy spectrum without taking into account statistical fluctuations or detector effects can be summarized as follows: the measured energy distribution (see Fig. 5.1, top panel), or raw energy histogram, is built from the selected HAWC data sample mentioned in section 4.5. Then, the number of events in each energy bin of the raw histogram is divided by the corresponding width of that energy bin, the effective lifetime period, the solid angle of detection, and the effective area of the instrument in order to transform it into an energy spectrum. This can be computed with the formula

$$\Phi_{\mathrm{raw}}(E_{\mathrm{rec}}) = \frac{N(E_{\mathrm{rec}})}{\Delta E_{\mathrm{rec}}\,\Delta t\,A\,\Delta\Omega}, \tag{5.1}$$

where $N(E_{\mathrm{rec}})$ corresponds to the total number of cosmic ray events contained in a given reconstructed energy bin centered at E_{rec}, while ΔE_{rec} represents the width of the corresponding reconstructed energy bin, $\Delta t = 1.66946 \times 10^8$ s , and $A = 34371\ \mathrm{m}^2$ is the fiducial area of the detector after the selection criteria from section 4.3.6. Finally, $\Delta\Omega = 1.14$ sr. Fig. 5.1, top panel, shows the reconstructed energy distribution from the selected HAWC data sample, where it is compared to the reconstructed energy distribution from the nominal model using MC simulations, which is plotted with an error band that corresponds to the variations between the nominal model and the predictions from the different composition models described in section 4.3.4. In addition, Fig. 5.1, low panel, illustrates the ratio between the measured data and the predictions from the nominal model. The ratio of the measured data to the nominal model is varies between 0.4 and 1.9, and its behavior indicates an energy dependence. Moreover, the presence of a local maximum inside the energy interval $\log(E_{\mathrm{rec}}/\mathrm{GeV}) = 4.0$ and $\log(E_{\mathrm{rec}}/\mathrm{GeV}) = 5.0$ appears where the nominal

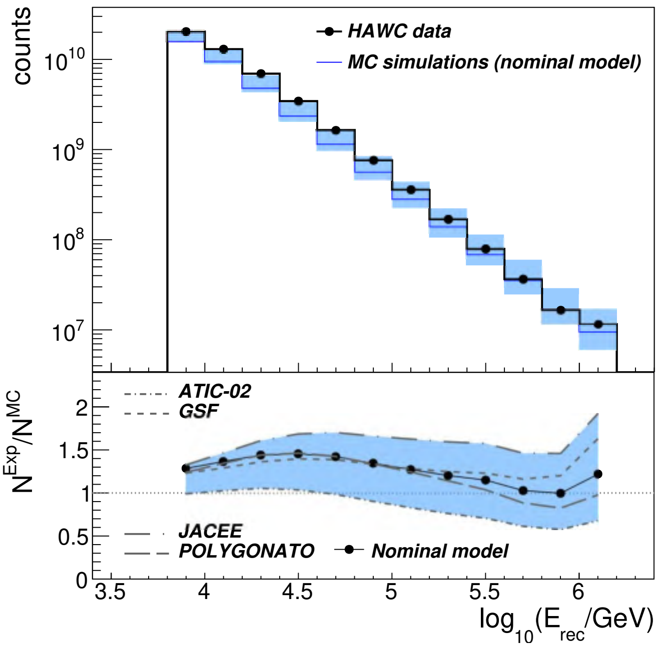

FIGURE 5.1: *First panel:* The (measured) reconstructed energy distribution from the (experimental dataset, c.f. section 4.5) nominal simulated data using the nominal composition model is presented as a (black circles with horizontal bold line) thin blue line, along with its corresponding error band in blue. The error band corresponds to minimum and maximum differences observed from the comparison between the reconstructed energy from the nominal model and those corresponding to the alternative cosmic ray composition models described in section 4.3.4. *Second panel:* Ratio curves of the HAWC data to the standard simulated distribution and the predictions from different composition models (c.f. section 4.3.4) [278]. The horizontal thin line in gray is a reference for 1:1 ratio. *Image Source:* [278].

cosmic ray composition model predicts a power-law spectrum (c.f. Fig. 4.7), suggesting that the experimental data deviates from this scenario. This discrepancy could be related to the presence of a variation in the spectral index in the all-particle spectrum at some tens of TeV, which has been published by the HAWC collaboration [22], as well as by the NUCLEON collaboration [23], and more recently in the updated analysis of the total energy spectrum measured with HAWC presented in [278], which is the core basis of the present thesis. The raw energy spectrum is presented in Fig. 5.2.

To reduce the bias in the reconstruction of the spectrum as possible we must account for the effects of the detector and the reconstruction method of the shower events. One way to achieve this is through the implementation of a deconvolution method.

5.2 Bayesian unfolding method

The design of measuring instruments (detectors) responds to the particular needs of specific studies or is limited by the technological developments available at the time.

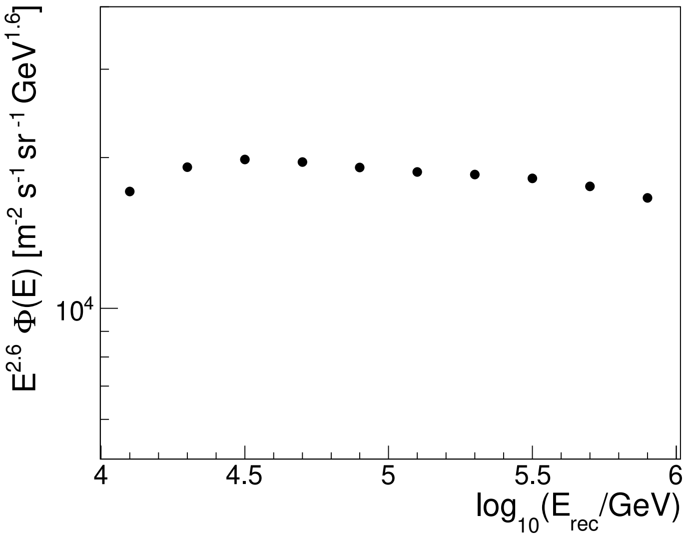

FIGURE 5.2: Raw spectrum reconstructed from the selected data of HAWC according to Eq. (5.1).

As a consequence, these constraints lead to limitations in the measurement range, resolution, and the detector's response, which to some degree distort the experimental measurements. Therefore, it is crucial to correct the measured distributions for resolution of the detector, which is often a challenging task [347].

In the context of the analysis presented in here, the precise measurement of the all-particle spectrum with HAWC relies on retrieving the best estimate for the true distribution, N, from the measured one, N_{rec}. To take into account the response of the detector a response matrix, R, was built using the nominal MC simulations. These quantities are related by means of the following equation:

$$N_{\text{rec}} = RN. \tag{5.2}$$

The simplest solution to Eq. (5.2) is by inversion, i.e.,

$$N = R^{-1}N_{\text{rec}}. \tag{5.3}$$

However, this solution will be subject to large statistical oscillations. A better solution to Eq. (5.2) can be found by the implementation of an unfolding method, which can be categorized into iterative and non-iterative algorithms [347].

In particular, the Bayesian unfolding method is a popular technique based on the Bayes' theorem [50–52]. The method estimates iteratively a smearing matrix $P(E|E_{\text{rec,j}})$ that corrects the raw energy distribution, and the result from this iterative process is the $N(E)$ distribution, which is an approximation to the true energy distribution. The formula to compute $N(E)$ is:

$$N(E_i) = \sum_{\text{j}=1}^{n_r} P(E_i|E_{\text{rec,j}})N(E_{\text{rec,j}}). \tag{5.4}$$

Here, the summation for j starts from 1 to n_r, with n_r representing the number of divisions (energy bins) within the reconstructed energy histogram for a given interval, while $i = 1, ..., n_t$, and n_t corresponds to the total number of energy bins of the unfolded distribution. The smearing matrix, $P(E_i|E_{\mathrm{rec,j}})$, represents the conditional probability that an event reconstructed with $E_{\mathrm{rec,j}}$ has been originated by an event with energy E_i.

$$P(E_i|E_{\mathrm{rec,j}}) = \frac{P(E_{\mathrm{rec,j}}|E_i)P(E_i)}{\sum_{l=1}^{n_t} P(E_{\mathrm{rec,j}}|E_l)P(E_l)}, \tag{5.5}$$

where $P(E_i)$ is the is the prior distribution of the causes E_i from the previous iteration. This prior knowledge is updated iteratively during the unfolding process. The response matrix, $P(E_{\mathrm{rec,j}}|E_i)$, describes the probability for an event with energy E_i to be reconstructed as an event with energy $E_{\mathrm{rec,j}}$.

In this framework, the response matrix has its own normalization condition [50]:

- $\sum_{\mathrm{j}=1}^{n_r} P(E_{\mathrm{rec,j}}|E_i) = 1.$

This condition states that a given event with energy E_i has an associated set of possible reconstructed energies E_{rec}.
In addition, the smearing matrix is subject to the following condition [50]

- $\sum_{i=1}^{n_t} P(E_i|E_{\mathrm{rec,j}}) = 1.$

This condition expresses that for a given event with reconstructed energy E_{rec} it must have originated from some event with energy E_i from the set of possible causes.

The Bayesian unfolding method treats the energy migration effects caused by the response of the detector, therefore correcting the measured energy distribution. The described method is a basic formalism that can be extend to include efficiency effects [50].

In the Bayesian unfolding, it is best to avoid using the unregularized result from a previous iteration as the prior distribution for the next iteration. Doing so can introduce large oscillations into the unfolded result and may differ from a physical solution [50]. While the initial prior might be a simple flat distribution or even a *granular* distribution, it is ideal to regularize the prior distribution for the intermediate unfolding steps to ensure a smooth and stable result [50]. In particular, for the present analysis, the true energy distribution $N(E)$, from the nominal model (see section 4.3.4) was selected as the prior information for the unfolding procedure. Only the intermediate unfolded results were smoothed with the 353HQtwice algorithm [348], as implemented in the ROOT analysis software [349].

A criterion to determine the iteration depth is required because of the iterative nature of the method. For the present analysis, the convergence of the method was assumed when a local minimum in the χ^2-distribution values was reached, and this point was used as the stopping criterion for the analysis. In addition, it was observed that the minimum in χ^2 is located within one iteration step of the local minimum observed in the *Weighted Mean Squared Error* (*WMSE*) [111, 350].

The χ^2 value is derived by a comparison of the raw distribution, $N(E_{rec,j})$, and the forward-folded distribution, $N^f(E_{rec,j})$. This relation is described by the formula

$$\chi^2 = \sum_{j=j_{min}}^{j_{max}} \frac{\left[N(E_{rec,j}) - N^f(E_{rec,j})\right]^2}{N(E_{rec,j})}. \tag{5.6}$$

For the minimization of the χ^2, the analysis focuses on the energy interval $4.0 \leq \log_{10}(E_{\mathrm{rec}}/\mathrm{GeV}) \leq 6.0$. Within this interval, j_{min} corresponds to the bin at the lower limit, i.e., $\log_{10}(E_{\mathrm{rec}}/\mathrm{GeV}) = 4.0$, while j_{max} is the label for the upper limit, in this case $\log_{10}(E_{\rm rec}/\mathrm{GeV}) = 6.0$. Also, the unfolded results will be presented in this energy interval. Here, $N^f(E_{rec,j})$ was obtained from $N(E_j)$ at a given iteration depth as follows

$$N^f(E_{rec,j}) = \sum_{i=1}^{n_t} P(E_{rec,j}|E_i)N(E_i). \tag{5.7}$$

The $WMSE$ is the mean squared sum of the systematic bias introduced by the unfolding combined with the statistical uncertainties [111, 350], and is given by

$$WMSE = \frac{1}{s}\sum_{i=1}^{s}\left[\frac{\bar{\sigma}^2_{stat,i}}{N(E_i)} + \frac{\bar{\sigma}^2_{bias,i}}{N^{MC}_{true}(E_i)}\right], \tag{5.8}$$

where s is the number of energy bins within $4.0 \leq \log_{10}(E_{\rm rec}/\mathrm{GeV}) \leq 6.0$. In addition, $\bar{\sigma}_{bias,i}$ ($\bar{\sigma}_{stat,i}$) represent the average systematic bias (statistical error), which was calculated as follows:

- **Statistical error:** To estimate the statistical error for each iteration depth, Poisson fluctuations were introduced into the experimental raw energy distribution, bin by bin, to create m toy spectra, which were then unfolded at the same iteration depth, and the results were averaged. The statistical error was then calculated as the deviation between the average and the individually unfolded spectra for each bin as follows

  $$\bar{\sigma}_{stat,i} = \sqrt{\sum_{j=1}^{m}\frac{[N_j^{Exp}(E_i) - \bar{N}^{Exp}(E_i)]^2}{m}}. \tag{5.9}$$

  Here, the average of the m toy spectra is $\bar{N}^{Exp}(E_i)$, while the j-th unfolded energy spectrum is represented by $N_j^{Exp}(E_i)$.

- **Systematic bias:** In the nominal MC simulations, the full data of the energy spectrum (using the nominal model) is available. For this reason, the MC simulations were employed in the evaluation of the systematic bias. First, the total energy spectrum from the nominal model was weighted to reproduce the shape of the one observed in [22], and was employed as the reference. Next, Poisson-like fluctuations were added, bin by bin, to the MC reconstructed energy distribution (c.f. Fig. 5.1, to generate a total of m fake measured spectra, $N_j^{MC}(E_{\rm rec})$, and after each of these fake spectra were unfolded one by one. Then, for a given iteration depth, the corresponding value of the systematic bias is computed from the comparison between the averaged unfolded results and the true energy spectrum, $N(E^T)$. The bias can be computed with the following formula:

  $$\bar{\sigma}_{bias,i} = \sum_{j=1}^{m}\frac{N_j^{MC}(E_i)}{m} - N^{MC}_{true}(E_i). \tag{5.10}$$

5.2.1 Statistical uncertainties from the finite size of the selected measured data set

According to the procedures described in [22, 351], to determinate the covariance matrix V_{stat}^{data}, which contains the statistical error from the measured data sample, the statistical errors from $N(E_{rec})$ were propagated through the unfolding procedure

$$V_{stat}^{data}[N_\mu^i, N_\nu^i] = \sum_{j,k} \frac{\partial N_\mu^i}{\partial N_{rec,j}} \mathrm{Cov}[N_{rec,j}, N_{rec,k}] \frac{\partial N_\nu^i}{\partial N_{rec,k}}, \tag{5.11}$$

In here,

$$\begin{aligned} N_\mu &= N(E_\mu), \\ N_{rec,j} &= N(E_{rec,j}), \\ M_{\mu j} &= P(E_\mu | E_{rec,j}), \end{aligned}$$

and

$$\frac{\partial N_\mu^i}{\partial N_{rec,j}} = M_{\mu j} + \frac{N_\mu^i}{N_\mu^{i-1}} \frac{\partial N_\mu^{i-1}}{\partial N_{rec,j}} - \sum_{\sigma,k} \frac{N_{rec,k}}{N_\sigma^{i-1}} M_{\mu k} M_{\sigma k} \frac{\partial N_\sigma^{i-1}}{\partial N_{rec,j}}.$$

Moreover, the i index corresponds to the iteration depth related to the unfolded $N(E)$, and the covariance matrix associated with the reconstructed energy bins of the $N(E_{rec})$ distribution is represented by $\mathrm{Cov}[N_{rec,j}, N_{rec,k}]$.

Assuming that reconstructed energy bins are independent and Poisson-distributed

$$\mathrm{Cov}[N_{rec,j}, N_{rec,k}] = N_{rec,j}\delta_{j,k}. \tag{5.12}$$

In particular, when $i = 0$

$$\partial N_\mu^0 / \partial N_{rec,j} = 0. \tag{5.13}$$

5.2.2 Statistical uncertainties from the limited size of the simulated data

Another important source of statistical error is introduced in the results by the finite number of simulated data (c.f. section 4.3.4) employed in the construction of the response matrix, which was also estimated via error propagation with the method from [22, 351].

For this case, the covariance matrix V_{stat}^{MC} is given by

$$V_{stat}^{MC}[N_\mu^i, N_\nu^i] = \sum_{\lambda,j} \sum_{\rho,k} \frac{\partial N_\mu^i}{\partial P_{j\lambda}} \mathrm{Cov}[P_{j\lambda}, P_{k\rho}] \frac{\partial N_\nu^i}{\partial P_{k\rho}}, \tag{5.14}$$

where

$$P_{j\mu} = P(E_{rec,j} | E_\mu),$$

and

$$\frac{\partial N_\mu^i}{P_{j\lambda}} = [N_\mu^{i-1}\delta_{\mu\lambda} - M_{\mu j} N_\lambda^{i-1}] \frac{N_{rec,j}}{\sum_\sigma P_{j\sigma} N_\sigma^{i-1}} + \frac{N_\mu^i}{N_\mu^{i-1}} \frac{\partial N_\mu^{i-1}}{\partial P_{j\lambda}} - \sum_{\sigma,k} \left[\frac{N_{rec,k}}{N_\sigma^{i-1}} M_{\mu k} M_{\sigma k} \frac{\partial N_\sigma^{i-1}}{\partial P_{j\lambda}} \right].$$

The covariance matrix $\mathrm{Cov}[P_{j\lambda}, P_{k\rho}]$ from Eq. (5.14) is defined as

$$\mathrm{Cov}[P_{j\lambda}, P_{k\rho}] = \begin{cases} P_{j\lambda}[1 - P_{k\lambda}]/\tilde{N}_{MC,\lambda} & ; j = k, \lambda = \rho \\ -P_{j\lambda}P_{k\lambda}/\tilde{N}_{MC,\lambda} & ; j \neq k, \lambda = \rho \\ 0 & ; \text{other case,} \end{cases} \tag{5.15}$$

where $\tilde{N}_{MC,\lambda}$ represents the equivalent number of unweighted simulated showers contained within the bin of energy E_λ.

$$\tilde{N}_{MC,\lambda} = \frac{(\sum_{k=1} w_{k\lambda})^2}{\sum_{k=1} w_{k\lambda}^2}. \tag{5.16}$$

where $w_{k\lambda}$ is the weight of the k-th event.

5.3 Total energy spectrum of cosmic rays

Using the Bayes unfolding, the true energy spectrum, $N(E)$, is estimated from the reconstructed distribution $N(E_{\mathrm{rec}})$. Following this procedure, the total energy spectrum is calculated with $N(E)$ according to the following formula:

$$\Phi(E) = \frac{N(E)}{\Delta E\, \Delta t\, A_{\mathrm{eff}}\, \Delta\Omega}. \tag{5.17}$$

Here, ΔE represents the width of of each true energy bin, and Δt is the effective observational time of the data, $\Delta\Omega$ is the solid angle of observation, A_{eff} represents the effective area, which is proportional to the efficiency, ϵ, of a cosmic ray being detected, reconstructed, and passed the established quality parameters (c.f. section 4.3.6). In HAWC, the corresponding effective area is computed with the following equation: [22]

$$A_{\mathrm{eff}}(E) = A_{\mathrm{thrown}}\epsilon(E). \tag{5.18}$$

In the above expression, A_{thrown} is the simulated throwing area. This represents a circular region over which the MC events were generated and thrown. It is defined as $A_{\mathrm{thrown}} = (1/2)(\cos\theta_{max} + \cos\theta_{min})\pi R_{thrown}^2$, with a radius $R_{thrown} = 1$ km. In particular, for the present analysis, θ_{min}, and θ_{max}, are equal to 0° and 35°, respectively (see section 4.3.6).

For the present analysis, the effective area was estimated for the all-particles scenario from the nominal model (described in section 4.3.4). The result is plotted in Fig. 5.3, left panel, as a function of the true primary energy. From this figure, it is possible to identify the maximum efficiency region for the present study. In addition, the efficiency (see Eq. (5.18)) is plotted against the base ten logarithm of the true primary energy in Fig. 5.3, right panel. While the efficiency decreases and tends to zero at 10 TeV, it becomes constant within $4.5 \leq \log_{10}(E/\mathrm{GeV}) \leq 6.0$, where it has its maximum value. For comparison, the effective areas calculated for each individual mass group (H, He, C+O, Ne+Mg+Si, and Fe) are also presented in Fig. 5.3. The corresponding effective area of the H (Fe) component is almost constant above $\log_{10}(E/\mathrm{GeV}) = 4.0$ (4.5), and below this point it rapidly tends to zero close to $\log_{10}(E/\mathrm{GeV}) = 3.1$ (3.9). Since the efficiency for Fe-induced events is almost zero at $E = 8$ TeV, it was decided to present unfolded energy spectrum only for energies $4.0 \leq \log_{10}(E/\mathrm{GeV}) \leq 6.0$.

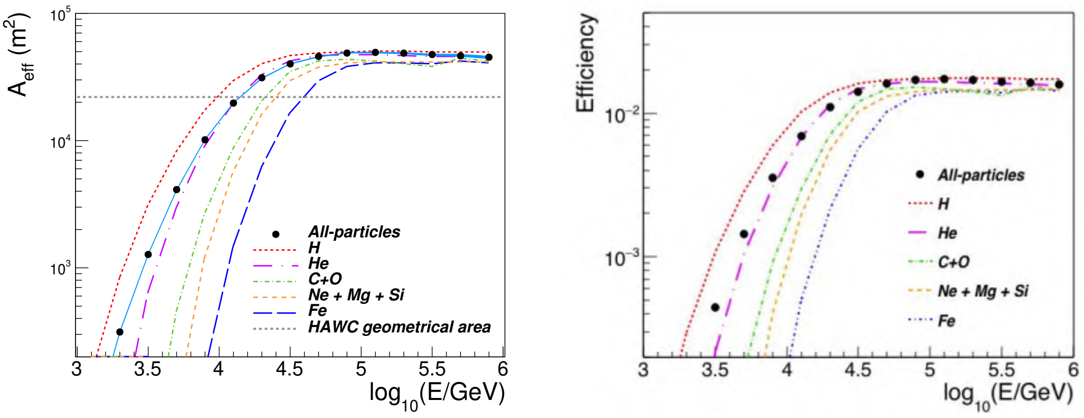

FIGURE 5.3: The effective area (left panel) and efficiency (right panel) of HAWC for the detection of cosmic-ray events versus the base ten logarithm of the true primary energy. Statistical errors are shown with the blue band. A_{eff} is compared with the geometric area of HAWC (horizontal dashed line). The individual contributions to the total effective area and efficiency from the mass groups of H (dashed lines in red), He (loosely dashdotted lines in violet), C+O (densely dashdotted lines in green), Ne+Mg+Si (densely dashed lines in orange), and Fe (long dash lines in blue) are shown. The curves were obtained with QGSJET-II-04 simulations and the nominal composition model for a mixed component scenario. *Image Source:* [278].

5.4 Test of the reconstruction method with MC simulations

In the present work, some tests were designed using simulated data to

- validate the reconstruction method,
- test the reconstruction method with an energy spectrum with an artificial spectral break in the TeV region, as in [22].

To validate the accuracy of the reconstruction, we applied the reconstruction method to the nominal simulated data set (see section 4.3.4). The MC raw distribution $N^{MC}(E^{rec})$ estimated from the nominal MC data sets is shown at the top panel of Fig. 5.1.

The simulated raw distribution was processed using the nominal reconstruction procedure using the Bayesian unfolding method. The method converged at 5 iterations, as determined by the χ^2 criteria. The unfolded MC energy spectrum is presented at Fig. 5.5, left panel, where the true energy spectrum from the simulations is displayed for reference. The spectra exhibit good agreement, with a maximum relative difference of approximately 2%, as shown in the first panel of Fig. 5.5. Here, the relative error was calculated as $(\Phi^{rec} - \Phi^{true})/\Phi^{true}$. In addition, the unfolded MC spectrum, subject to a smoothing procedure based on a fit with a power-law model formula, as described in [22], is also plotted for comparison at the left panel of Fig. 5.5. Such result is also in agreement with the true MC spectrum (see Fig. 5.5, right panel).

The second test with MC simulations was carried out to demonstrate the capability of the unfolding procedure to reconstruct a spectral softening similar to that observed in [22]. To start with, a toy MC model was created by introducing an artificial break, $\Delta\gamma = 0.22$, into the spectrum of the nominal MC simulations at $E = 10^{4.4}$

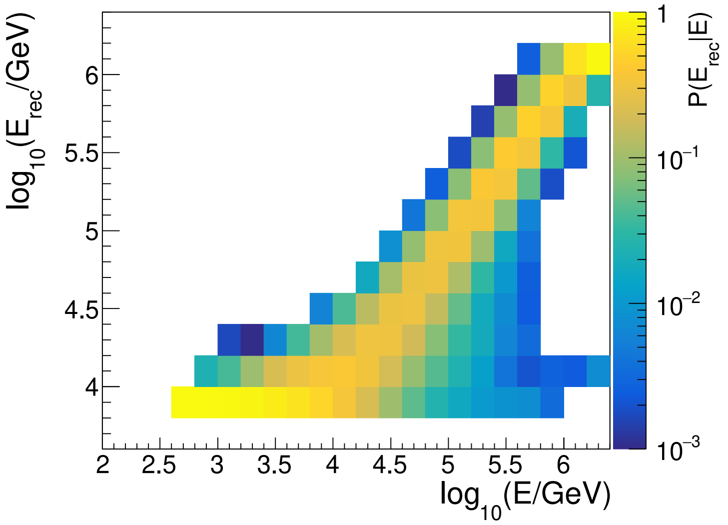

FIGURE 5.4: The response matrix, $P(E_{rec}|E)$, used in the Bayesian unfolding method to account for migration effects between neighboring energy bins. It was estimated with the nominal QGSJET-II-04 simulations (see section 4.3.4).
Image Source: [278].

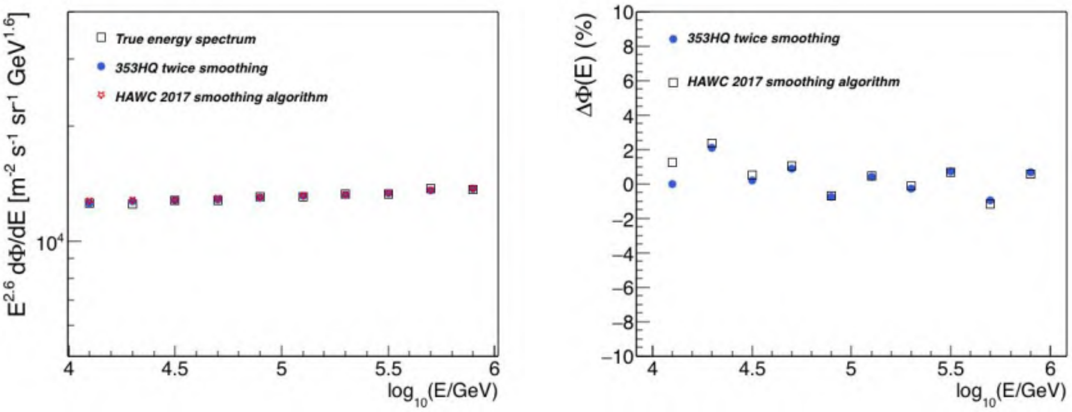

FIGURE 5.5: *Left panel*: The unfolded energy spectrum for a toy MC model based on the nominal model described in section 4.3.4 (blue circles), and the unfolded result following the method described in [22] with a power law smoothing (open stars in red) are compared to the true energy spectrum from the MC simulations (open squares). The magnitude of the statistical errors is plotted as vertical error bars. *Right panel*: The differences between both reconstruction techniques are represented by the ratios of the unfolded spectra to the true energy spectrum. The results for the present reconstruction technique (c.f. section 5.2) are represented by the blue circles, while the results obtained with the procedure and smoothing algorithm from [22] are shown as open squares.

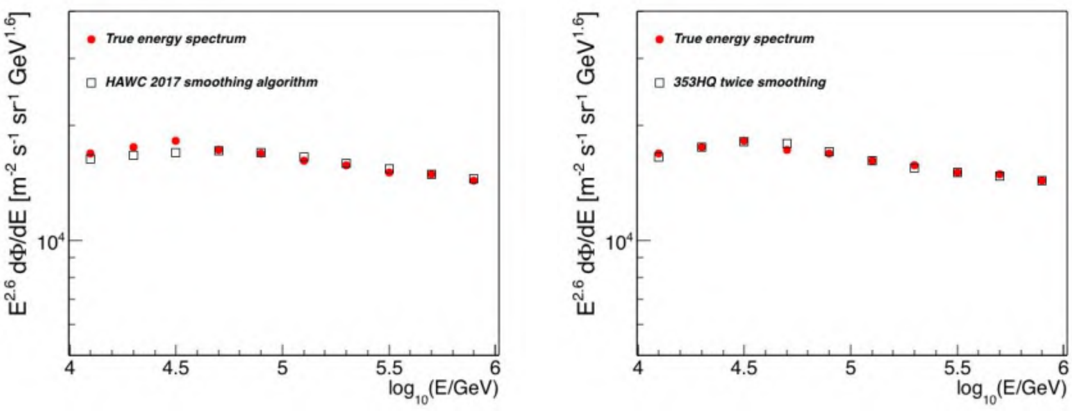

FIGURE 5.6: The true energy spectrum (circles) for the toy MC simulations with an artificial break at $E = 10^{4.4}$ GeV compared to the unfolded spectra (squares) obtained by using the smoothing method of [22] (left panel) and by the 353HQtwice smoothing algorithm [348] (right panel), respectively.

GeV. The unfolding method, as described in here (c.f. section 5.2), was used on the raw energy distribution of the toy MC model. The corresponding unfolded spectrum is plotted in Fig. 5.6, right panel, along with the corresponding true spectrum derived from the toy MC model. The all-particle spectrum of the toy model was also reconstructed with the procedure presented in [22] (see Fig. 5.6, left panel) for a comparison of both methods. Fig. 5.7 shows the relative difference between the unfolded spectra and the true spectrum of the toy MC model. An analysis of this figure demonstrates that the unfolding procedure employed in this work provides an improved reconstruction accuracy compared to the method presented in [22], for a scenario involving a shift spectral index. The same figure shows that the power-law smoothing method tends to flatten the energy spectrum and to shift the feature to higher energies compared to the original position in the true spectrum. Because of this effect, it was adopted the smoothing method of section 5.2 for the present work.

The aforementioned MC example served to demonstrate the performance of the reconstruction procedure, particularly in a scenario with a spectral cut. Furthermore, in [278], a third test was conducted to verify whether a reliable reconstruction of the spectral indices on either sides of the spectral cutoff using the method presented here. The first step was to create a simulated toy model using the predictions from QGSJET-II-04, designed to replicate the mass composition of the nominal model (see Fig. 4.7). In addition, the MC toy model was weighted to exhibit a broken power-law behavior, as defined by Eq. (4.6), in the total energy spectrum like the one that we observed in the experiment with the reconstruction of the present work. The true spectrum of the toy model is plotted in Fig. 5.8. The parameters that characterize it are from Eq. (4.6):

- $\log_{10}[\Phi_0/(\mathrm{m}^{-2}\,\mathrm{s}^{-1}\,\mathrm{sr}^{-1}\,\mathrm{GeV}^{-1})] = 4.24$,
- $\gamma_1 = -2.53$,
- $\gamma_2 = -2.71$,
- $E_{\text{break}} = 37.7$ TeV,

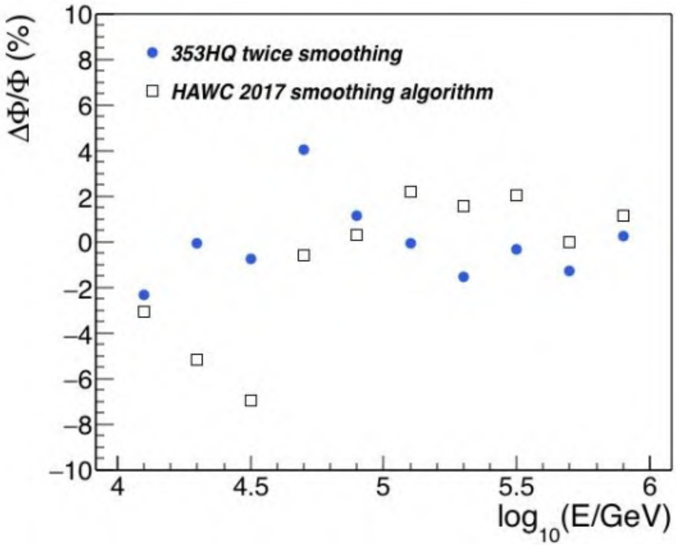

FIGURE 5.7: Relative ratios of the unfolded spectra, derived from two different smoothing methods, to the a toy MC model (c.f. Fig. 5.6). The unfolded results by using the 353HQtwice smoothing algorithm and smoothing method described in [22] are represented by blue circles and open black squares, respectively.

where the value of E_{break} was chosen from fitting the relative energy distribution of the measured data to the nominal simulated data (see Fig. 5.2, bottom panel) in the energy interval $4.0 \leq \log_{10}(E_{rec}/\text{GeV}) \leq 6.0$, under a broken power-law model (Eq. (4.6)).

Fig. 5.8 presents the unfolded spectrum derived from the toy MC model, obtained by treating the corresponding energy distribution, E_{rec}, with the present unfolding method. The unfolded result is shown with its corresponding total statistical errors (c.f. sections 5.2.2 and 5.2.1) and systematic uncertainties (c.f section 6.2). From this figure it is clear to see that the reconstructed spectrum reveals the spectral softening induced in the toy MC model and is in good agreement with the corresponding true spectrum. In addition, a comparison of the best-fit parameters obtained in both cases was conducted to verify the accuracy of the method. Thus, the reconstructed result spectrum derived from the unfolding of the toy model energy distribution was also fitted with the broken power-law function from Eq. (4.6). The best fit parameters are presented below:

- $\log_{10}[\Phi_0/(\text{m}^{-2}\,\text{s}^{-1}\,\text{sr}^{-1}\,\text{GeV}^{-1})] = 4.24 \pm 0.002(\text{stat.})^{+0.03}_{-0.02}(\text{sys.})$,
- $\gamma_1 = -2.53 \pm 0.001(\text{stat.}) \pm 0.03(\text{sys.})$,
- $\gamma_2 = -2.71 \pm 0.002(\text{stat.})^{+0.02}_{-0.04}(\text{sys.})$,
- $E_{\text{break}} = [38.9 \pm 0.1(\text{stat.})^{+6.8}_{-1.7}(\text{sys.})]$ TeV,

which were compared with those values obtained for the true spectrum.

We observed a that the true and reconstructed parameters are consistent within uncertainties. The largest difference is found for the position of the break, however, it is just of the order of 3.1% The fit to the unfolded toy spectrum is plotted in Fig. 5.8.

The comparison demonstrates the good agreement between the fitted result and the true energy spectrum.

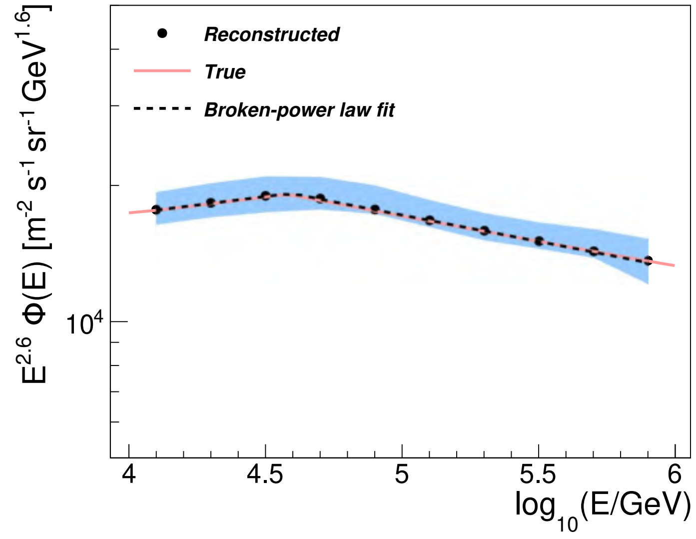

FIGURE 5.8: The true (orange thin line) and the unfolded (black circles) spectra for a toy model generated from the MC nominal simulations (see section 4.3.4) are compared. The true MC spectrum exhibit a break, which was reconstructed using the analysis presented in this doctoral thesis. In particular, the reconstructed energy spectrum of cosmic rays was obtained following the present reconstruction procedure, and is plotted with its total statistical error (vertical bars) and systematic uncertainties (blue error band). The fit to the reconstructed result with Eq. (4.6) is shown with a dashed line. *Image Source:* [278].

Overall, the above examples demonstrate that the unfolding method from section 5.2 is a suitable selection for the detailed analysis of the all-particle energy spectrum and its cut-off with HAWC, and it complements other analyses previously made by the collaboration that also tested the veracity of this method [22, 124, 278]. Moreover, other unfolding methods were implemented to cross-check the reconstruction of the spectrum, like the reduced cross-entropy method [352] and the Gold unfolding technique [293]. Both models are described in Appendix A.

Chapter 6

All-particle cosmic-ray energy spectrum from HAWC data

Following the procedure described in Chapter 5, the Bayesian method was used and implemented over the reconstructed primary energy histogram extracted from the data sample, as detailed in section 4.5, with the goal to obtain the unfolded spectrum from HAWC measurements within the primary energy interval 10 TeV $\leq E \leq$ 1 PeV [278].

The unfolding of the total spectrum is detailed in this chapter. In addition, the systematic uncertainties that have an effect in the reconstruction of the energy spectrum are described individually [353]. The unfolded result has been published in [278].

6.1 Reconstruction of the total spectrum

After applying the selection cuts from section 4.3.6 to the selected HAWC data sample (c.f. section 4.5), the measured energy distribution, $N(E_{\mathrm{rec}})$, is obtained within the energy interval $2.0 \leq \log_{10}(E_{\mathrm{rec}}/\mathrm{GeV}) \leq 6.4$. Here, we used a bin size of $\Delta \log_{10}(E_{\mathrm{rec}}/\mathrm{GeV}) = 0.2$. Though the Bayesian unfolding should minimize the correlations between neighboring bins, it was shown in [278] that the selection of a smaller bin size for the energy distribution increases the bin-to-bin correlations. In particular, for energies between $\log_{10}(E_{\mathrm{rec}}/\mathrm{GeV}) = 4.0$ and $\log_{10}(E_{\mathrm{rec}}/\mathrm{GeV}) = 4.5$, where correlation values from 0.3 (0.8) to 0.6 (1.0) between adjacent bins were found for bin widths of $\Delta \log_{10}(E/\mathrm{GeV}) = 0.2$ ($\Delta \log_{10}(E/\mathrm{GeV}) \leq 0.16$). The measured distribution is plotted in the top panel of Fig. 5.1, where it is compared against the reconstructed energy histogram from the simulated data using the nominal composition model.

Then, the raw distribution from the HAWC measured data set is corrected for detector effects by means of the Bayesian unfolding method (c.f. section 5.2) using the response matrix derived from MC simulations for the all-particle component of the nominal composition model (see Fig. 5.4). This step yields the unfolded distribution, employed for the energy spectrum reconstruction. The stopping criterion of the unfolding method was determined as described in section 5.2. For energies between 10 TeV and 1 PeV, the χ^2 reaches a local minimum at 8 iterations (see the plot at Fig. 6.1, second panel) while the local minimum for the $WMSE$ is located between 8 and 10 iterations (see Fig. 6.1, left panel). Thus, the iteration depth of the unfolding procedure was set to 8 iterations. Inside the same energy interval, the absolute magnitude of the differences between $N(E_{rec,j})$ and $N^f(E_{rec,j})$ were found to be smaller than 4.3%. As described in section 5.2, the χ^2 guarantees that the result is at the point were the differences between $N(E_{rec,j})$ and $N^f(E_{rec,j})$ are minimum, while the

$WMSE$ method confirms that the result is within the region where the total error in the reconstruction is minimum. In addition, it was observed that the shape of the spectrum is not modified by the variations in the iteration depth, and the relative differences with the reference result (unfolded with 8 iterations) are smaller than 1% in the energy interval $4.0 \leq \log_{10}(E_{rec}/\text{GeV}) \leq 6.0$. This is true for iterations no bigger than 40. Therefore, it is observed that the result obtained with 8 iterations is a stable solution.

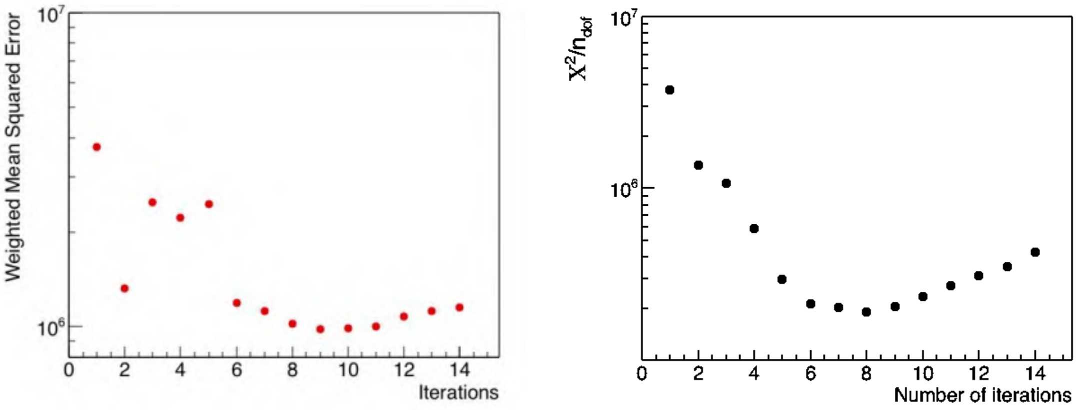

FIGURE 6.1: The $WMSE$ (left panel) and χ^2/n_{dof} (right panel) are plotted as a function of the iteration depth. Both tests were performed to estimate the optimal number of iterations for the Bayesian unfolding method applied to the HAWC data. Local minima are observed around 9 iterations and at 8 iterations, respectively.

As a final step, using the unfolded energy distribution, the all-particle cosmic ray energy spectrum was estimated with Eq. (5.17), where the effective area was calculated from the QGSJET-II-04 simulations for the all-particles scenario of the nominal model (see Fig. 5.3). The unfolded spectrum is presented in Fig. 6.2. Here, the all-particle differential flux of cosmic rays is plotted with vertical error bars that correspond to the total statistical error, which was estimated as the sum in quadrature of the statistical uncertainties intrinsic to the finite size of the measured and simulated data sets, respectively (c.f. sections 5.2.1 and 5.2.2). The statistical error varies within ±2.6% in the interval from 10 TeV and 1 PeV. In particular, the uncertainties related to the size of the measured data vary between ±0.001% and ±0.03%, while the corresponding uncertainties associated to the MC simulations varies from ±0.05% to ±2.6%. Moreover, the total systematic uncertainties are represented by the blue error band, and vary between −11.7% and +13.6% in the above energy interval. The energy spectrum points are presented in table 6.1, where their corresponding statistical and systematic uncertainties are presented.

The procedure to estimate the systematic uncertainties from different sources that affect the reconstruction of the energy spectrum, as well as a description of the different error sources under consideration in the present work, are described in the following section.

6.2 Systematic errors in the energy spectrum reconstruction

Some systematic errors from different sources can produce variations in the unfolded spectrum, thus creating a bias. In this work, the uncertainties related to a

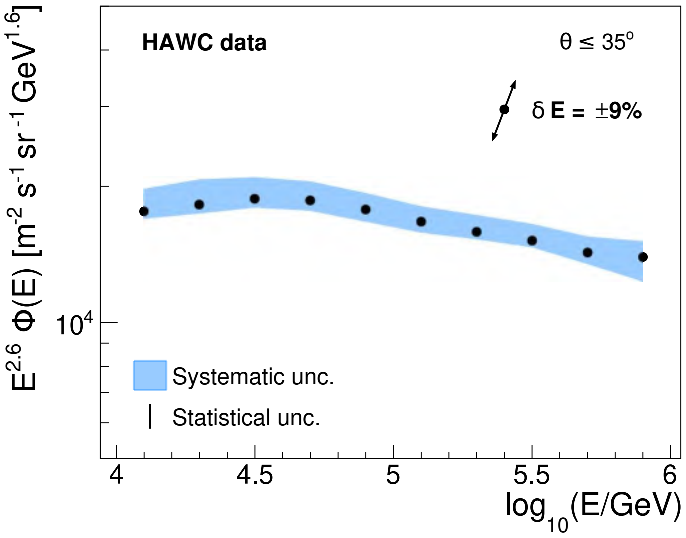

FIGURE 6.2: The all-particle cosmic-ray energy spectrum measured with HAWC (circles), after unfolding a data sample from 5.3 years of effective observation. To appreciate in detail the shift of the spectral index, the reference result was multiplied by an energy factor of $E^{2.6}$. The systematic uncertainties are shown as an error band, and the corresponding statistical uncertainties as vertical error bars. The marker size exceeds the length of the error bars. The arrows' size represent the variation in the spectrum due to a $\delta E = \pm 9\%$ systematic uncertainties related to the energy scale.
Image Source: [278].

given systematic source were evaluated by generating different sets of MC simulations, designed to represent different possible scenarios for the systematic error source under consideration. These simulations involved changes to the model, the analysis process, or the values of the parameters contributing to the uncertainty. Then, the energy spectrum is reconstructed from the experimental data using each MC data set associated with the systematic error source. To calculate the corresponding bias, the results are compared to the unfolded energy spectrum from Fig. 6.2, and the differences are listed as maximum or minimum variations. This process is replicated for every systematic source under study, and the corresponding minimum and maximum variations are combined in quadratically to account for the total systematic bias. Fig. 6.3 shows the total statistical and systematic uncertainties against the base ten logarithm of the primary energy.

The systematic uncertainties under study include

- the PMT performance (efficiency, charge resolution, late-light effect, and energy threshold) [49],
- variations due to seasonal effects,
- unfolding uncertainties including the choice of the algorithm, prior, and smoothing technique,
- the effective area,

TABLE 6.1: Flux points of the reference result presented in this thesis [278]. For a bin with limits E_{min} and E_{max}, and centered at E, the corresponding data point is presented with statistical $\sigma_{\text{stat.}}$ and systematic $\sigma_{\text{sys.}}$ uncertainties. *Table Source:* [278].

E (10^3 GeV)	E_{min} (10^3 GeV)	E_{max} (10^3 GeV)	$\Phi \pm\sigma_{\text{stat.}} + \sigma_{\text{sys.}} - \sigma_{\text{sys.}}$ (GeV^{-1} m^{-2} s^{-1} sr^{-1})
12.59	10.00	15.85	$(3.85 \pm 0.01 + 0.47 - 0.14) \times 10^{-7}$
19.95	15.85	25.12	$(1.20 \pm 0.01 + 0.16 - 0.05) \times 10^{-7}$
31.62	25.12	39.81	$(3.75 \pm 0.02 + 0.43 - 0.16) \times 10^{-8}$
50.12	39.81	63.10	$(1.12 \pm 0.01 + 0.11 - 0.06) \times 10^{-8}$
79.43	63.10	100.00	$(3.23 \pm 0.03 + 0.28 - 0.19) \times 10^{-9}$
125.89	100.00	158.49	$(9.18 \pm 0.10 + 0.74 - 0.50) \times 10^{-10}$
199.53	158.49	251.19	$(2.63 \pm 0.04 + 0.23 - 0.10) \times 10^{-10}$
316.29	251.19	398.11	$(7.60 \pm 0.14 + 0.67 - 0.25) \times 10^{-11}$
501.19	398.11	630.96	$(2.16 \pm 0.05 + 0.18 - 0.12) \times 10^{-11}$
794.33	630.96	1000.00	$(6.38 \pm 0.17 + 0.53 - 0.75) \times 10^{-12}$

- variations between the results for vertical and inclined events,
- uncertainties relative to the cosmic-ray composition models,
- and errors associated with the high-energy hadronic interaction model.

The total systematic bias is composed from the individual contributions related to each of the different uncertainty sources listed above are shown in Fig. 6.4. In addition, the systematic analysis performed in this work showed that, in the range $4.1 \leq \log_{10}(E/\text{GeV}) \leq 5.9$, the main systematic uncertainties in the HAWC spectrum arise from PMT modeling, the choice of the modeling of the relative abundances of cosmic rays in the analysis, and the aging effects over the PMTs' efficiencies at different DAQ periods (see table 6.2).

TABLE 6.2: Minimum and maximum variations of the dominant systematic uncertainty sources.

Source	minimum (%)	maximum (%)
PMT efficiency	−7.6%	+6.5%
Composition model	−1.1%	+11.6%
PMT late light	−3.4%	+5.6%

The following subsections will describe the systematic error sources and their individual contributions to the total systematic bias.

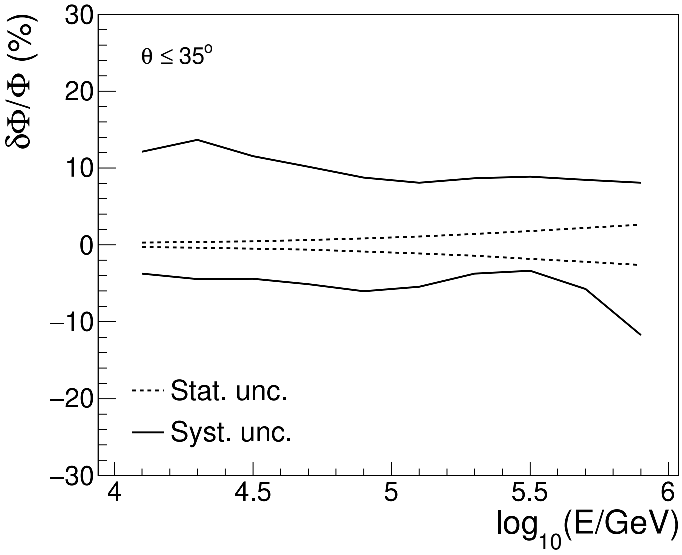

FIGURE 6.3: The continuous line corresponds to the total relative systematic error on the unfolded spectrum, while the dashed line represents the corresponding relative statistical uncertainty. *Image Source:* [278].

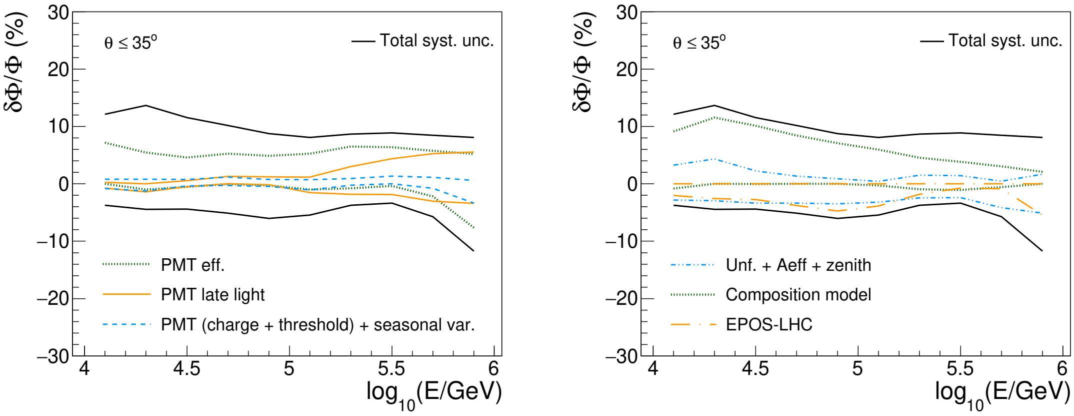

FIGURE 6.4: *Left panel:* The individual components of the total relative systematic error (bold line) from the PMT efficiency (dotted line in green), PMT late-light (solid line in orange), in addition to the contribution from the differences in the spectrum due to the seasons of the year plus the contributions from the PMT charge and threshold uncertainties combined (dashed line in azure), are presented as a function of $\log_{10}(E/\mathrm{GeV})$. *Right panel:* Same but for the contributions from the sum quadrature of the unfolding method, the seed for the Bayes unfolding, A_{eff} and the zenith angle (dash-dot-dot line in azure), the uncertainties in the relative abundances of the elemental mass groups of cosmic rays (dotted line in green), and the choice of the simulation package for high-energy hadronic interactions (long-dash dotted line in orange) are plotted against the base ten logarithm of the primary energy. To make a clear comparison between the different contributions, those with magnitudes smaller or equal to 5% were combined using a quadrature sum. *Image Source:* [278].

6.2.1 PMT systematic uncertainties

The uncertainties produced by the modeling and performance of the PMTs have been subject of study by the collaboration in other analysis like [22, 49, 124], and are related to four known effects: time dependence of the PMT efficiency (aging effects) and spatial configuration, energy threshold, charge resolution, and the late-light effect.

Variations in the PMT efficiency and configuration measured at different DAQ periods.

This systematic uncertainty source is related to change over time of the PMT efficiencies and the physical configuration of the active PMTs at the HAWC experimental facility. It was evaluated employing several MC data sets, each representing a specific DAQ period: September of 2015, April and July of 2016, February and June of 2017, and lastly February of 2018, and incorporating the corresponding active PMT layout and efficiency information to study potential spectral changes caused by PMT aging and variations in the number of operational PMTs through the DAQ periods. These aspects

These simulations were created upon the configuration of active PMTs and their efficiencies information from those periods, to study the variations in the spectrum due to possible PMT aging effects and changes in the number of active PMTs during the data-taking period, which are not in the nominal MC simulations.

The following MC simulations were employed to evaluate this systematic source:

```
 /data/archive/hawcroot/sim/reco/aerie_svn_42375a/
    config_hawc_v101/config_run004255

 /data/archive/hawcroot/sim/reco/aerie_svn_42375a/
    config_hawc_v101/config_run005214

 /data/archive/hawcroot/sim/reco/aerie_svn_42375a/
    config_hawc_v101/config_run005689

/data/archive/hawcroot/sim/reco/aerie_svn_42375a/
   config_hawc_v101/config_run006283

/data/archive/hawcroot/sim/reco/aerie_svn_42375a/
   config_hawc_v101/config_run006801

/data/archive/hawcroot/sim/reco/aerie_svn_42375a/
   config_hawc_v101/config_run007578
```

Fig. 6.5, top left panel, shows the HAWC energy spectra reconstructed with the above MC simulations. At $\log_{10}(E/\mathrm{GeV}) = 5.9$, the observed deviations from the reference energy spectrum were found between -7.6% and $+5.2\%$, while at an energy $\log_{10}(E/\mathrm{GeV}) = 4.1$, the variations are between 0.0% and $+7.1\%$. This represents one of the largest sources of systematic bias in the reference spectrum [278].

PMT late-light effect

The PMT late-light effect has a direct impact into the calibration of the effective charge, Q_{eff}, and results in an artificial increase of the EAS Q_{eff}, specially for $Q_{eff} >$

50 PE. This uncertainty is due to the disparity between the calibration laser pulses and EAS fronts time distributions [49]. To study this effect, modifications to the Q_{eff} were made through simulations by adding a linear function (calibrated with data) in logarithmic space in the interval $1.25 \leq \log_{10}(Q_{eff}/\mathrm{PE}) \leq 2.25$. At $\log_{10}(Q_{eff}/\mathrm{PE}) = 1.25$ ($\log_{10}(Q_{eff}/\mathrm{PE}) = 2.25$), this function takes the value of 0.0 (0.1). The value of the function at $\log_{10}(Q_{eff}/\mathrm{PE}) = 2.25$ is multiplied by a factor between 0.5 and 1.25 to compute the systematic bias from this source. The MC simulations used for this study are located in the directories

```
/data/archive/hawcroot/sim/reco/aerie_svn_42375a/
   config_hawc_v101/daqsim-config_broadpulse-0p50

/data/archive/hawcroot/sim/reco/aerie_svn_42375a/
   config_hawc_v101/daqsim-config_broadpulse-0p75

/data/archive/hawcroot/sim/reco/aerie_svn_42375a/
   config_hawc_v101/daqsim-config_broadpulse-1p25
```

The energy spectra derived from the aforementioned files were compared to the reference spectrum (see Fig. 6.5, bottom left panel). It was found that for energies $\log_{10}(E/\mathrm{GeV}) \leq 5$, the spectra are in good agreement and exhibit similar shapes. In the range $4.1 \leq \log_{10}(E/\mathrm{GeV}) \leq 5.9$, the observed deviations from the reference energy spectrum were found between -3.4% to $+5.6\%$.

PMT charge resolution

The uncertainty introduced by PMT charge resolution, as discussed in [49, 354], was determined by repeating the analysis with a charge resolution of $\log_{10}(Q_{eff}) = 0.0$ and 0.06 instead of the default value of 0.04. The corresponding MC simulation files are located at:

```
/data/archive/hawcroot/sim/reco/aerie_svn_42375a/
   config_hawc_v101/daqsim-config_charge-uncertainty-0p00

/data/archive/hawcroot/sim/reco/aerie_svn_42375a/
   config_hawc_v101/daqsim-config_charge-uncertainty-0p06
```

The reference spectrum is plotted in the top right panel of Fig. 6.5 against the generated spectra from the aforementioned MC simulations. This comparison reveals variations from -2.1% to $+1.0\%$ within $4.1 \leq \log_{10}(E/\mathrm{GeV}) \leq 5.9$.

PMT charge threshold

According to [49], the simulated PMT minimum charge detection limit is set to 0.2 PE, however, this value has an uncertainty equivalent to ±0.05 PE, which introduces an uncertainty in the spectrum. The MC simulations used for the analysis of this uncertainty source are stored in these directories

```
/data/archive/hawcroot/sim/reco/aerie_svn_42375a/
   config_hawc_v101/daqsim-config_threshold-0p15
```

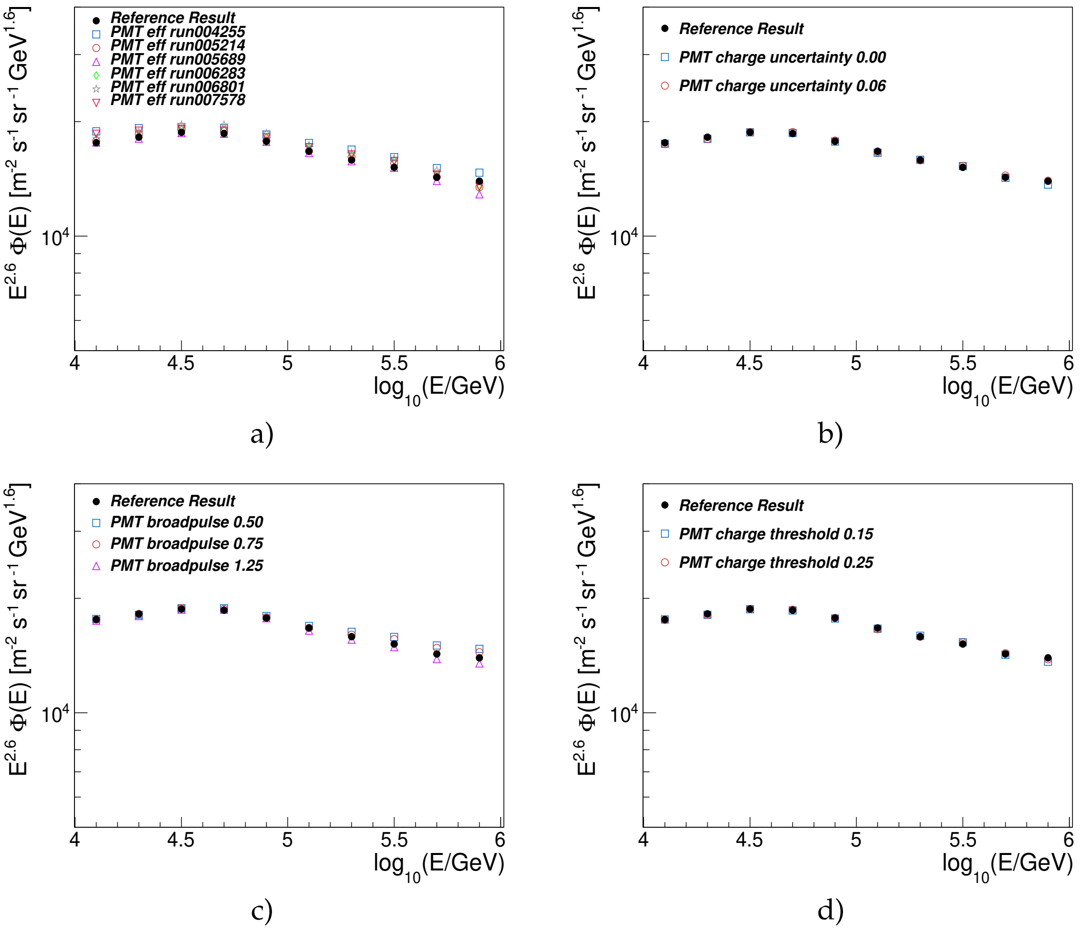

a) b) c) d)

FIGURE 6.5: Impact of PMT systematic uncertainties (efficiency, charge uncertainty, late light, threshold) on the cosmic ray energy spectrum. In all the panels, the total spectrum from this work is shown for comparison (black dots).

```
/data/archive/hawcroot/sim/reco/aerie_svn_42375a/
   config_hawc_v101/daqsim-config_threshold-0p25
```

Fig. 6.5, lower right panel, shows the energy spectra derived from the MC simulations produced with PMT charge thresholds of 0.15 and 0.25 PE, respectively. In the interval $4.1 \leq \log_{10}(E/\mathrm{GeV}) \leq 5.9$, the variations in the energy spectrum range from -2.5% to $+1.0\%$ with respect to the reference result.

6.2.2 Differences between run periods

To quantify the effects of the atmospheric pressure variations in the spectrum, through HAWC's EAS detection frequency, the data was segmented and classified into four seasonal periods: the first one that goes from March to May, the second one from June to August, the third one that spans the months from September to November, and the fourth one that covers the interval from December to February. Following the reconstruction of seasonal energy spectra, the results were compared to the reference result (see Fig. 6.6). The observed variations within $4.1 \leq \log_{10}(E/\mathrm{GeV}) \leq 5.9$ are within $\pm 0.8\%$. Thus, it is concluded that these are minor fluctuations.

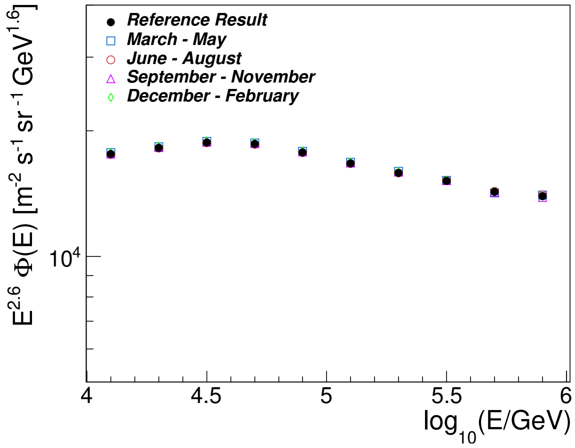

FIGURE 6.6: The total energy spectrum of cosmic rays from this work compared to the spectra obtained for the different seasonal epochs.

6.2.3 Unfolding method

The result derived from the unfolding method is an approximation to the true distribution under study, therefore it is subject to uncertainties inherent from the method itself. In addition, the unfolded result is subject to uncertainties from the prior and the smoothing technique of the method.

The systematic error from the unfolding method was estimated by comparing the reference spectrum to the one derived with the Gold unfolding method [111, 293], which was modified to include statistical errors and a positive definite quadratic response matrix [111]. For comparative consistency, the same prior was used for both techniques. The results from both unfolding procedures are presented in Fig. 6.7. Within $4.1 \leq \log_{10}(E/\mathrm{GeV}) \leq 5.9$, the systematic error fluctuated between -0.2% and 0.0%.

6.2.4 Prior for the unfolding procedure

The second systematic source contribution associated with the unfolding procedure comes from the prior distribution. Four different priors, estimated from the additional models that describe the relative abundances of cosmic rays and presented in section 4.3.4, were employed to calculate the corresponding systematic uncertainty. The results are plotted in the first panel of Fig. 6.8. Overall, it was found that the contributions from this error source to the total systematic bias are almost negligible. In particular, within $4.1 \leq \log_{10}(E/\mathrm{GeV}) \leq 5.9$ the differences with regard to the spectrum range from -1.5% to $+0.2\%$.

6.2.5 Smoothing procedure in the unfolding method

Finally, the systematic error from the smoothing procedure was determined by changing the 353HQtwice algorithm [348] to a broken power-law fit [355] at the intermediate steps during the unfolding. Fig. 6.8, right panel, shows the corresponding result against the reference spectrum. In the energy region $4.1 \leq \log_{10}(E/\mathrm{GeV}) \leq 5.9$, the observed variations range from -1.2% to $+2.0\%$.

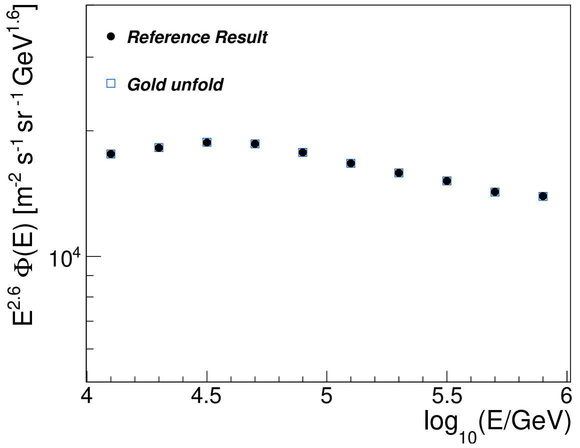

FIGURE 6.7: The total energy spectra of cosmic rays as reconstructed from the implementation of the Bayesian (circles) and Gold (open squares) unfolding procedures, respectively.

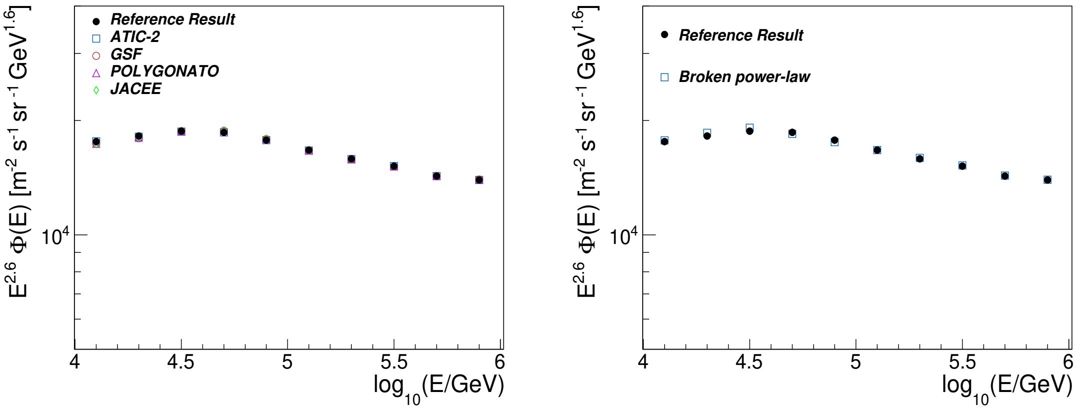

FIGURE 6.8: *Left panel:* HAWC cosmic-ray spectrum variations due to the prior choice in the Bayesian unfolding. *Right panel:* Differential intensity of the all-particle component of cosmic rays obtained from a broken power-law smoothing function in the unfolding. The reference result is presented in both panels for comparison (black circles).

6.2.6 Effective area

Fig. 5.3 shows the effective area, from the QGSJET-II-04 simulations, together with the upper and lower statistical errors. These were used to reconstruct the spectrum and estimate the variations from this systematic source. Fig. 6.9, left panel, shows the corresponding results as an error band, representing the magnitude of the variations in the total energy spectrum of reference. Within $4.1 \leq \log_{10}(E/\mathrm{GeV}) \leq 5.9$, the observed deviations from the reference energy spectrum were found between varies between -2.9% and $+4.3\%$.

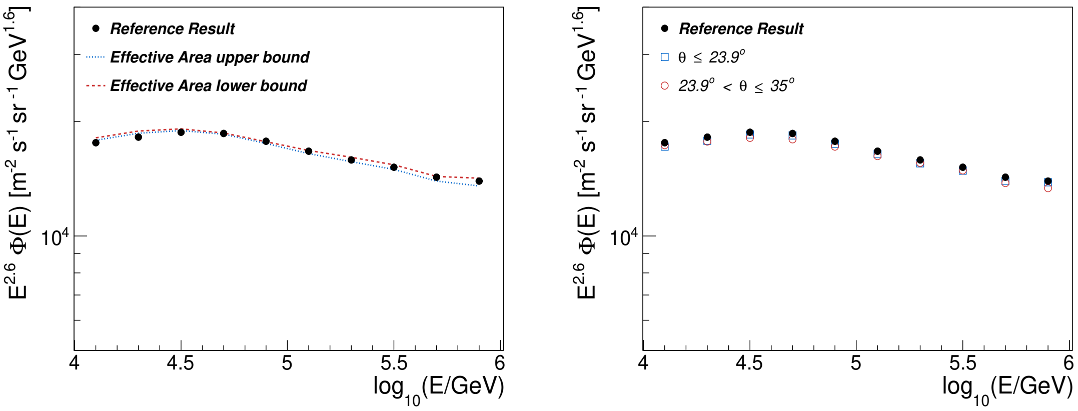

FIGURE 6.9: *Left panel:* The systematic uncertainty in the effective area is represented by an error band. *Right panel:* Energy spectra for vertical (open squares) and inclined (open circles) events. The reference result is presented in both panels for comparison (black circles).

6.2.7 Zenith angle selection

The next uncertainty under study was the dependence of the result with the observed arrival direction. Fig. 6.9, right panel, presents the energy spectra reconstructed for vertical ($\theta < 23.9°$) and inclined ($23.9° < \theta \leq 35°$) showers, respectively. The limits for both zenith angles were chosen this way in order to have the same acceptance in both cases. The zenith angle dependence contributes an uncertainty that varies from -4.2% to 0% within the energy range $4.1 \leq \log_{10}(E/\mathrm{GeV}) \leq 5.9$.

6.2.8 Cosmic-ray mass composition model

The selection of a cosmic-ray composition model introduces a significant source of systematic uncertainty, as it plays a key roll in the reconstruction of the energy spectrum, and has a direct effect in reconstruction procedure of the effective area and the response matrix.

To analyze the influence from this systematic source, the response matrix and the effective area for the reconstruction method were estimated for different relative elemental abundances, selected from the additional models of cosmic-ray relative abundances (c.f. section 4.3.4). Then, for each model, the energy spectrum was unfolded using its corresponding response matrix and effective area. In the energy interval $4.1 \leq \log_{10}(E/\mathrm{GeV}) \leq 5.9$, the systematic error varies between -1.1% and $+11.6\%$.

6.2.9 High-energy hadronic interaction model

To calculate this systematic effect, it was necessary to create a new set of MC simulations with a different high-energy hadronic model, in this case, the EPOS-LHC model [186]. The corresponding simulations for the new model were created using the same CORSIKA version and configuration of the *pass4* data described in section 4.3.4. A total of 6.2×10^7 events were generated for energies ranging from 500 GeV to 5×10^6 GeV and zenith angles below $60°$.

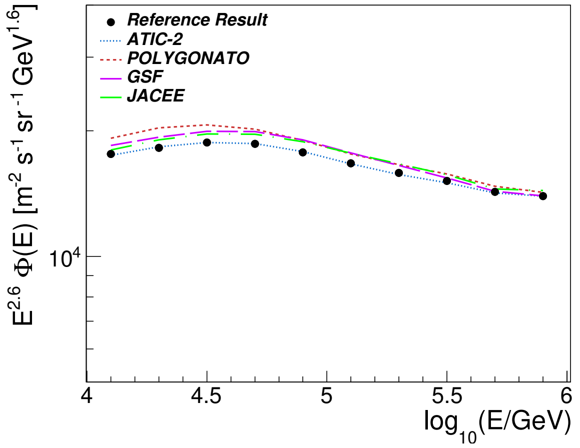

FIGURE 6.10: The unfolded energy spectrum obtained in this work using the nominal MC simulations (solid circles in black) is plotted together with the results obtained from the alternative mass composition models: Polygonato (dashed line in red) [343], GSF (long-dashed line in violet) [344], ATIC-2 (dotted line in blue) [317], and ATIC-2 plus JACEE measurements (dash-dotted line in green) [345].

Then, the response matrix (Fig. 6.11, left panel) and the effective area (Fig. 6.11, right) were calculated with the predictions from EPOS-LHC and the nominal relative abundances of cosmic rays (c.f. section 4.3.4), next the reconstruction method described in Chapter 5 was applied. The unfolded spectrum is shown in Fig. 6.12. When compared to the reference energy spectrum using the QGSJET-II-04 model, the unfolded result using the EPOS-LHC model is displaced towards lower energies. Within $4.1 \leq \log_{10}(E/\mathrm{GeV}) \leq 5.9$, the observed variation in magnitude is within -5.5% 0.0%.

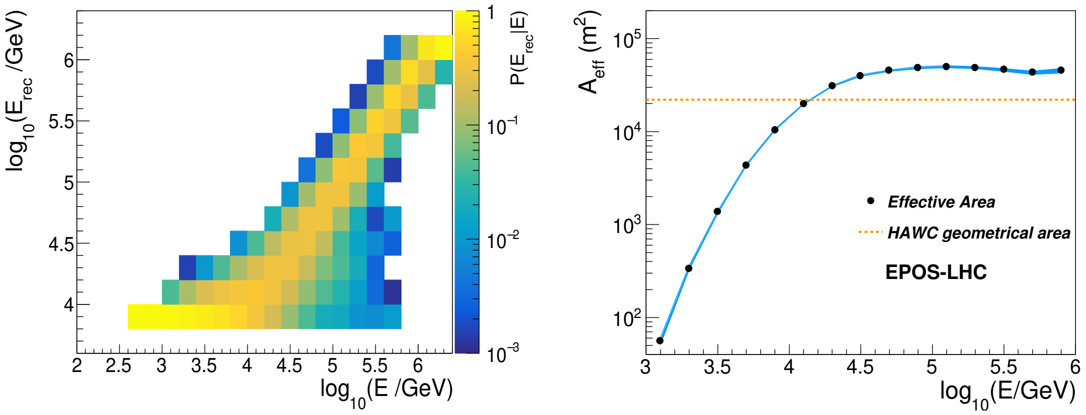

FIGURE 6.11: *Left panel:* The HAWC response matrix. *Right panel:* HAWC effective area. Both elements were calculated from EPOS-LHC model for the all-particle component of the nominal model of cosmic-ray relative abundances. *Image Source:* [278].

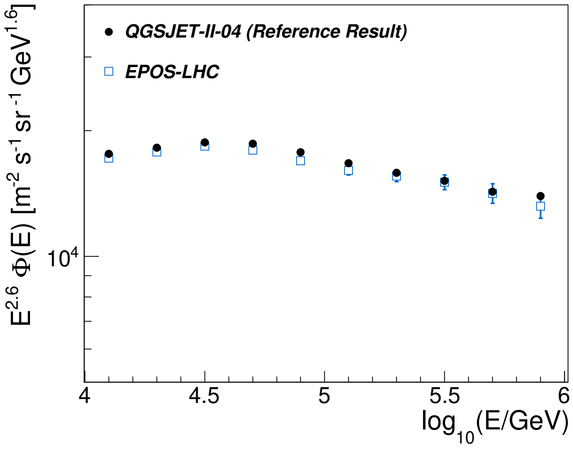

FIGURE 6.12: Unfolded cosmic ray energy spectra from the predictions of the QGSJET-II-04 (solid circles in black) and EPOS-LHC (unfilled squares in blue) models. *Image Source:* [278].

Chapter 7

Analysis on the shape of the energy spectrum

As reported in [278], the total energy spectrum of cosmic rays obtained with the present analysis has a softening in the TeV region, supporting the observations from [22]. In order to validate this observation, a detailed analysis was implemented to determine the spectral shape of the reference result and the exact position of the break under statistical and systematic uncertainties.

7.1 Study on the shape of the spectrum under statistical errors

When our reference result for the energy spectrum is multiplied by a factor scale $E^{2.6}$ (as shown in Fig. 6.2), a softening at tens of TeV becomes evident, suggesting that it deviates from a power-law function. To corroborate this observation, the energy spectrum of Fig. 6.2 was fitted under two distinct hypotheses, a power- and a broken power-law, inside the interval $4.0 \leq \log_{10}(E/\mathrm{GeV}) \leq 6.0$ (see Fig. 7.1). The analytical procedure incorporated the χ^2 difference between the respective fits as a test statistic, TS, to determine if the broken power-law provides a better description of the data. The power-law model is defined as:

$$\Phi(E) = \Phi_0 E^{\gamma_1}. \tag{7.1}$$

In here, the normalization constant for the flux is represented by Φ_0, while γ_1 is the spectral index. In addition, Eq. (4.6) defines the broken power-law model for the analysis, where the constant parameter E_0 was fixed to 10^4 GeV.

The fitting process was made using the minimization library MINUIT from root [349, 356], where a chi-squared minimization was employed (c.f. [357]), incorporating the covariance matrix of the unfolded spectrum to account for statistical correlations [124, 351, 358]. This matrix contains the statistical errors from the measured data and those from the finite number of Monte Carlo simulations (c.f. sections 5.2.1 and 5.2.2).

The results of the fit with Equations (7.1) and (4.6) are shown in table 7.1, respectively.

The test statistics applied to compare the hypothesis was defined as follows:

$$TS = \Delta\chi^2 = \chi_0^2 - \chi_1^2. \tag{7.2}$$

In the above expression, the χ^2 value for the power-law function (the null hypothesis) is denoted as χ_0^2, while the corresponding χ^2 for the broken power-law

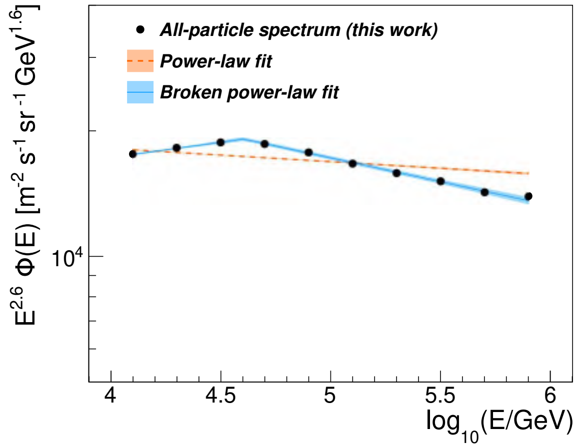

FIGURE 7.1: Fits with a broken power-law (blue bold line) and power-law functions (orange dashed line) to the HAWC energy spectrum data (black points) between 10 TeV and 1 PeV. The shaded error bands correspond to the one-sigma uncertainty for each fit.
Image Source: [278].

function (alternative hypothesis) is represented by χ_1^2 (see Table 7.1). Using the parameters from Table 7.1, the observed TS was $TS_{obs} = 779.97$. To determine the significance of the break in the spectrum, the distribution of the TS was generated under the null hypothesis that the reference result is best described by a power-law function employing the best-fit parameters derived from fitting the HAWC data with Eq. (7.1). This was done by creating toy Monte Carlo spectra using a multivariate Gaussian distribution [359]. Th statistical correlations between adjacent flux points were included by using the covariance matrix of the unfolded HAWC spectrum. We generated a set of 3.5×10^6 toy spectra were created using the described procedure. The observed test statistic, TS_{obs}, was larger than all the TS values obtained from the toy spectra, resulting in a p-value less than 2.86×10^{-7}. This result corresponds to a statistical significance greater than $5\,\sigma$, strongly suggesting that the reference result is best characterized by the broken power-law model.

7.1.1 Study on the shape of the spectrum under systematic uncertainties

Following the methodology described in [31], systematic uncertainties were integrated into the analysis to provide a complete characterization of the spectral break and its significance. This involved fitting the broken power-law (Eq. (4.6)) to the unfolded spectra from each systematic source listed in section 6.2. The impact of each systematic source was evaluated by estimating the minimum and maximum variations of the fitted parameters compared to the reference values shown in Table 7.1. Finally, the total systematic bias was computed by combining these individual uncertainties in quadrature, and the final results are provided in Table 7.1.

In particular, for the parameters γ_1 and γ_2 from Eq. (4.6), their statistical and systematic uncertainties were estimated with the procedures described above so as to analyze the significance of the spectral index change, $\Delta\gamma = \gamma_2 - \gamma_1$. The results obtained for $\Delta\gamma$, uncertainties included, are

- $\Delta\gamma = -0.19 \pm 0.01\,\text{(stat.)}\,^{+0.06}_{-0.07}\text{(sys.)}$,

Parameter	Value
Power law	
Φ_0	$10^{4.38\pm0.01(\text{stat.})^{+0.18}_{-0.11}(\text{sys.})}\ \text{m}^{-2}\,\text{s}^{-1}\,\text{sr}^{-1}\,\text{GeV}^{-1}$
γ_1	$-2.631\pm0.001(\text{stat.})^{+0.14}_{-0.03}(\text{sys.})$
χ_0^2	782.85
ν(ndof)	8
Broken power law	
Φ_0	$10^{4.24\pm0.001(\text{stat.})^{+0.05}_{-0.02}(\text{sys.})}\ \text{m}^{-2}\,\text{s}^{-1}\,\text{sr}^{-1}\,\text{GeV}^{-1}$
γ_1	$-2.53\pm0.01(\text{stat.})^{+0.04}_{-0.05}(\text{sys.})$
γ_2	$-2.71\pm0.01(\text{stat.})^{+0.03}_{-0.04}(\text{sys.})$
E_{br}	$\left[40.2\pm1.0(\text{stat.})^{+6.2}_{-6.4}(\text{sys.})\right]$ TeV
$\Delta\gamma=\gamma_2-\gamma_1$	$-0.19\pm0.01(\text{stat.})^{+0.06}_{-0.07}(\text{sys.})$
χ_1^2	2.88
ν(ndof)	6

TABLE 7.1: The parameters obtained from fitting the reference result (Fig. 6.2) with the broken power-law function (see Eq. 4.6) and power-law funtion (c.f. Eq. 7.1) models are summarized in here. The table also includes the χ^2, and the number of degrees of freedom (ndof) for each model. Statistical errors for each parameter correspond to the 1σ confidence interval.

representing a 3.1σ deviation from zero.

7.2 Energy resolution

A potential source of systematic error in the reference result from Fig. 6.2 is the uncertainty in the energy scale. This uncertainty propagates to the flux according to the following formula [360]:

$$\frac{\delta\Phi}{\Phi} = -(\gamma+1)\frac{\delta E}{E}. \tag{7.3}$$

Here, the parameter γ represents the spectral index at a specific energy E. The overall systematic error present in the energy scale, see Fig. 7.2, was reconstructed with the best fitted γ parameter from Eq. (4.6) (c.f. Table 7.1) and the total systematic error in the flux $\delta\Phi$ from Fig. 6.3. As plotted in Fig. 7.2, the total energy uncertainty at the lowest (highest) energies, $\log_{10}(E/\text{GeV}) = 4.1(5.9)$ ranges from -2.4% (-6.8%) to $+7.9\%$ $(+4.7\%)$.

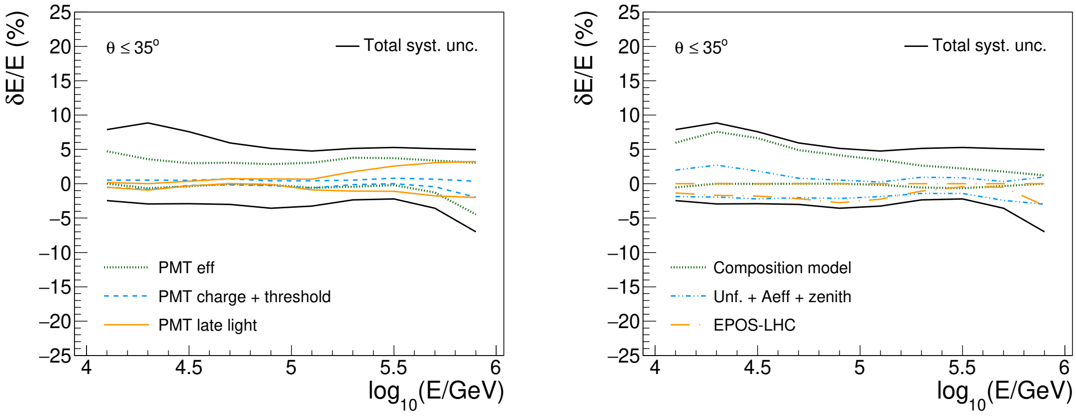

FIGURE 7.2: Individual contributions from the sources of systematic bias (see section 6.2) to the total relative systematic uncertainty in the energy scale (bold black line).
Image Source: [278].

The next chapter will cover a discussion of the reference result (see Fig. 6.2) that is reported in the present thesis, the total energy spectrum measured with HAWC. The HAWC spectrum will then be compared against other experimental measurements of the total spectrum. Additionally, several theoretical models that potentially explain the observed softening in the spectrum at $40.2 \pm 1.0(\text{stat.})^{+6.2}_{-6.4}(\text{sys.})$ TeV will be explored.

Chapter 8

Discussion

The total energy spectrum derived with the present analysis exhibits a softening at $40.2 \pm 1.0(\text{stat.})^{+6.2}_{-6.4}(\text{sys.})$ TeV [179], result that is consistent (within systematic uncertainties) with a previous HAWC measurement of the spectrum with a softening occurring at $45.7 \pm 1.1(\text{stat})$ TeV [5]. In the present study, the systematic uncertainties are reduced significantly compared to the earlier HAWC analysis [5] as a result of the analysis of a larger data sample and an improved understanding and modeling of the PMT performance, which combined with updates on the reconstruction algorithms, and the increase of the zenith angle range, allowed to extend the analysis of the energy spectrum with HAWC up to 1 PeV. In addition, in comparison with the previous work, the analysis here shown features the usage of the QGSJET-II-04 hadronic interaction model in the unfolding. One interesting difference appears between the previous and the updated results on the spectrum in HAWC: the position of the spectral break in the result from [22] is shifted to higher energies. This difference is attributed to a systematic effect in the analysis from [22], where the implementation of a power-law fit in their unfolding smoothing algorithm produces a flattening of the measured spectrum. For the present work, the energy spectrum of cosmic rays was reconstructed using a data sample of HAWC collected between June 11th, 2015 to December 31st, 2020, with an effective observational time of 5.3 years. Since 2020, the observatory has continued to measure new cosmic ray data. The final result using 5.3 years of data is robust, adding more data to the sample under analysis would not produce a different result from the final one, nor would it affect the shape of the energy spectrum. Variations in the systematic errors would be expected to be less than 1%, and the statistical errors due to the size of experimental sample are already $\ll 1\%$. In addition, the production of experimental data using the *pass 4* algorithms only covers the DAQ period between June 11, 2015, and January 14, 2021. This sets a limit on the experimental sample selected for the present analysis to approximately 5.3 years of effective observational time.

The HAWC spectrum [278] is contrasted to cosmic-ray data from other direct missions and indirect experimental facilities for a wider discussion of the result, as shown in Fig. 8.1. From this comparison, it is observed that the energy spectrum measured with HAWC in this work [278] is consistent with measurements from NUCLEON [23] within 20 TeV $\leq E \leq$ 1 PeV, within systematic uncertainties. In addition, the result of the present analysis is consistent with the observations reported by NUCLEON about the detection of an spectral break around 10 TeV [23]. Between 10 TeV and 200 TeV, HAWC data exhibits a fair agreement with ATIC-2 spectrum [7], and in the range 100 TeV $\leq E \leq$ 1 PeV, with the TAIGA-HiScore data [259]. Moreover, the HAWC and TUNKA-133 results [263] are in good agreement around 1 PeV. In addition, within the energy range of 0.3 PeV and 1 PeV, the HAWC spectrum is comparable to ICETOP [245] and LHAASO-KM2A [114] measurements, within systematic effects. In contrast, above 100 TeV, the mesurements from HAWC are higher than ARGO-YBJ [361] and TIBET results [265].

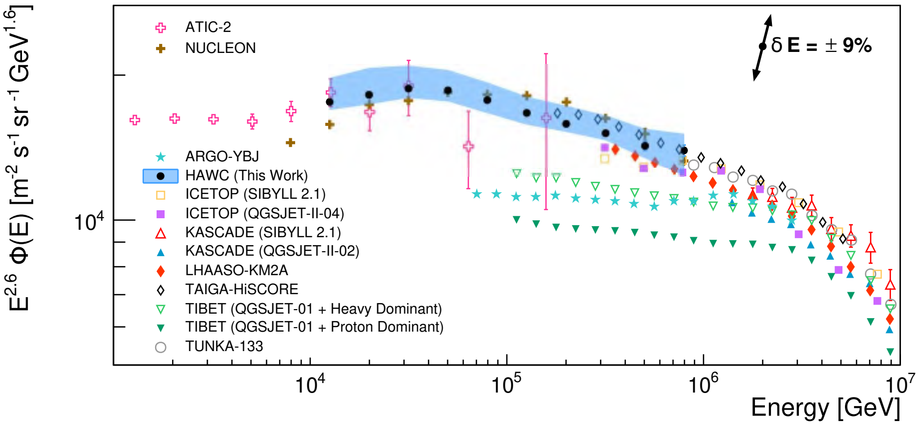

FIGURE 8.1: The all-particle cosmic ray energy spectrum from this work [278] (solid black circles) with statistical (vertical error bars) and systematic uncertainties (error band in blue) is compared to other measurements of the spectrum around the knee. The direct measurements (statistical uncertainties only) are from the ballon-borne ATIC-2 (open crosses in pink) [7] and the NUCLEON satellite (solid brown crosses) [23], respectively. For the comparison, the data from recent indirect experiments were selected . This includes the observations from (statistical uncertainties only) ICETOP (SYBILL 2.1, open squares in orange; QGSJET-II-04, full squares in violet) [245], LHAASO-KM2A (solid diamonds in red) [114], and TAIGA-HISCORE (open diamonds in black) [259]. To extend the discussion, some of the most representative indirect measurements of the spectrum (statistical uncertainties only) in the region of interest are also shown to: ARGO-YBJ (teal stars) [362], KASCADE (QGSJET-II-02, up-facing full triangles in red; SYBILL 2.1 open up-facing triangles in blue) [109, 111], , TIBET-III (QGSJET-01 + Heavy Dominant, open down-facing triangles in green; QGSJET-01 + Proton Dominant, down-facing full triangles in dark green) [265] and TUNKA (gray open circles) [263]. All the measurements were multiplied by $E^{2.6}$ to enhance and visualize their features. *Image Source:* [278].

Classical acceleration and propagation models like [32–41] predict a featureless energy spectrum below the knee, with a spectral index γ between -2.6 and -2.7. This predictions seem to be in agreement with the main result from this work at $E >$ 40.2 TeV, where the spectral index was found to be $\gamma = -2.71 \pm 0.01(\text{stat.})^{+0.03}_{-0.04}(\text{sys.})$. However, for $E \leq 40.2$ TeV, the spectral index changes to $\gamma = -2.53 \pm 0.01(\text{stat.})^{+0.04}_{-0.05}(\text{sys.})$, which deviates from the predictions of the previous models. Although the causes behind the spectral features observed at TeV energies in the total and individual element cosmic ray spectra are not yet fully understood, certain models speculate that they could be linked to:

A nearby source: One hypothesis suggests that the spectral cutoffs could be produced by a cosmic-ray accelerator situated within 500 parsecs of Earth, possessing cutoff rigidities below approximately 10 TV [47]. Potential candidates for such a local source include a 2 or 3 Myr old supernova at a range of 100 − 200 parsecs away from the planet Earth [157, 158, 363], or the well-known Geminga SNR [45]. The physical phenomena linked to the production of the

TeV features might also involve multiple local sources. For instance, [45] suggests, that along with Geminga, a nearby SNR (300 pc away, 0.3 Myr old) could fit the data if it lies in a particular direction in the sky.

New cosmic-ray sources: Some models propose a scenario where, a significant TeV contribution arises from new cosmic-ray sources in the Milky Way dominating the TeV region above the component of cosmic rays generated by galactic hadronic Pevatrons, directly linked to the production of the spectrum *knee structure* at approximately 3×10^{15} eV. It is predicted that these new sources have maximum rigidities within 10 TV and 100 TV. These TeV cosmic-ray sources could be supernovae within the interstellar medium, while Pevatrons could be massive stellar explosions associated to O and B stars [46, 364]. In contrast, the model from [365] proposes that supernova remnants within the ISM without magnetic field amplification at their shocks could be responsible for the cosmic ray spectrum across the TeV energy region, while the total spectrum of PeV cosmic rays could be ruled by SNR with magnetic field amplification.

A reacceleration mechanism within the interstellar medium (ISM): An alternative explanation for the spectral structures that have been observed at dozens of TeV involves the reacceleration of the primary particles, generated inside the galaxy, by local shocks. For example, in [43, 44, 366] the authors suggest that these features are originated from the local reacceleration of galactic cosmic rays by nearby shocks, within 3 to 10 pc from the solar system. In addition to this mechanism, the spectrum is shaped by turbulence in the magnetic fields across the ISM, with rigidities above 50 TV, and by the deflection of the reaccelerated particles with rigidities below 0.5 by the ISM flow, thus preventing their arrival to the Sun. The ϵ-Eridani star and the stelar bow shock associated to it is a potential region for the reacceleration of preexisting galactic cosmic rays [43, 44]. ϵ-Eridani is located approximately at 3.2 pc from the solar system.

All these hypotheses are subject to the constraints imposed by cosmic-ray data of the energy spectra, relative abundances of the mass components, and the arrival direction anisotropies.

A recent HAWC study of the mass composition of cosmic rays within the interval 10 TeV $\leq E \leq$ 1 PeV, suggests that the softening observed in the TeV energy spectrum is attributed to the combined spectral breaks of light primary nuclei along with a growing contribution of heavier nuclei [26]. The experimental observation of spectral cutoffs in the spectra for the light mass components of cosmic rays at dozens of TeV provides a potential explanation for the spectral change observed in the all-particle spectrum of cosmic rays at similar positions. The existence of these spectral features, for light cosmic-ray nuclei, was first suggested by CREAM-II [27]. These results were followed by the observation of a decrease in the spectral index from the energy spectrum of hydrogen nuclei at 10 TeV according to NUCLEON data [25], while CALET [30] and DAMPE [28] observed a similar behavior at 9 TeV and 14 TeV, respectively. Also, according to the observations made by CALET [31] (DAMPE [29]), the helium nuclei spectrum has a break located at 30 TeV (34 TeV). Moreover, a study of the H+He spectrum with HAWC revealed a softening at 24 TeV [124], which was later confirmed by DAMPE with the report of a spectral break in the H+He component at $\sim$ 29 TeV [367]. Fig. 8.2 compares the CALET, DAMPE, NUCLEON, and HAWC measurements of light cosmic ray mass groups with the main result of this work. From here, it possible to notice that the spectral features

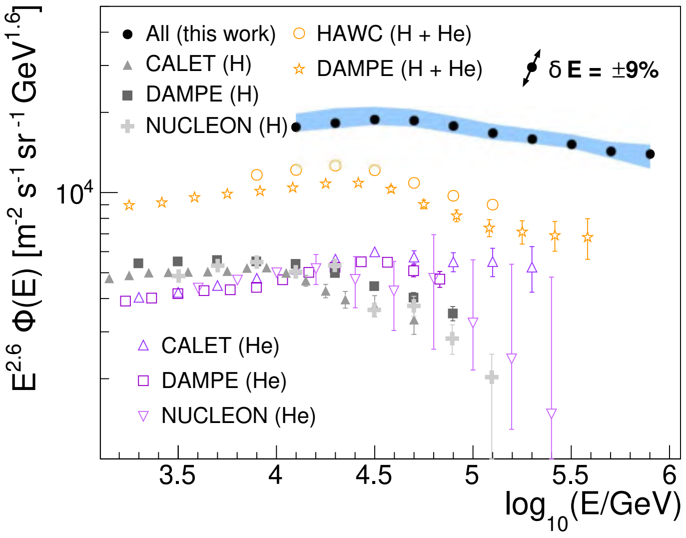

FIGURE 8.2: The total energy spectrum (this work [278], solid circles in black) compared to H (solid symbols), He (open triangles and squares), and H+He (open stars and circles) spectra from CALET [30, 31], DAMPE [28, 29, 367], NUCLEON [25], and HAWC [124], respectively. For all data points, the statistical errors are presented with vertical bars, while the systematic uncertainty of the total energy spectrum is shown as an error band. *Image Source:* [278].

in light nuclei appear at energies close to the softening observed by HAWC in the total spectrum, but typically at lower energy values. HAWC continues to investigate the connection between the observed softening in the total spectrum and the relative abundances of cosmic-ray nuclei with TeV energies [26].

Determining the precise source of the spectral structure in the total energy spectrum of cosmic rays at dozens of TeV is a challenge that requires further investigation into the arrival direction anisotropies and elemental spectra below the knee with larger statistics and smaller systematic uncertainties. Under these conditions, progress will depend on theoretical advancements and the complementary measurements provided by direct (e.g., CALET and DAMPE) and indirect (e.g., HAWC and LHAASO [219]) cosmic ray experiments.

Chapter 9

Conclusions

Together with the measurements of NUCLEON [23], the results of the present study serve as a connection for direct and indirect measurements of the TeV cosmic-ray spectrum. The systematic bias in the reconstruction of the spectrum of this work are dominated by uncertainties relative to the modeling of the PMTs and the mass-composition model of cosmic rays employed in the analysis, as well as variations within run periods.

This work presents the all-particle cosmic ray energy spectrum within 10^{13} eV $\leq E \leq 10^{15}$ eV, based on 5.3 years of effective cosmic-ray-data measured with HAWC. It is important to emphasize that the HAWC spectrum (this work) reveals a softening at $40.2 \pm 1.0(\text{stat.})^{+6.2}_{-6.4}(\text{sys.})$ TeV, and a softening where the spectral index falls from $\gamma = -2.53 \pm 0.01(\text{stat.})^{+0.04}_{-0.05}(\text{sys.})$ to a value of $\gamma = -2.71 \pm 0.01(\text{stat.})^{+0.03}_{-0.04}(\text{sys.})$ with a statistical significance of at least 5σ (3.1σ under systematic uncertainties). This result is consistent with the previous observations from NUCLEON [23, 24] and HAWC [22, 368–370]. In particular, within 10 TeV $\leq E \leq$ 1 PeV, the HAWC (this work) and NUCLEON measurements are consistent under systematic errors, while at energies close to 10^{13} eV, HAWC's measurements concur with the ballon-borne data from ATIC-2 [7]. At 10^{15} eV, the HAWC spectrum is consistent with the measurements from ICETOP [245], LHAASO-KM2A [114], TAIGA-HiScore [259], and TUNKA-133 [263] ground-base experiments. In contrast, HAWC observes a higher intensity in the spectrum than ARGO-YBJ [361] and TIBET-III [265].

Finally, throughout this work:

- It has been proven that the reconstructed energy spectrum with HAWC is a robust result that contributes to bridge direct and indirect data of the all-particle energy spectrum of cosmic rays between 10^{13} eV $\leq E \leq 10^{15}$ eV, along with the satellite mission NUCLEON [23, 24].

- In addition, it was shown that this is the first result on the energy spectrum within energies 10^{13} eV $\leq E \leq 10^{15}$ eV with high statistics from and indirect experiment.

- The reference energy spectrum from this thesis validates the observation of the spectral cuttof in the TeV region. In addition, this result contributes with experimental constrains to theoretical models on the acceleration and propagation of galactic cosmic-ray primaries.

- Proves the ability of the water Cherenkov technique for measurements of cosmic rays within 10^{13} eV $\leq E \leq 10^{15}$ eV. This validates the implementation of this technique in future experimental facilities such as SWGO for the study of TeV cosmic rays [371].

Future Work

At HAWC, the reconstruction method for determining the primary energy of cosmic rays is currently being updated and optimized using Machine Learning techniques [372] and QGSJET-II-04 [48]. The resulting estimator will be incorporated into new, higher-statistics MC simulations. The later will include an improved description of the detector response and the systematic effects [285]. These simulations will then be employed at future studies to update the analysis of the total cosmic ray energy spectrum. It is expected that these updates will allow to extend the analysis up to the knee.

Currently, a new analysis of the energy spectrum is being developed to optimize the energy resolution in the final result, through the unfolding of an energy distribution with multivariate energy bin widths. This analysis will offer a more detailed description of the softening in the spectrum, and will try to reduce the lower limit of the energy range of study.

The HAWC collaboration is performing an advanced study of the mass composition and the spectra of light and heavy primaries [26], alongside an updated analysis of the cosmic-ray arrival anisotropies [373], in order to provide new insights on the origin of the softening in the total energy spectrum.

Along with HAWC, other experimental facilities, LHAASO included [20, 114, 273], are currently seeking to improve the measurements of the total energy spectrum in the TeV region and to extend measurements to lower energies to connect with the region dominated by direct experiments. In addition, direct experiments such as DAMPE have also been able to extend full-spectrum measurements up to approximately 200 TeV, also observing a spectral feature at dozens of TeV [374]. Future cosmic-ray satellite-born missions like HERD will explore the all-particle cosmic-ray energy spectrum within the interval from 30 GeV and the PeV regime [375].

Appendix A

Unfolding techniques

In chapter 5, we described the Bayesian unfolding method [50–52], which is the core reconstruction method in this thesis. In this appendix, we will provide a brief explanation on alternative unfolding techniques that were implemented here for comparative studies, in particular, on the reduced cross-entropy method, which is a non-iterative approach, and the Gold's unfolding technique, which is an iterative approach.

A.1 Gold unfolding method

The unfolding method proposed by R. Gold in 1964 [293] is useful in situations where the input measured distribution N_{rec} contains non-negative entries, since it provides a positive solution for the unfolded distribution N_T, ensuring that it represents a physically plausible solution to Eq. (5.2). For this iterative unfolding technique to approach to a stable and accurate solution, the response matrix R must meet two conditions:

- It must be a square matrix.
- It must be positive definite.

Under these conditions, it is possible to establish a relation between N_T and N_{rec} through a diagonal transformation matrix, D,

$$N_T = DN_{\text{rec}}, \quad \text{with } D_{ii} = N_{T,i}/N_{\text{rec,i}}, \quad i = 1, 2, ..., n. \tag{A.1}$$

The elements of this matrix, D_{ii}, represent the correction factors applied to each bin of the measured distribution to approximate the true distribution. The elements of D are computed through an iterative process defined by the following expression

$$D_{ii}^{k+1} = \frac{D_{ii}^{k} N_{\text{rec,i}}}{\sum_{j=1}^{n} R_{ij} D_{jj}^{k} N_{\text{rec,j}}}, \quad i, j = 1, 2, ..., n. \tag{A.2}$$

In the above expression, the response matrix is represented by R, and the iteration depth is given by k. By substituting the iterative relation for D from Eq. (A.2) into Eq. (A.1), it is possible to obtain a recursive relation to approximate N_T:

If we substitute Eq. (A.2) into Eq. (A.1), we obtain an iterative relation for N_T,

$$N_{T,i}^{k+1} = \frac{N_{T,i}^{k} N_{\text{rec,i}}}{\sum_{j=1}^{n} R_{ij} N_{T,j}^{k}}. \tag{A.3}$$

The final solution obtained through this iterative procedure is independent of the chosen prior distribution. This is a valuable feature in scenarios where prior knowledge about the true distribution might be limited or uncertain.

Moreover, this formalism was extended to scenarios where the response matrix is not necessarily quadratic or positive definite, and to incorporate statistical uncertainties into the unfolding process [111]. First, Eq. (5.2) is transformed by replacing R and N_{rec} by $R^T R$ and $R^T N_{\text{rec}}$, respectively. Then, to incorporate the statistical errors, $\sigma_{stat}(N_{\text{rec,i}})$, into the unfolding procedure, Eq. (5.2) is multiplied by a diagonal matrix C defined as

$$C_{i,j} = \delta_{i,j}/\sigma_{stat}(N_{\text{rec,i}}). \tag{A.4}$$

Consequently, the recursive relation for N from Eq. (A.3) is modified to

$$N^{k+1}_{T,i} = \frac{N^k_{T,i} N_{r,mod,i}}{\sum_{j=1}^{n} R_{mod,ij} N^k_{T,j}}, \tag{A.5}$$

where the modified measured distribution $N_{\text{rec,mod}}$ and the modified response matrix R_{mod} are given by $N_{\text{rec,mod}} = R^T C C N_{\text{rec}}$, and $R_{\text{mod}} = R^T C C R$, respectively.

For the purpose of estimating systematic uncertainties related to the implementation of different unfolding algorithms in this work, the Gold unfolding method was employed using the modifications described above [111]. The results obtained using this technique are presented and compared with those from other unfolding methods in Figs. 6.7 and A.1.

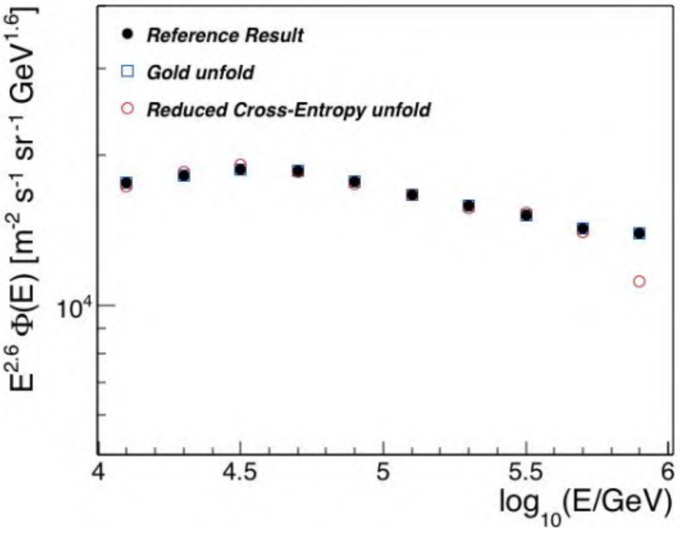

FIGURE A.1: HAWC energy spectra derived using three different unfolding methods: Bayes unfolding (black dots), reduced cross entropy (open circles in red), and Gold procedure (open squares in blue).

A.2 Reduced cross-entropy method

The non-iterative unfolding techniques are an alternative approach employed for approximating the true distribution of a measured quantity that has been distorted by the response of a detector or system [347, 350]. In general, these methods include a regularization procedure to impose conditions on the unfolded distribution, for example, on the smoothness or the amplitude of the result, among others. This is typically achieved by formulating the unfolding procedure as a minimization problem with a χ^2 expression plus a regularization function. The quantity to be minimized takes the general form:

$$F(N_T) = \chi^2(N_T) + \tau S(N_T) = \sum_{i=1}^{n_r} \left[\frac{N_{R,i} - \sum_{j=1}^{n_t} R_{ij} N_{T,j}}{\sigma(N_{R,i})} \right]^2 + \tau S(N_T). \tag{A.6}$$

Here, $\sigma(N_{R,i})$ represents the statistical uncertainty of the measured data in the i-th bin. The regularization function, $S(N_T)$, contains the condition on the unfolded distribution, and its influence over the final solution is ruled by the regularization parameter τ. For example, if $\tau = 0$ the solution to Eq. (5.2) will be ruled by statistical fluctuations and bin-to-bin correlations. Meanwhile, a large value of τ implies a stronger influence of the regularization term on the final unfolded solution.

The specific functional form of $S(N_T)$ determines the nature of the imposed condition [347]. One particular example is the regularization function derived from the von Neumann-Shannon entropy of information, $H(N_T)$, which is the kernel function in the maximum entropy unfolding method [350, 376]. $H(N_T)$ has the form:

$$S(N_T) = -H(N_T) = \sum_{j=1}^{n_t} N_{T,j} \log(N_{T,j} / \sum_{k=1}^{n_t} N_{T,k}). \tag{A.7}$$

This non-iterative approach combines a least-squares fit to the data with the principle of maximum entropy, yielding positive solutions and favoring smoother solutions [350]. However, for large values of regularization parameter, the maximum entropy technique tends to pull the unfolded result towards a uniform distribution [350].

Another non-iterative regularized method is the reduced-cross entropy. Developed by M. Schmelling, this method is based on the maximum entropy unfolding and the cross-entropy principle [350]. The reduced-cross entropy technique incorporates prior knowledge, N_{prior}, about the expected true distribution, and its regularization function is given by [352]:

$$S(N_T) = \sum_{j=1}^{n_t} N_{T,j} \log(N_{T,j} / N_{\text{prior,j}}), \tag{A.8}$$

The above expression is known as *cross-entropy* or Shannon-Jaynes entropy [377]. This term measures the degree of similarity between the unfolded solution and the prior distribution[1]. In the reduced cross-entropy technique, the functional form of the cross-entropy is employed in Eq. (A.6) as the regularization function.

To perform a cross-check of the main result obtained with the Bayesian unfolding procedure in this work, the analysis of the total spectrum of cosmic rays was repeated using the reduced cross-entropy technique as the unfolding method. This alternative unfolding method was first validated on a MC toy model before being applied to the measurements of HAWC for the final cross-check. For the unfolding test, the prior distribution, $N_{prior}(E)$ is based on the nominal MC simulations

---

[1] In the case that there is no prior information available, this method allows to use a uniform distribution [352, 378].

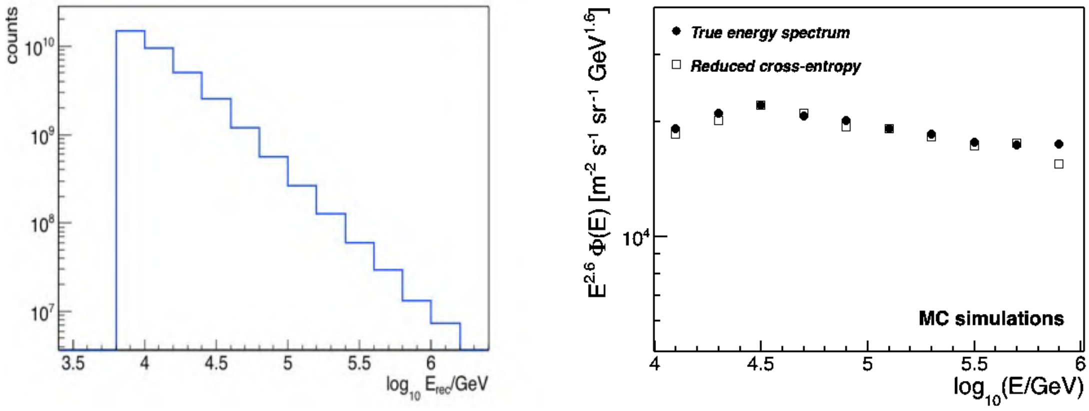

FIGURE A.2: *Left panel:* Energy distribution for the reduced cross-entropy method. This prior distribution $N_{prior}(E)$ is based on the nominal QGSJET-II-04 simulations and the total energy spectrum from [22], using our nominal composition. *Left panel:* Results from the MC tests of the reduced cross-entropy method, showing the true energy spectrum (black circles) compared to the unfolded spectrum (open squares in blue).

with additional weights applied to the energy distribution to have a broken power-law behavior consistent with Eq. (4.6) in the total energy spectrum (see Fig. A.2, left panel). The new spectrum have parameters $E_{\mathrm{break}} = 10^{4.7}$ GeV, $\gamma_1 = -2.49$ and $\gamma_2 = -2.71$, as it was found in [22]. The toy model was generated using the nominal model (described in section 4.3.4). The energy spectrum of the toy model was designed to match the spectral shape of the unfolded reference result (c.f. Fig. 6.2). The regularization parameter was set to $\tau = 0.052$, which was found by finding a minimum for $WMSE$ (as defined in section 5.2).

Fig. A.2, right panel, shows the unfolded energy spectrum for the toy MC distribution using the reduced cross-entropy method, compared to the true energy spectrum of the toy MC model. This comparison reveals that the spectra are consistent with each other. Nonetheless, at the highest energy bin, the unfolded result seems to be affected by statistical fluctuations, due to limited MC statistics in this energy region, causing a deviation of the result from the true MC spectrum.

After the validation of the reduced cross-entropy technique, it was applied to the measured energy distribution with the same prior distribution and the value of the regularization parameter obtained from the MC scenario. The unfolded spectrum obtained with this technique using HAWC data is shown in Fig. A.1, where it is compared with the spectra reconstructed using the Bayesian and Gold unfolding methods, showing good agreement. The presence of fluctuations around 1 PeV is also noted, attributed to the limited statistics in MC simulations in this energy region.

Appendix B

Published work

The analysis from which this thesis is derived was published in [278]. An early version of the analysis was cited in [163]. In addition, this analysis has been broadly discussed in national and international specialized forums, and preliminary results have been published in [368–370, 379].

Bibliography

[1] J. R. Hörandel, “Models of the knee in the energy spectrum of cosmic rays”, Astroparticle Physics **21**, 241–265 (2004).

[2] S. Mollerach and E. Roulet, “Progress in high-energy cosmic ray physics”, Progress in Particle and Nuclear Physics **98**, 85–118 (2018).

[3] M. Kachelrieß, A. Neronov, and D. Semikoz, “Cosmic ray signatures of a 2–3 Myr old local supernova”, Phys. Rev. D **97**, 063011 (2018).

[4] V. I. Zatsepin and N. V. Sokolskaya, “Three component model of cosmic ray spectra from 10 GeV to 100 PeV”, Astronomy and Astrophysics **458**, 1–5 (2006).

[5] N. L. Grigorov, et al., [PROTON], “Study of energy spectra of primary cosmic rays at very high energies on the PROTON series of satellites”, Space Research XII, Academic Verlag, Berlin **1617** (1972).

[6] N. N. L. Grigorov et al., “The study of cosmic rays on the proton artificial earth satellite”, Cosmic Rays, 227–246 (1975).

[7] A. D. Panov, et al., [ATIC], “Energy spectra of abundant nuclei of primary cosmic rays from the data of ATIC-2 experiment: Final results”, Bull. Russ. Acad. Sci. Phys. **73**, 564–567 (2009).

[8] Y. S. Yoon, et al., [CREAM], “Cosmic-Ray Proton and Helium Spectra from the First CREAM Flight”, Astrophys. J. **728**, 8 (2011).

[9] V. Zatsepin et al., “Energy spectra of primary protons and other nuclei in energy region 10-100 TeV/nucleus”, in 23rd international cosmic ray conference (icrc23), Vol. 2, edited by D.A. Leahy, R.B. Hicks, and D. Venkatesan (World Scientific, Singapore, 1993) (1993), p. 13.

[10] K. Asakimori, et al., [JACEE], “Energy Spectra and Elemental Composition of Nuclei above 100 TeV from a Series of JACEE Balloon Flights”, Arxiv preprint astro-ph/9509091 (1995).

[11] V. A. Derbina, et al., [RUNJOB], “Cosmic-ray spectra and composition in the energy range of 10-1000 TeV per particle obtained by the RUNJOB experiment”, Astrophys. J. **628**, L41–L44 (2005).

[12] I. P. Ivanenko, et al., [SOKOL], “Energy spectra of cosmic rays above 2 TeV as measured by the SOKOL apparatus”, in 23rd international cosmic ray conference (icrc23), volume 2, Vol. 2 (1993), p. 17.

[13] E. Atkin, et al., [NUCLEON], “The NUCLEON space experiment for direct high energy cosmic rays investigation in TeV – PeV energy range”, Nucl. Instrum. Methods Phys. Res. Sect. A **770**, 189–196 (2015).

[14] T. V. Danilova, et al., [Tien-Shan], “The energy spectrum of the primary cosmic rays in the range 10^{13} - 10 ^{16} eV”, in 15th international cosmic ray conference, vol. 8. published: budapest: dept. of cosmic rays, central research institute for physics of the hungarian academy of sciences, 1977. international union of pure and applied physics; bulgarska akademiia na naukite. lccn: 78-307721 12 volumes, p. 129 (1977).

[15] H. Yoshi, et al., [BASJE], “Composition and energy spectrum of cosmic rays above 30 TeV”, in 24th International Cosmic Ray Conference, Vol. 2, held August 28-September 8, 1995 in Rome, Italy. Edited by N. Iucci and E. Lamanna. International Union of Pure and Applied Physics, 1995., p.703 (1995).

[16] Y. Yu, et al., [DAMPE], “The Plastic Scintillator Detector at DAMPE”, (2017).

[17] V. S. Gallo, “Studies on Helium flux with DAMPE”, 35th International Cosmic Ray Conference (2017).

[18] Q. An, et al., [DAMPE], “Measurement of the cosmic ray proton spectrum from 40 GeV to 100 TeV with the DAMPE satellite”, Science advances **5**, eaax3793 (2019).

[19] A. Carraminana, E. Mendoza, J. Nava, and L. Vázquez, *The HAWC experiment at the Parque Nacional Pico de Orizaba A feasibility study for the HAWC Collaboration*, (2007) `https://www.hawc-observatory.org/publications/docs/repfin.pdf`.

[20] X.-H. Ma et al., “LHAASO Instruments and Detector technology”, Chinese Physics C **46**, 030001 (2022).

[21] S. Navas, et al., [Particle Data Group], “Review of particle physics”, Phys. Rev. D **110**, 030001 (2024).

[22] R. Alfaro, et al., [HAWC], “All-particle cosmic ray energy spectrum measured by the HAWC experiment from 10 to 500 TeV”, Phys. Rev. D **96** (2017).

[23] [. V. Grebenyuk et al., “Energy spectra of abundant cosmic-ray nuclei in the NUCLEON experiment”, Advances in Space Research **64**, 2546–2558 (2019).

[24] E. Atkin, et al., [NUCLEON], “First results of the cosmic ray NUCLEON experiment”, J. Cosmol. Astropart. Phys. **2017**, 20 (2017).

[25] E. Atkin, et al., [NUCLEON], “New universal cosmic-ray knee near a magnetic rigidity of 10 TV with the NUCLEON space observatory”, JETP Lett. **108**, 5–12 (2018).

[26] J. C. Arteaga-Velázquez, et. al., [HAWC], “Analysis of the composition of TeV cosmic rays with HAWC”, in Proceedings of 38th International Cosmic Ray Conference — PoS(ICRC2023), Vol. 444 (2023), p. 299.

[27] Y. S. Yoon, et. al., [CREAM-III], “Proton and helium spectra from the CREAM-III flight”, Astrophys. J. **839**, 5 (2017).

[28] Q. An, et al., [DAMPE], “Measurement of the cosmic ray proton spectrum from 40 GeV to 100 TeV with the DAMPE satellite”, Sci. Adv. **5**, eaax3793 (2019).

[29] F. Alemanno et al., [DAMPE], “Measurement of the cosmic ray helium energy spectrum from 70 GeV to 80 TeV with the DAMPE space mission”, Phys. Rev. Lett. **126**, 201102 (2021).

[30] O. Adriani, et al., [CALET], “Direct measurement of the cosmic-ray proton spectrum from 50 GeV to 10 TeV with the calorimetric electron telescope on the International Space Station”, Phys. Rev. Lett. **122**, 181102 (2019).

[31] O. Adriani, et al., [CALET], “Direct Measurement of the Cosmic-Ray Helium Spectrum from 40 GeV to 250 TeV with the Calorimetric Electron Telescope on the International Space Station”, Phys. Rev. Lett. **130**, 171002 (2023).

[32] S. Mollerach and E. Roulet, “Progress in high-energy cosmic ray physics”, Prog. Part. Nucl. Phys. **98**, 85–118 (2018).

[33] W. Baade and F. Zwicky, “Cosmic rays from super-novae”, Proceedings of the National Academy of Sciences **20**, 259–263 (1934).

[34] G. Morlino, “High-energy cosmic rays from supernovae”, in *Handbook of supernovae*, edited by A. W. Alsabti and P. Murdin (Springer International Publishing, Cham, 2017), pp. 1711–1736.

[35] W. Axford, E. Leer, and G. Skadron, “The acceleration of cosmic rays by shock waves”, in International cosmic ray conference, Vol. 11 (Springer, 1977).

[36] G. F. Krymsky, “Regular mechanism of charged particle acceleration on the shock wave front”, in Dokl. akad. nauk, Vol. 234, 6 (Russ. Acad. Sci., 1977), pp. 1306–1308.

[37] A. R. Bell, “The acceleration of cosmic rays in shock fronts–I”, Mon. Not. R. Astron. Soc. **182**, 147–156 (1978).

[38] R. D. Blandford and J. P. Ostriker, “Particle acceleration by astrophysical shocks”, Astrophys. J. **221**, L29–L32 (1978).

[39] C. J. Cesarsky, “Cosmic-ray confinement in the galaxy”, Annu. Rev. Nucl. Part. Sci. **18**, 289–319 (1980).

[40] V. S. Ptuskin et al., “Diffusion and drift of very high energy cosmic rays in galactic magnetic fields”, Astron. Astrophys. **268**, 726–735 (1993).

[41] A. W. Strong, I. V. Moskalenko, and V. S. Ptuskin, “Cosmic-ray propagation and interactions in the galaxy”, Annu. Rev. Nucl. Part. Sci. **57**, 285–327 (2007).

[42] V. Ptuskin, V. Zirakashvili, and E.-S. Seo, “Spectra of cosmic-ray protons and helium produced in supernova remnants”, Astrophys. J. **763**, 47 (2013).

[43] M. A. Malkov and I. V. Moskalenko, “The TeV Cosmic-Ray Bump: A Message from the Epsilon Indi or Epsilon Eridani Star?”, Astrophys. J. **911**, 151 (2021).

[44] M. A. Malkov and I. V. Moskalenko, “On the origin of observed cosmic-ray spectrum below 100 TV”, Astrophys. J. **933**, 78 (2022).

[45] W. Liu, Y.-Q. Guo, and Q. Yuan, “Indication of nearby source signatures of cosmic rays from energy spectra and anisotropies”, J. Cosmol. Astropart. Phys. **2019**, 010 (2019).

[46] V. Zatsepin and N. Sokolskaya, “Energy spectra of the main groups of galactic cosmic rays in the model of three classes of sources”, Astro. Lett. **33**, 25–33 (2007).

[47] [. C. Yue et al., “Implications on the origin of cosmic rays in light of 10 TeV spectral softenings”, Front. Phys. **15**, 1–9 (2020).

[48] S. Ostapchenko, “Monte Carlo treatment of hadronic interactions in enhanced Pomeron scheme: QGSJET-II model”, Phys. Rev. D **83**, 014018 (2011).

[49] A. U. Abeysekara, et al., [HAWC], “Measurement of the Crab Nebula spectrum past 100 TeV with HAWC”, Astrophys. J. **881**, 134 (2019).

[50] G. D’Agostini, “A multidimensional unfolding method based on Bayes’ theorem”, Nucl. Instrum. Methods Phys. Res. Sect. A **362**, 487–498 (1995).

[51] W. H. Richardson, “Bayesian-based iterative method of image restoration”, JoSA **62**, 55–59 (1972).

[52] L. B. Lucy, “An iterative technique for the rectification of observed distributions”, The Astronomical Journal **79**, 745 (1974).

[53] V. F. Hess, “Über Beobachtungen der durchdringenden Strahlung bei sieben Freiballonfahrten”, Phys. Z. **13**, 1084–1091 (1912).

[54] C. A. de Coulomb, Mem. de l’Acad. des Sciences, 612 (1875).

[55] C. V. Boys, “Quartz as an insulator”, Proceedings of the Physical Society of London **10**, 128 (1888).

[56] M. Bertolotti, *Celestial messengers* (Springer Berlin Heidelberg, 2013).

[57] H. Becquerel, “Sur les radiations émises par phosphorescence”, Comptes rendus de 1’Academie des Sciences, Paris **122**, 420–421 (1896).

[58] R. G. A. Fricke and K. Schlegel, “Julius Elster and Hans Geitel – Dioscuri of physics and pioneer investigators in atmospheric electricity”, History of Geo- and Space Sciences **8**, 1–7 (2017).

[59] Walther Gerlach, *Ebert, Hermann*, in: Neue Deutsche Biographie 4 (1959), S. 256-257 [Online-Version], `https://www.deutsche-biographie.de/pnd116332247.html`.

[60] A. Eve, “XIV. The ionization of the atmosphere over the ocean”, The London, Edinburgh, and Dublin Philosophical Magazine and Journal of Science **13**, 248–258 (1907).

[61] E. Rutherford, “Uranium radiation and the electrical conduction produced by it”, in *The collected papers of lord rutherford of nelson* (Routledge, 2014), pp. 169–215.

[62] P. Villard, “Sur la réflexion et la réfraction de rayons cathodiques et des rayons déviables du radium”, Comptes rendus **130**, 1010–1011 (1900).

[63] M. Walter, “Early cosmic ray research with balloons”, Nuclear Physics B - Proceedings Supplements **239-240**, Proceedings of the 9th workshop on Science with the New Generation of High Energy Gamma-ray Experiments: From high energy gamma sources to cosmic rays, one century after their discovery, 11–18 (2013).

[64] J. R. Hörandel, “Early cosmic-ray work published in German”, AIP Conference Proceedings **1516**, 52–60 (2013).

[65] A. Gockel and T. Wulf, “Beobachtungen über die radioaktivität der atmosphäre im hochgebirge”, Phys. Z **9**, 907–911 (1908).

[66] *Wikimedia commons*, Original Wulf electroscope used by Wulf around 1912. By A. De Angelis and C. Guaita, from the collection of R. Fricke., (2020) `https://commons.wikimedia.org/wiki/File:Originalwulf.jpeg`.

[67] F. Linke, “Luftelektrische messungen bei zwölf ballonfahrten.”, Abhandlungen der Gesellschaft der Wissenschaften in Göttingen, Mathematisch-Physikalische Klasse **3**, 1–1 (1904).

[68] J. Lacki, “Albert Gockel, a pioneer in atmospheric electricity and cosmic radiation”, Astroparticle Physics **53**, 27–32 (2014).

[69] A. Gockel, “Luftelektrische beobachtungen bei einer ballonfahrt”, Physikalische Zeitschrift **11**, 280–282 (1910).

[70] A. De Angelis, “Domenico Pacini, uncredited pioneer of the discovery of cosmic rays”, La Rivista del Nuovo Cimento **33**, 713–756 (2010).

[71] D. Pacini, “La radiazione penetrante alla superficie ed in seno alle acque”, Il Nuovo Cimento (1911-1923) **3**, 93–100 (1912).

[72] V. F. Hess, Phys. Zeit. **13** (1912).

[73] V. F. Hess, “Über Beobachtungen der durchdringenden Strahlung bei sieben Freiballonfahrten”, Physikalische Zeitschrift **13**, 1084–1091 (1912).

[74] M. Kachelrieß, “Lecture notes on high energy cosmic rays”, 17.th Jyväsklyä Summer School (2007).

[75] P. Biermann and G. Sigl, “Introduction to Cosmic Rays”, **576**, 1–26 (2002).

[76] The New York Times, (2012) `https://www.nytimes.com/2012/08/07/science/space/when-victor-hess-discovered-cosmic-rays-in-a-hydrogen-balloon.html`.

[77] W. Kolhörster, “Messungen der durchdringenden Strahlungen bis in Höhen von 9300”, Verh. deutsche phys. Gesellschaf, 719–721 (1914).

[78] R. A. Millikan and G. H. Cameron, Phys. Rev. **28**, 856 (1926).

[79] R. A. Millikan and G. H. Cameron, “The origin of the cosmic rays”, Phys. Rev. **32**, 533–557 (1928).

[80] D. Skobelzyn, “Die Intensitätsverteilung in dem Spektrum der γ-Strahlen von Ra C”, Zeitschrift für Physik **43**, 354–378 (1927).

[81] D. Skobelzyn, “Über eine neue art sehr schneller β-strahlen”, Zeitschrift für Physik **54**, 686–702 (1929).

[82] W. Bothe and W. Kolhörster, “Das wesen der höhenstrahlung”, Zeitschrift für Physik **56**, 751–777 (1929).

[83] L. Bonolis, “From cosmic ray physics to cosmic ray astronomy: Bruno Rossi and the opening of new windows on the universe”, Astroparticle Physics **53**, 67–85 (2014).

[84] L. Alvarez and A. H. Compton, “A positively charged component of cosmic rays”, Phys. Rev. **43**, 835–836 (1933).

[85] T. H. Johnson, “The azimuthal asymmetry of the cosmic radiation”, Phys. Rev. **43**, 834–835 (1933).

[86] M. F. L’Annunziata, *Radioactivity: introduction and history*, edited by M. F. L’Annunziata (Elsevier Science B.V., Amsterdam, 2007).

[87] B. Rossi, “EARLY DAYS IN COSMIC RAYS”, Phys. Today **34**, 34–41 (1981).

[88] W. Kolhörster, I. Matthes, and E. Weber, “Gekoppelte höhenstrahlen”, Naturwissenschaften **26**, 576–576 (1938).

[89] P. Auger, R. Maze, and T. Grivet-Meyer, “Grandes gerbes cosmiques atmosphèriques contenant des corpuscules ultrapènetrants”, Comptes Rendus de l’Acad’emie des Sciences **206**, 1721–1723 (1938).

[90] A. Abeysekara, et al., [HAWC], “HAWC observations of the acceleration of very-high-energy cosmic rays in the Cygnus Cocoon”, Nat Astron **5**, 465–471 (2021).

[91] LHAASO Collaboration, “An ultrahigh-energy γ-ray bubble powered by a super PeVatron”, Science Bulletin **69**, 449–457 (2024).

[92] M. Walter and A. W. Wolfendale, “Early history of cosmic particle physics”, The European Physical Journal H **37**, 323–358 (2012).

[93] V. Cirkel-bartelt, “History of Astroparticle Physics and its Components Imprint / Terms of Use”, Living Reviews in Relativity (2008).

[94] S. Abdollahi, et al., [Fermi-LAT], “Fermi Large Area Telescope Fourth Source Catalog”, The Astrophysical Journal Supplement Series **247**, 33 (2020).

[95] P. K. F. Grieder, *Extensive Air Showers*, Vol. 1 (Springer-Verlag Berlin Heidelberg, 2010), p. 1118.

[96] C. Grupen, *Astroparticle physics*, Vol. 1 (Springer-Verlag Berlin Heidelberg, 2005).

[97] G. M. Tanco, “Ultra-high energy cosmic rays: from GeV to ZeV”, in *Solar, stellar and galactic connections between particle physics and astrophysics* (Springer, 2007), pp. 165–196.

[98] W. Baade and F. Zwicky, “Cosmic Rays from Super-Novae”, Proceedings of the National Academy of Sciences **20**, 259 (1934).

[99] A. Bell, “Cosmic ray acceleration”, Astroparticle Physics **43**, Seeing the High-Energy Universe with the Cherenkov Telescope Array - The Science Explored with the CTA, 56–70 (2013).

[100] J. Abraham, et al., [Pierre Auger], “Correlation of the Highest-Energy Cosmic Rays with Nearby Extragalactic Objects”, Science **318**, 938–943 (2007).

[101] M. Aartsen, et al., [IceCube], “Neutrino emission from the direction of the blazar TXS 0506+056 prior to the IceCube-170922A alert”, Science **361**, 147–151 (2018).

[102] Particle Data Group, C. Patrignani, et al., “Review of Particle Physics”, Chinese Physics C **40**, 10001 (2016).

[103] G. Kulikov and G. B. Khristiansen, “On the size spectrum of extensive air showers”, Sov. Phys. JETP **35**, 441–444 (1959).

[104] M. Bertaina, et al., [KASCADE-Grande], “The cosmic ray energy spectrum in the range 10^{16}–10^{18} eV measured by KASCADE-Grande”, Astrophys. Space Sci. Trans. **7**, 229–234 (2011).

[105] D. R. Bergman and J. W. Belz, “Cosmic rays: the second knee and beyond”, Journal of Physics G: Nuclear and Particle Physics **34**, R359–R400 (2007).

[106] D.-Y. Chung, “The knees-ankles-toe in cosmic rays and the periodic table of elementary particles”, Journal of Modern Physics **5**, 1467–1472 (2014).

[107] M. E. Bertaina, “Cosmic rays from the knee to the ankle”, Comptes Rendus Physique **15**, Ultra-high-energy cosmic rays: From the ankle to the tip of the spectrum, 300–308 (2014).

[108] S. Thoudam et al., “Cosmic-ray energy spectrum and composition up to the ankle - the case for a second Galactic component”, Astronomy & Astrophysics **595**, 23 (2016).

[109] T. Antoni, et al., [KASCADE], “KASCADE measurements of energy spectra for elemental groups of cosmic rays: Results and open problems”, Astropart. Phys. **24**, 1–25 (2005).

[110] W.D. Apel, et al., [KASCADE], “Energy spectra of elemental groups of cosmic rays: Update on the KASCADE unfolding analysis”, Astropart. Phys. **31**, 86–91 (2009).

[111] W. D. Apel, et al., [KASCADE-Grande], “KASCADE-Grande measurements of energy spectra for elemental groups of cosmic rays”, Astropart. Phys. **47**, 54–66 (2013).

[112] M. Aglietta, et al., [EAS-TOP], "The cosmic ray primary composition in the "knee" region through the EAS electromagnetic and muon measurements at EAS-TOP", Astroparticle Physics **21**, 583–596 (2004).

[113] A.P. Garyaka, et al., [GAMMA], "Rigidity-dependent cosmic ray energy spectra in the knee region obtained with the GAMMA experiment", Astroparticle Physics **28**, 169–181 (2007).

[114] Z. Cao, et. al., [LHAASO], "Measurements of All-Particle Energy Spectrum and Mean Logarithmic Mass of Cosmic Rays from 0.3 to 30 PeV with LHAASO-KM2A", Phys. Rev. Lett. **132**, 131002 (2024).

[115] V. Souza, et al., [KASCADE-Grande], "The KASCADE-grande experiment", AIP Conference Proceedings **1123**, 211–216 (2009).

[116] W. D Apel et al., "Kneelike Structure in the Spectrum of the Heavy Component of Cosmic Rays Observed with KASCADE-Grande", Phys. Rev. Lett. **107**, 171104 (2011).

[117] J. C. Arteaga-Velázquez, et al., [KASCADE-Grande], "The KASCADE-Grande experiment: measurements of the all-particle energy spectrum of cosmic rays", XVI International Symposium on Very High Energy Cosmic Ray Interactions ISVHECRI 2010.

[118] Helmholtz Allience for Astroparticle Physics, (2017) `http://www.hap-astroparticle.org/184.php`.

[119] M. Bustamante et al., "High-energy cosmic-ray acceleration", 2009 CERN-Latin-American School of High-Energy Physics, CLASHEP 2009 - Proceedings, 533–539 (2010).

[120] H. S. Ahn et al., "Discrepant Hardening Observed in Cosmic-ray Elemental Spectra", The Astrophysical Journal Letters **714**, L89 (2010).

[121] O. Adriani, et al., [PAMELA], "PAMELA Measurements of Cosmic-Ray Proton and Helium Spectra", Science **332**, 69–72 (2011).

[122] AMS Collaboration, "The Alpha Magnetic Spectrometer (AMS) on the International Space Station", Physics Reports **366**, 331–404 (2002).

[123] A. Abdul Halim, et al., [Pierre Auger], "Inference of the mass composition of cosmic rays with energies from $10^{18.5}$ to 10^{20} eV using the Pierre Auger observatory and deep learning", Phys. Rev. Lett. **134**, 021001 (2025).

[124] J. C. Arteaga-Velázquez, et al., [HAWC], "Cosmic ray spectrum of protons plus helium nuclei between 6 and 158 TeV from HAWC data", Phys. Rev. D **105**, 063021 (2022).

[125] N. Tomassetti, "Direct measurements of galactic cosmic rays", arXiv preprint arXiv:2301.10255 (2023).

[126] S. G. Mashnik, "On solar system and cosmic rays nucleosynthesis and spallation processes", Los Alamos National Laboratory Report LA-UR-00-3658 (2000).

[127] G. Steigman, "Observational tests of antimatter cosmologies", In: Annual review of astronomy and astrophysics. Volume 14.(A76-46826 24-90) Palo Alto, Calif., Annual Reviews, Inc., 1976, p. 339-372. **14**, 339–372 (1976).

[128] M. Aguilar, et al., [AMS], "Towards understanding the origin of cosmic-ray positrons", Phys. Rev. Lett. **122**, 041102 (2019).

[129] L. Canetti, M. Drewes, and M. Shaposhnikov, "Matter and antimatter in the universe", New Journal of Physics **14**, 095012 (2012).

[130] A. Bykov et al., “Antistars as possible sources of antihelium cosmic rays”, Journal of Cosmology and Astroparticle Physics **2023**, 027 (2023).

[131] P. De La Torre Luque, M. W. Winkler, and T. Linden, “Cosmic-ray propagation models elucidate the prospects for antinuclei detection”, arXiv e-prints, arXiv–2404 (2024).

[132] M. W. Winkler, P. D. L. T. Luque, and T. Linden, “Cosmic ray antihelium from a strongly coupled dark sector”, Phys. Rev. D **107**, 123035 (2023).

[133] J. Alcaraz et al., “Search for antihelium in cosmic rays”, Physics Letters B **461**, 387–396 (1999).

[134] P. Von Doetinchem et al., “Cosmic-ray antinuclei as messengers of new physics: status and outlook for the new decade”, Journal of Cosmology and Astroparticle Physics **2020**, 035 (2020).

[135] M. Aguilar, et al., [AMS], “The Alpha Magnetic Spectrometer (AMS) on the international space station: Part II—Results from the first seven years”, Physics reports **894**, 1–116 (2021).

[136] K. Lave et al., “Galactic cosmic-ray energy spectra and composition during the 2009–2010 solar minimum period”, Astrophys. J. **770**, 117 (2013).

[137] R. P. Murphy, et al., [SUPERTIGER], “Galactic cosmic ray origins and OB associations: evidence from SuperTIGER observations of elements 26Fe through 40Zr”, Astrophys. J. **831**, 148 (2016).

[138] A. Aab, et al., [Pierre Auger], “Observation of a large-scale anisotropy in the arrival directions of cosmic rays above 8×10^{18} eV”, Science **357**, 1266–1270 (2017).

[139] A. Aab, et al., [Pierre Auger], “Large-scale Cosmic-Ray Anisotropies above 4 EeV Measured by the Pierre Auger Observatory”, The Astrophysical Journal **868**, 4 (2018).

[140] S. Mollerach and E. Roulet, “Progress in high-energy cosmic ray physics”, Progress in Particle and Nuclear Physics **98**, 85–118 (2018).

[141] M. Kachelriess and D. Semikoz, “Cosmic ray models”, Progress in Particle and Nuclear Physics **109**, 103710 (2019).

[142] A. Albert, et al., [HAWC], “Observation of the Galactic Center PeVatron beyond 100 TeV with HAWC”, Astrophys. J. Lett. **973**, L34 (2024).

[143] R. Alfaro, et al., [HAWC], “Ultra-high-energy gamma-ray bubble around microquasar V4641 Sgr”, Nature **634**, 557 (2024).

[144] A. Abdul Halim, et al., [Pierre Auger], “Constraining models for the origin of ultra-high-energy cosmic rays with a novel combined analysis of arrival directions, spectrum, and composition data measured at the Pierre Auger Observatory”, Journal of Cosmology and Astroparticle Physics **2024**, 022 (2024).

[145] G. Pelletier and E. Kersalé, “Acceleration of UHE Cosmic Rays in Gamma-Ray Bursts”, Astronomy and Astrophysics **361** (2000).

[146] IceCube, Fermi-LAT, MAGIC, AGILE, ASAS-SN, HAWC, H.E.S.S., INTEGRAL, KANATA, KISO, KAPTEYN, LIVERPOOL TELESCOPE, SUBARU, SWIFT/NUSTAR, VERITAS, VLA/17B-403 teams, “Multimessenger observations of a flaring blazar coincident with high-energy neutrino IceCube-170922A”, Science **361**, `10.1126/science.aat1378` (2018).

[147] E. Fermi, “On the origin of the cosmic radiation”, Phys. Rev. **75**, 1169–1174 (1949).

[148] M. S. Longair, *High Energy Astrophysics* (2011), p. 880.

[149] G. Morlino, "High Energy Cosmic Rays From Supernovae", 1–25.

[150] B. Dawson, "Ultra-High Energy Cosmic Rays Ultra-High Energy Cosmic Rays", **35**, 1845–1861 (2009).

[151] B. Peters, "Primary cosmic radiation and extensive air showers", Il Nuovo Cimento (1955-1965) **22**, 800–819 (1961).

[152] A. M. Hillas, "The Origin of Ultra-High-Energy Cosmic Rays", Annual Review of Astronomy and Astrophysics **22**, 425–444 (1984).

[153] L. A. Anchordoqui, "Ultra-high-energy cosmic rays", Phys. Rept. **801**, 1–93 (2019).

[154] T. K. Gaisser, "Spectrum of cosmic-ray nucleons, kaon production, and the atmospheric muon charge ratio", Astroparticle Physics **35**, 801–806 (2012).

[155] O. Adriani et al., "Observation of spectral structures in the flux of cosmic-ray protons from 50 GeV to 60 TeV with the Calorimetric Electron Telescope on the International Space Station", Phys. Rev. Lett. **129**, 101102 (2022).

[156] O. Adriani, et al., [CALET], "Direct Measurement of the Spectral Structure of Cosmic-Ray Electrons + Positrons in the TeV Region with CALET on the International Space Station", Phys. Rev. Lett. **131**, 191001 (2023).

[157] V. Savchenko, M. Kachelrieß, and D. Semikoz, "Imprint of a 2 million year old source on the cosmic-ray anisotropy", Astrophys. J. Lett. **809**, L23 (2015).

[158] M. Kachelrieß, A. Neronov, and D. Semikoz, "Signatures of a two million year old supernova in the spectra of cosmic ray protons, antiprotons, and positrons", Phys. Rev. Lett. **115**, 181103 (2015).

[159] T. A. Porter, G. Johannesson, and I. V. Moskalenko, "The GALPROP cosmic-ray propagation and nonthermal emissions framework: Release v57", The Astrophysical Journal Supplement Series **262**, 30 (2022).

[160] B. Rossi, "Misure sulla distribuzione angolare di intensita della radiazione penetrante all'Asmara", La Ricerca Scientifica Supplemento **1**, Cited By :1, 579–589 (1934).

[161] R. Engel, D. Heck, and T. Pierog, "Extensive air showers and hadronic interactions at high energy", Annu. Rev. Nucl. Part. Sci. **61**, 467–489 (2011).

[162] J.J. Beatty, "Cosmic Rays", in K. Nakamura, et al., [PDG], "Review of Particle Physics", J. Phys. G: Nucl. Part. Phys. 37 075021 (2010).

[163] J. Alvarez-Muñiz, "Cosmic Rays", in S. Navas, et al., [PDG], "Review of Particle Physics", Phys. Rev. D 110, 030001 (2024).

[164] X. Tian et al., "Approach for composition measurement of cosmic rays using the muon-to-electron ratio observed by LHAASO-KM2A", Phys. Rev. D **110**, 043030 (2024).

[165] S. P. Knurenko and I. S. Petrov, "Mass composition of cosmic rays determined by the muon fraction with $\epsilon_{\text{thr}} \geq 1$ GeV in air showers with energy greater than 5 eev", Phys. Rev. D **102**, 023036 (2020).

[166] A. Balagopal V., et al., [ICECUBE], "Discrimination of Muons for Mass Composition Studies of Inclined Air Showers Detected with IceTop", in Proceedings of 37th international cosmic ray conference — pos(icrc2021), Vol. 395 (2021), p. 212.

[167] K. Kamata and J. Nishimura, "The lateral and the angular structure functions of electron showers", Progress of Theoretical Physics Supplement **6**, 93–155 (1958).

[168] A. Basak and R. K. Dey, "The shape of the electron and muon lateral distribution functions of extensive air showers", The European Physical Journal Plus **138**, 992 (2023).

[169] T. Stanev, *High energy cosmic rays* (Springer Science & Business Media, 2010).

[170] J. Abraham, et al., [Pierre Auger], "Measurement of the depth of maximum of extensive air showers above 10^{18} eV", Phys. Rev. Lett. **104**, 091101 (2010).

[171] H. H. Kh., "A new model-independent approach for finding the arrival direction of an extensive air shower", Journal of Cosmology and Astroparticle Physics **2016**, 040 (2016).

[172] P. Lipari, "Concepts of "age" and "universality" in cosmic ray showers", Phys. Rev. D **79**, 063001 (2009).

[173] K. Greisen, "Cosmic ray showers", Annual Review of Nuclear Science **10**, 63–108 (1960).

[174] A. De Angelis, O. Mansutti, and M. Persic, "Very-high energy gamma astrophysics", arXiv preprint arXiv:0712.0315 (2007).

[175] W. Heitler, *The quantum theory of radiation* (Oxford University Press, 1954).

[176] T. Pierog, R. Engel, and D. Heck, "Impact of uncertainties in hadron production on air-shower predictions", Czechoslovak Journal of Physics **56**, 1–12 (2006).

[177] J. Matthews, "A Heitler model of extensive air showers", Astropart. Phys. **22**, 387–397 (2005).

[178] [. K. Aamodt et al., "First proton-proton collisions at the LHC as observed with the ALICE detector: measurement of the charged-particle pseudorapidity density at $\sqrt{s}$=900 GeV", The European Physical Journal C **65**, 111–125 (2010).

[179] K. Carvalho-Akiba, et al., [LHCb] (LHCb), "First LHCb Results from 2009 LHC Run", (2010).

[180] V. Khachatryan, et al., [CMS], "CMS tracking performance results from early LHC operation", The European Physical Journal C **70**, 1165–1192 (2010).

[181] T. Pierog, "Hadronic interactions and air showers: Where do we stand?", in Epj web of conferences, Vol. 208 (EDP Sciences, 2019), p. 02002.

[182] L. Calcagni, C. G. Canal, S. J. Sciutto, and T. Tarutina, "LHC updated hadronic interaction packages analyzed up to cosmic-ray energies", Phys. Rev. D **98**, 083003 (2018).

[183] P. Schleper, "Soft hadronic interactions", in 30th International Conference on High-Energy Physics (July 2000), pp. 237–250.

[184] J. F. Donoghue, "Final state interactions in the decays of heavy quarks", arXiv preprint hep-ph/9607352 (1996).

[185] L. V. Gribov, E. M. Levin, and M. G. Ryskin, "Semihard processes in QCD", Physics Reports **100**, 1–150 (1983).

[186] T. Pierog, J. M. Katzy, E. Yatsenko, and K. Werner, "EPOS LHC: test of collective hadronization with LHC data", arXiv:1306.0121v2 [hep-ph].

[187] S. Ostapchenko and D. Heck, "Hadronic Interactions in QGSJET-II : Physics and Results", 29th International Cosmic Ray International COnference, 135–138 (2005).

[188] F. Riehn and T. K. Gaisser, "A new version of the event generator Sibyll", (2015).

[189] J. Ranft, "DPMJET version II.5, code manual", (2008).

[190] A. C. ENE, A. JIPA, and L.-E. GIUBEGA, "Study of monte carlo event generators for proton-proton collisions at lhc energies in the forward region *", Chinese Physics C **43**, 083001 (2019).

[191] T. Pierog, "Air Shower Simulation with a New Generation of post-LHC Hadronic Interaction Models in CORSIKA", in Proceedings of 35th international cosmic ray conference — pos(icrc2017), Vol. 301 (2017), p. 1100.

[192] S. Ostapchenko, "LHC results and hadronic interaction models", in 25th European Cosmic Ray Symposium (Dec. 2016).

[193] T. Pierog et al., "EPOS LHC: Test of collective hadronization with data measured at the CERN Large Hadron Collider", Phys. Rev. C **92**, 034906 (2015).

[194] J. Albrecht et al., "The muon puzzle in cosmic-ray induced air showers and its connection to the large hadron collider", Astrophysics and Space Science **367**, 27 (2022).

[195] E.-J. Ahn et al., "Cosmic ray interaction event generator SIBYLL 2.1", Phys. Rev. D **80**, 094003 (2009).

[196] T. Pierog, M. Perlin, and K. Werner, "Hadronic Interactions Studies at the LHC", EPJ Web Conf. **283**, 05001 (2023).

[197] K.-H. Kampert and A. A. Watson, "Extensive air showers and ultra high-energy cosmic rays: a historical review", The European Physical Journal H **37**, 359–412 (2012).

[198] V. Cirkel-Bartelt, "History of astroparticle physics and its components", Living reviews in relativity **11**, 1–58 (2008).

[199] W. R. Leo, *Techniques for nuclear and particle physics experiments: a how-to approach* (Springer Science & Business Media, 2012).

[200] R. J. Wilkes, "Technology of small emulsion chambers: a new review", AIP Conference Proceedings **49**, 63–71 (1979).

[201] A. D. Panov, et al., [ATIC], "The energy spectra of heavy nuclei measured by the ATIC experiment", Advances in Space Research **37**, 1944–1949 (2006).

[202] A. D. Panov et al., "Energy spectra of abundant nuclei of primary cosmic rays from the data of ATIC-2 experiment: Final results", Bull. Russ. Acad. Sci. Phys. **73**, 564–567 (2009).

[203] T. Maeno, et al., [BESS], "Successive measurements of cosmic-ray antiproton spectrum in a positive phase of the solar cycle", Astroparticle Physics **16**, 121–128 (2001).

[204] P. S. Marrocchesi, et al., [CALET], "CALET: A calorimeter-based orbital observatory for High Energy Astroparticle Physics For the CALET Collaboration", Nucl. Instrum. Methods Phys. Res. Sect. A **692**, 240–245 (2014).

[205] H. S. Ahn et al., "Energy Spectra of Cosmic-Ray Nuclei At High Energies", The Astrophysical Journal **707**, 593–603 (2009).

[206] M. Bertaina et al., "The cosmic ray primary spectrum in the transition region between direct and indirect measurements (10 TeV - 10 PeV)", Journal of Physics: Conference Series **120**, 62023 (2008).

[207] B. Keilhauer et al., "Nitrogen fluorescence in air for observing extensive air showers", EPJ Web Conf. **53**, 01010 (2013).

[208] P. Sokolsky, et al., [HiRes], "Final Results from the High solution Fly's Eye (HiRes) Experiment", Nuclear Physics B - Proceedings Supplements **212-213**, 74–78 (2011).

[209] F. Aharonian, et al., [HESS], “The HESS survey of the inner galaxy in very high energy gamma rays”, Astrophys. J. **636**, 777 (2006).

[210] F. Aharonian, et al., [H.E.S.S.], “First ground-based measurement of atmospheric Cherenkov light from cosmic rays”, Phys. Rev. D **75**, 042004 (2007).

[211] F. Aharonian, et al., [H.E.S.S.], “Probing the ATIC peak in the cosmic-ray electron spectrum with H.E.S.S.”, Astron. & Astrophys. **508**, 561–564 (2009).

[212] A. Archer, et al., [VERITAS], “Measurement of cosmic-ray electrons at TeV energies by VERITAS”, Phys. Rev. D **98**, 062004 (2018).

[213] A. Archer, et al., [VERITAS], “Measurement of the iron spectrum in cosmic rays by VERITAS”, Phys. Rev. D **98**, 022009 (2018).

[214] M. L. Ahnen, et al., [MAGIC], “Performance of the MAGIC telescopes under moonlight”, Astropart. Phys. **94**, 29–41 (2017).

[215] I. Reichardt, et al., [MAGIC], “Cosmic Ray Acceleration in W51C Observed with the MAGIC Telescopes”, Astrophys. Space Sci. Proc. **34**, edited by D. F. Torres and O. Reimer, 211–219 (2013).

[216] [. B. S. Acharya et al., “Science with the cherenkov telescope array”, arXiv: 1709.07997 (2017).

[217] A. U. Abeysekara, et al., [HAWC], “The High-Altitude Water Cherenkov (HAWC) observatory in México: The primary detector”, Nucl. Instrum. Methods Phys. Res. Sect. A **1052**, 168253 (2023).

[218] M. G. Aartsen, et al., [IceCube], “Cosmic Ray Spectrum and Composition from PeV to EeV Using 3 Years of Data From IceTop and IceCube”, Phys. Rev. D **100**, 082002 (2019).

[219] Z. Cao, et al., [LHAASO], “The Large High Altitude Air Shower Observatory (LHAASO) Science Book (2021 Edition)”, arXiv:1905.02773v4 [astro-ph.HE], `https://doi.org/10.48550/arXiv.1905.02773` (2019).

[220] F. G. Schröder, “Radio detection of cosmic-ray air showers and high-energy neutrinos”, Progress in Particle and Nuclear Physics **93**, 1–68 (2017).

[221] A. Abdul Halim, et al., [Pierre Auger], “Demonstrating Agreement between Radio and Fluorescence Measurements of the Depth of Maximum of Extensive Air Showers at the Pierre Auger Observatory”, Phys. Rev. Lett. **132**, 021001 (2024).

[222] F. G. Schröder, “Radio detection of cosmic-ray air showers and high-energy neutrinos”, Progress in Particle and Nuclear Physics **93**, 1 (2017).

[223] L. Kuzmichev, et al., [TAIGA], “Tunka Advanced Instrument for cosmic rays and Gamma Astronomy (TAIGA): Status, results and perspectives”, EPJ Web of Conferences **145**, 01001 (2017).

[224] J. Petrovic, et al., [LOPES], “Radio emission of highly inclined cosmic ray air showers measured with LOPES”, Astronomy & Astrophysics **462**, 389–395 (2007).

[225] M. P. van Haarlem et al., “LOFAR: The low-frequency array”, Astronomy and Astrophysics, `10.1051/0004-6361/201220873` (2013).

[226] T.G. Guzik, et al., [ATIC], “Enhancing the ATIC charge resolution”, Advances in Space Research **42**, 424–430 (2008).

[227] A. D. Panov, et al., [ATIC], “Possible structure in the cosmic ray electron spectrum measured by the ATIC-2 and ATIC-4 experiments”, Astrophys. Space Sci. Trans. **7**, 119–124 (2011).

[228] Fei Zhang, et al., [DAMPE], “Design of the readout electronics for the DAMPE Silicon Tracker detector”, Chinese Physics C **40**, 116101 (2016).

[229] J. Chang, et al., [DAMPE], “The Dark Matter Particle Explorer mission”, Astropart. Phys. **95**, 6–24 (2017).

[230] F. Alemanno et al., [DAMPE], “Measurement of the cosmic $p +$ He energy spectrum from 50 GeV to 0.5 PeV with the DAMPE space mission”, Phys. Rev. D **109**, L121101 (2024).

[231] P. Ma, et al., [DAMPE], *The latest results from the DAMPE experiment [Conference presentation]*, 13th Cosmic-Ray International Studies and Multi-Messenger Astroparticle Conference, 2024.

[232] I. Cagnoli, et al., [DAMPE], “Galactic cosmic ray spectral measurements with the DAMPE space mission”, EPJ Web Conf. **319**, 02002 (2025).

[233] D. Podorozhnyi et al., “Advanced method of energy determination of cosmic ray nuclei, applicable in lightweight instruments for satellites.”, in Proceedings of the 27th International Cosmic Ray Conference. 07-15 August, 2001. Hamburg, Germany. Under the auspices of the International Union of Pure and Applied Physics (IUPAP)., p. 2267, Vol. 6 (2001), p. 2267.

[234] G. Marsella, et al., [ARGO-YBJ], “Physics and astronomy results with the ARGO-YBJ experiment”, Nucl. Phys. B **188**, Proceedings of the Neutrino Oscillation Workshop, 280–282 (2009).

[235] S.S. Zhang, et al., [ARGO-YBJ], “Properties and performance of two wide field of view Cherenkov/fluorescence telescope array prototypes”, Nucl. Instrum. Methods Phys. Res. Sect. A **629**, 57–65 (2011).

[236] B. Bartoli, et al., [ARGO-YBJ,LHAASO], “Knee of the cosmic hydrogen and helium spectrum below 1 pev measured by argo-ybj and a cherenkov telescope of lhaaso”, Phys. Rev. D **92**, 092005 (2015).

[237] G. Marsella, et al., [ARGO-YBJ], “The distributed RPC read-out system for the ARGO-YBJ experiment”, Proceedings of the 27th International Cosmic Ray Conference. 07-15 August, 2001. Hamburg, Germany. Under the auspices of the International Union of Pure and Applied Physics (IUPAP)., p.2883.

[238] B. Bartoli, et al., [ARGO-YBJ], “Cosmic ray proton plus helium energy spectrum measured by the ARGO-YBJ experiment in the energy range 3–300 TeV”, Phys. Rev. D **91**, 112017 (2015).

[239] Paolo Montini, et al., [ARGO-YBJ], “Cosmic ray physics with ARGO-YBJ”, Nuclear and particle physics proceedings **279**, 7–14 (2016).

[240] M.G. Aartsen, et al., [IceCube], “The IceCube Neutrino Observatory: instrumentation and online systems”, Journal of Instrumentation **12**, P03012 (2017).

[241] R. Abbasi, et al., [IceCube], “The IceCube data acquisition system: Signal capture, digitization, and timestamping”, Nucl. Instrum. Methods Phys. Res. Sect. A **601**, 294–316 (2009).

[242] R. Abbasi, et al., [IceCube], “IceTop: The surface component of IceCube”, Nucl. Instrum. Methods Phys. Res. Sect. A **700**, 188–220 (2013).

[243] The IceCube Collaboration, “Science Case of a Scintillator and Radio Surface Array at IceCube”, 36^{th} International Cosmic Ray Conference (2019).

[244] A. Rehman et al., “Search for Cosmic-Ray Events Using Radio Signals and CNNs in Data from the IceTop Enhancement Prototype Station”, in 38th international cosmic ray conference (icrc2023)-cosmic-ray physics (indirect, cri) (2023), p. 291.

[245] M. G. Aartsen, et al., [ICECUBE], “Cosmic ray spectrum from 250 TeV to 10 PeV using IceTop”, Phys. Rev. D **102**, 122001 (2020).

[246] R. Abbasi, et al., [IceCube], “Cosmic ray composition and energy spectrum from 1–30PeV using the 40-string configuration of IceTop and IceCube”, Astropart. Phys. **42**, 15–32 (2013).

[247] M. G. Aartsen, et al., [IceCube], “Cosmic ray spectrum and composition from PeV to EeV using 3 years of data from IceTop and IceCube”, Phys. Rev. D **100**, 082002 (2019).

[248] T. Antoni, et al., [KASCADE], “The cosmic-ray experiment KASCADE”, Nucl. Instrum. Methods Phys. Res. Sect. A **513**, 490–510 (2003).

[249] M. Ahlers, [KASCADE-Grande], “Large-and Medium-scale Anisotropies in the Arrival Directions of Cosmic Rays Observed with KASCADE-Grande”, Astrophys. J. Lett. **886**, L18 (2019).

[250] K.-H. Kampert et al., “Cosmic Ray Energy Spectra and Mass Composition at the Knee–Recent Results from KASCADE–”, Nuclear Physics B-Proceedings Supplements **136**, 273–281 (2004).

[251] Karlsruhe Institute of Technology, *KASCADE-Grande web site*, (2014) `http://www.ikp.kit.edu/kascade/english/index.php`.

[252] N. Budnev, et al., [TAIGA], “The TAIGA experiment: From cosmic-ray to gamma-ray astronomy in the Tunka valley”, Nucl. Instrum. Methods Phys. Res. Sect. A **845**, 330–333 (2017).

[253] N. Budnev, et al., [TAIGA], “Taiga—an advanced hybrid detector complex for astroparticle physics and high energy gamma-ray astronomy in the tunka valley”, Journal of Instrumentation **15**, C09031 (2020).

[254] N.M. Budnev, et al., [TAIGA], “The primary cosmic-ray energy spectrum measured with the Tunka-133 array”, Astropart. Phys. **117**, 102406 (2020).

[255] N.M. Budnev, et al., [TAIGA], “The TAIGA experiment: from cosmic ray physics to gamma astronomy in the Tunka valley”, Phys. Part. Nuclei **49**, 589–598 (2018).

[256] R. D. Monkhoev, et al., [TAIGA], “Main Results from the TUNKA-GRANDE Experiment”, Bull. Russ. Acad. Sci. Phys. **87**, 893–899 (2023).

[257] R. D. Monkhoev, et al., [TAIGA] (Tunka), “The Tunka-Grande experiment: Status and prospects”, Bull. Russ. Acad. Sci. **81**, 468–470 (2017).

[258] O. Gress, et al., [TAIGA], “The wide-aperture gamma-ray telescope TAIGA-HiSCORE in the Tunka Valley: Design, composition and commissioning”, Nucl. Instrum. Methods Phys. Res. Sect. A **845**, Proceedings of the Vienna Conference on Instrumentation 2016, 367–372 (2017).

[259] V. Prosin, et al., [TAIGA], “Energy Spectrum of Primary Cosmic Rays, According to TUNKA-133 and TAIGA-HiSCORE EAS Cherenkov Light Data”, Bull. Russ. Acad. Sci. Phys. **83**, 1016–1019 (2019).

[260] TAIGA collaboration, *”TAIGA | facility in the Tunka valley”*, (2025) `https://taiga-experiment.info/taiga-detector`.

[261] I. Astapov, et al., [TAIGA], “The TAIGA—a Hybrid Detector Complex in Tunka Valley for Astroparticle Physics, Cosmic Ray Physics and Gamma-Ray Astronomy”, Phys. Atom. Nucl. **86**, 471–477 (2023).

[262] Anna L. Ivanova, et al., [TAIGA], “The Tunka-Grande scintillation array: Current results”, SciPost Phys. Proc. **13**, 011 (2023).

[263] W. Prosin and the TAIGA collboration, “TUNKA-133: Results of 3 year operation”, Nucl. Instrum. Methods Phys. Res. Sect. A **756**, 94–101 (2014).

[264] M. Amenomori, et al., [TIBET], “First Detection of Photons with Energy beyond 100 TeV from an Astrophysical Source”, Phys. Rev. Lett. **123**, 051101 (2019).

[265] M. Amenomori, et al., [TIBET], “The All-Particle Spectrum of Primary Cosmic Rays in the Wide Energy Range from 10^{14} to 10^{17} eV Observed with the Tibet-III Air-Shower Array”, The Astrophysical Journal **678**, 1165–1179 (2008).

[266] M. Amenomori, et al., [TIBET], “Cosmic-ray energy spectrum around the knee observed with the Tibet air-shower experiment”, Astrophysics and Space Sciences Transactions **7**, 15–20 (2011).

[267] M. Amenomori, et al., [TIBET], “Chemical composition of cosmic rays around the knee observed by the Tibet air-shower-core detector”, J. Phys. Soc. Jpn. **78**, 206–209 (2009).

[268] M. Amenomori, et al., [TIBET], “Northern Sky Galactic Cosmic Ray Anisotropy between 10 and 1000 TeV with the Tibet Air Shower Array”, Astrophys. J. **836**, 153 (2017).

[269] M. Amenomori, et al., [TIBET], “Development and performance test of a prototype air shower array for search for gamma ray point sources in the very high energy region”, Nucl. Instrum. Methods Phys. Res. Sect. A **288**, 619–631 (1990).

[270] W. Liu et al., “Measurement of cosmic-ray anisotropies using LHAASO-WCDA”, in Proceedings of 38th international cosmic ray conference — pos(icrc2023), Vol. 444 (2023), p. 186.

[271] Q. Sun et al., “The end-to-end Calibration of LHAASO-WFCTA based on Nitrogen Laser System”, in Proceedings of 38th international cosmic ray conference — pos(icrc2023), Vol. 444 (2023), p. 494.

[272] Z. Cao, et al., [LHAASO], “Discovery of the ultrahigh-energy gamma-ray source LHAASO J2108+ 5157”, Astrophys. J. Lett. **919**, L22 (2021).

[273] X.-J. Lv et al., “Precise Measurement of the Cosmic-Ray Spectrum and <ln A> by LHAASO: Connecting the Galactic to the Extragalactic Components”, Astrophys. J. **979**, 225 (2025).

[274] Y. Takahashi, et al., [JACEE], “Elemental abundance of high energy cosmic rays”, Nuclear Physics B - Proceedings Supplements **60**, 83–92 (1998).

[275] I. P. Ivanenko, et al., [SOKOL], “Energy Spectra of Cosmic Rays above 2 TeV as Measured by the ’SOKOL’ Apparatus”, in 23rd International Cosmic Ray Conference, Vol. 2, held 19-30 July, 1993 at University of Calgary, Alberta, Canada. Edited by D.A. Leahy, R.B. Hicks, and D. Venkatesan. Invited, Rapporteur, and Highlight Papers. Singapore: World Scientific, 1993., p.17 (1993).

[276] M. Aglietta, et al., [EAS-TOP], “The EAS size spectrum and the cosmic ray energy spectrum in the region 10^{15}–10^{16} eV”, Astropart. Phys. **10**, 1–9 (1999).

[277] F. Arqueros et al., “Energy spectrum and chemical composition of cosmic rays between 0.3 and 10 pev determined from the cherenkov-light and charged-particle distributions in air showers”, Astronomy and Astrophysics, v. 359, p. 682-694 (2000) **359**, 682–694 (2000).

[278] R. Alfaro, et al., [HAWC], “A measurement of the all-particle energy spectrum of cosmic rays from 10^{13} to 10^{15} eV using HAWC”, Astropart. P. **167**, 103077 (2025).

[279] A.A. Abdo, et al., [MILAGRO], “Milagro observations of potential TeV emitters”, Astropart. Phys. **57-58**, 16–25 (2014).

[280] A. U. Abeysekara, et al., [HAWC], “Extended gamma-ray sources around pulsars constrain the origin of the positron flux at Earth”, Science **358**, 911–914 (2017).

[281] A. Albert, et al., [HAWC], “Precise Measurements of TeV Halos around Geminga and Monogem Pulsars with HAWC”, Astrophys. J **974**, 246 (2024).

[282] A. U. Abeysekara, et al., [HAWC], “Multiple galactic sources with emission above 56 TeV detected by HAWC”, Phys. Rev. Lett. **124**, 021102 (2020).

[283] A. Albert, et al., [HAWC], “Spectrum and morphology of the very-high-energy source hawc j2019+368”, Astrophys. J. **911**, 143 (2021).

[284] A. Albert, et al., [HAWC], “HAWC J2227+ 610 and its association with G106. 3+ 2.7, a new potential Galactic PeVatron”, Astrophys. J. Lett. **896**, L29 (2020).

[285] A. Albert, et al., [HAWC], “Performance of the HAWC Observatory and TeV gamma-ray measurements of the Crab Nebula with improved extensive air shower reconstruction algorithms”, Astrophys. J. **972**, 144 (2024).

[286] A. Albert, et al., [HAWC], “Discovery of Gamma Rays from the Quiescent Sun with HAWC”, Phys. Rev. Lett. **131**, 051201 (2023).

[287] A. U. Abeysekara, et al., [HAWC], “Very high energy particle acceleration powered by the jets of the microquasar SS 433”, Nature **564**, E38 (2018).

[288] A. Abeysekara, et al., [HAWC], “Daily Monitoring of TeV Gamma-Ray Emission from Mrk 421, Mrk 501, and the Crab Nebula with HAWC”, Astrophys. J. **841**, 100 (2017).

[289] A. Albert, et al., [HAWC], “Long-term Spectra of the Blazars Mrk 421 and Mrk 501 at TeV Energies Seen by HAWC”, Astrophys. J. **929**, 125 (2022).

[290] F. J. Urena-Mena, et al., [HAWC], “Study of the long-term Very High Energy emission of the blazars 1ES 1215+3031 and VER J0521+211 with the HAWC gamma-ray observatory”, in Proceedings of 38th international cosmic ray conference — pos(icrc2023), Vol. 444 (2023), p. 807.

[291] R. Alfaro, et al., [HAWC], “Study of the Very High Energy Emission of M87 through its Broadband Spectral Energy Distribution”, Astrophys. J. **934**, 158 (2022).

[292] A. Albert, et al., [HAWC], “3HWC: The third HAWC catalog of very-high-energy gamma-ray sources”, Astrophys. J. **905**, 76 (2020).

[293] R. Gold, *An iterative unfolding method for response matrices* (Argonne National Laboratory ANL-6984, 1964).

[294] A. U. Abeysekara, et al., [HAWC], “Observation of anisotropy of tev cosmic rays with two years of HAWC”, Astrophys. J **865**, 57 (2018).

[295] A. U. Abeysekara, et al., [HAWC,IceCube], “All-sky measurement of the anisotropy of cosmic rays at 10 tev and mapping of the local interstellar magnetic field”, Astrophys. J. **871**, 96 (2019).

[296] A. Albert et al., “Search for gamma-ray spectral lines from dark matter annihilation in dwarf galaxies with the High-Altitude Water Cherenkov observatory”, Phys. Rev. D **101**, 103001 (2020).

[297] A. Albert et al., “Constraints on Lorentz invariance violation from HAWC observations of gamma rays above 100 TeV”, Phys. Rev. Lett. **124**, 131101 (2020).

[298] H. A. Ayala Solares et al., “The astrophysical multimessenger observatory network (amon): performance and science program”, Astroparticle Physics **114**, 68–76 (2020).

[299] J. Abraham, et al., [Pierre Auger], “Trigger and aperture of the surface detector array of the Pierre Auger Observatory”, Nuclear Instruments and Methods in Physics Research Section A: Accelerators, Spectrometers, Detectors and Associated Equipment **613**, 29–39 (2010).

[300] A. U. Abeysekara, et al., [VERITAS,FERMI-LAT,HAWC], “VERITAS and Fermi-LAT Observations of TeV Gamma-Ray Sources Discovered by HAWC in the 2HWC Catalog”, Astrophys. J. **866**, 24, 24 (2018).

[301] B. P. Abbot, et al., [LIGO, Virgo], “GWTC-1: a gravitational-wave transient catalog of compact binary mergers observed by LIGO and Virgo during the first and second observing runs”, Phys. Rev. X **9**, 031040 (2019).

[302] B. P. Abbot, et al., [LIGO, Virgo], “GW170608: Observation of a 19 solar-mass binary black hole coalescence”, Astrophys. J. Lett. **851**, L35 (2017).

[303] H. A. Ayala Solares and in behalf of the AMON Group, “The astrophysical multimessenger observatory network: a summary”, Journal of Physics: Conference Series **2429**, 012034 (2023).

[304] A. U. Abeysekara, et al., [HAWC], “Observation of the crab nebula with the hawc gamma-ray observatory”, Astrophys. J. **843**, 39 (2017).

[305] Hamamatsu Photonics K.K. and its affiliates, *Hamamatsu Photonics - Large Photocathode Area Photomultiplier Tubes Manual*, (2025) `https://hep.hamamatsu.com/content/dam/hamamatsu-photonics/sites/documents/99_SALES_LIBRARY/etd/LARGE_AREA_PMT_TPMH1376E.pdf`.

[306] C. Burgess, “Optical spectroscopy | detection devices”, in *Encyclopedia of analytical science (second edition)*, edited by P. Worsfold, A. Townshend, and C. Poole, Second Edition (Elsevier, Oxford, 2005), pp. 438–443.

[307] O. Heaviside, “The electromagnetic effect of moving point charge”, The Electrician **22**, 147–148 (1888).

[308] O. Heaviside, “On the electromagnetic effects due to the motion of electrification through a dielectric”, in *Electrical papers*, Vol. 2, Cambridge Library Collection - Technology (Cambridge University Press, 2011), pp. 504–518.

[309] P. A. Cherenkov, “Visible emission of clean liquids by action of gamma radiation”, Doklady Akademii Nauk SSSR **2** (1934).

[310] Y. Hu et al., “Cherenkov radiation control via self-accelerating wave-packets”, Scientific reports **7**, 8695 (2017).

[311] F. Nerling, J. Blümer, R. Engel, and M. Risse, “Universality of electron distributions in high-energy air showers—description of cherenkov light production”, Astroparticle Physics **24**, 421–437 (2006).

[312] A. U. Abeysekara, et al., [HAWC], “Data acquisition architecture and online processing system for the HAWC gamma-ray observatory”, Nucl. Instrum. Methods Phys. Res. Sect. A **888**, 138–146 (2018).

[313] HAWC Collaboration, *HAWCWiki*, (2017) `http://private.hawc-observatory.org/wiki/index.php/Main_Page`.

[314] Z. Hampel-Arias, “Cosmic ray observations at the TeV scale with the HAWC Observatory”, https://private.hawc-observatory.org/wiki/images/b/b8/HampelThesis.pdf, PhD thesis (University of Wisconsin-Madison, 2017).

[315] M. U. Nisa, “Constraining TeV-scale astrophysical foregrounds for dark matter searches with HAWC”, PhD thesis (University of Rochester, 2019).

[316] J. Pretz, *HAWC Saucy Platypus Crab Analysis: Results and Systematics Discussion*, HAWC internal documents, (2016) `https://private.hawc-observatory.org/hawc.umd.edu/internal/db/2333_07.pdf`.

[317] A. D. Panov, et al., [ATIC], “Elemental energy spectra of cosmic rays from the data of the ATIC-2 experiment”, Bull. Russ. Acad. Sci. Phys. **71**, 494–497 (2007).

[318] J. J. Beatty, J. Matthews, S. P. Wakely, et al., [Particle Data Group], “Review of Particle Physics”, Phys. Rev. D **98**, 030001 (2018).

[319] D. Heck et al., “CORSIKA: A Monte Carlo Code to Simulate Extensive Air Showers”, Forschungszentrum Karlsruhe **FZKA 6019**, 1–90 (1998).

[320] A. Ferrari, P. R. Sala, and J. Ranft, “FLUKA: a multi-particle transport code”, (2011).

[321] S. Ostapchenko, “QGSJET-II: towards reliable description of very high energy hadronic interactions”, Nucl. Phys. B (Proc. Suppl.) **151**, 143–146 (2006).

[322] S. Ostapchenko, “Nonlinear screening effects in high energy hadronic interactions”, Phys. Rev. D **74**, 014026 (2006).

[323] S. Agostinelli et al., “GEANT4 — a simulation toolkit”, **506**, 250–303 (2003).

[324] M. Aguilar et al., “Precision Measurement of the Helium Flux in Primary Cosmic Rays of Rigidities 1 . 9 GV to 3 TV with the Alpha Magnetic Spectrometer on the International Space Station”, **211101**, 1–9 (2015).

[325] M. Aguilar, et al., [AMS], “Precision measurement of the proton flux in primary cosmic rays from rigidity 1 GeV to 1.8 TeV with the Alpha Magnetic Spectrometer on the International Space Station”, Phys. Rev. Lett. **114**, 171103 (2015).

[326] Segev BenZvi, *Review of the SWEETS Project in AERIE*, HAWC internal documents, (2015) `https://private.hawc-observatory.org/hawc.umd.edu/internal/doc.php?id=2302`.

[327] John Pretz, Segev BenZvi, Zhixiang Ren, *Simulation weighting*, HAWC internal documents, (2013) `https://private.hawc-observatory.org/hawc.umd.edu/internal/doc.php?id=2302`.

[328] HAWC Collaboration, *Fits to direct measurements*, (2017) `https://private.hawc-observatory.org/wiki/index.php/Fits_to_Direct_Measurements`.

[329] A. D. Panov et al., “Elemental Energy Spectra of Cosmic Rays from the Data of the ATIC-2 Experiment”, Bull. Russ. Acad. Sci. Phys. **71**, 494–497 (2007).

[330] O. Adriani, et al., [CALET] (CALET Collaboration), “Direct Measurement of the Cosmic-Ray Carbon and Oxygen Spectra from 10 GeV/n to 2.2 TeV/n with the Calorimetric Electron Telescope on the International Space Station”, Phys. Rev. Lett. **125**, 251102 (2020).

[331] Y. Ohira, N. Kawanaka, and K. Ioka, “Cosmic-ray hardenings in light of AMS-02 data”, Phys. Rev. D **93**, 083001 (2016).

[332] E. Parizot et al., “Superbubbles and energetic particles in the Galaxy - I. Collective effects of particle acceleration”, A&A **424**, 747–760 (2004).

[333] N. Kawanaka and S. Yanagita, “Cosmic-ray lithium production at the nova eruptions followed by a type ia supernova”, Phys. Rev. Lett. **120**, 041103 (2018).

[334] V. I. Zatsepin and N. V. Sokolskaya, “Three component model of cosmic ray spectra from 10 GeV to 100 PeV ”, A&A **458**, 1–5 (2006).

[335] P. Lipari, “How well do we understand the properties of the Galactic cosmic ray accelerators and of cosmic ray propagation in the Galaxy ? A critical view.”, in Proceedings of 37th international cosmic ray conference — pos(icrc2021), Vol. 395 (2021), p. 169.

[336] D. Caprioli, C. Haggerty, and P. Blasi, “The Theory of Efficient Particle Acceleration at Shocks”, in Proceedings of 37th international cosmic ray conference — pos(icrc2021), Vol. 395 (2021), p. 482.

[337] Thoudam, Satyendra and Hörandel, Jörg R., “GeV-TeV cosmic-ray spectral anomaly as due to reacceleration by weak shocks in the Galaxy”, A&A **567**, A33 (2014).

[338] N. Tomassetti, “Origin of the spectral upturn in the cosmic-ray C/Fe and O/Fe ratios”, Phys. Rev. D **92**, 063001 (2015).

[339] G. Giacinti, M. KachelrieSS, and D. Semikoz, “Reconciling cosmic ray diffusion with galactic magnetic field models”, Journal of Cosmology and Astroparticle Physics **2018**, 051 (2018).

[340] C. Evoli, P. Blasi, G. Morlino, and R. Aloisio, “Origin of the cosmic ray galactic halo driven by advected turbulence and self-generated waves”, Phys. Rev. Lett. **121**, 021102 (2018).

[341] G. Bernard et al., “TeV cosmic-ray proton and helium spectra in the myriad model”, A&A **555**, A48 (2013).

[342] S. Recchia, S. Gabici, F. Aharonian, and J. Vink, “A local fading accelerator and the origin of TeV cosmic ray electrons”, in Proceedings of 37th international cosmic ray conference — pos(icrc2021), Vol. 395 (2021), p. 168.

[343] J. R. Hoerandel, “On the knee in the energy spectrum of cosmic rays”, Astroparticle Physics **19**, 193–220 (2003).

[344] H. Dembinski et al., “Data-driven model of the cosmic-ray flux and mass composition from 10 GeV to 10^{11} GeV”, arXiv:1711.11432 [astro-ph.HE] (2017).

[345] K. Asakimori, et al., [JACEE], “Cosmic-Ray Proton and Helium Spectra: Results from the JACEE Experiment”, Astrophys. J. **502**, 278–283 (1998).

[346] J. A. Morales-Soto, *The all-particle energy spectrum from 10 TeV to 1 PeV - CR group call, June 23th, 2020*, (2020) `https://private.hawc-observatory.org/wiki/images/0/09/Cr_call_june_23_JAMS_2.pdf`.

[347] V. Blobel, “Unfolding methods in particle physics”, Proceedings PHYSTAT 2011 Workshop on Statistical Issues Related to Discovery Claims in Search Experiments and Unfolding, 240–251 (2011).

[348] J. H. Friedman, “Data analysis techniques for high energy particle physics”, Proceedings of the 3rd CERN School of Computing, Norway (1974).

[349] R. Brun and F. Rademakers, “An object oriented data analysis framework”, Nucl. Instrum. Methods Phys. Res. Sect. A **389**, 81–86 (1997).

[350] G. Cowan, *Statistical data analysis* (Clarendon Press, Oxford, United States, 1998).

[351] T. Adye, *Corrected error calculation for iterative bayesian unfolding*, (2011) `https://hepunex.rl.ac.uk/adye/software/unfold/bayes_errors.pdf`.

[352] M. Schmelling, “The method of reduced cross-entropy a general approach to unfold probability distributions”, Nucl. Instrum. Methods Phys. Res. Sect. A **340**, 400–412 (1994).

[353] J. A. Morales-Soto, J. C. Arteaga-Velázquez, et al., [HAWC], *The all-particle energy spectrum of cosmic rays from 10 TeV to 1 PeV from HAWC data*, tech. rep. 2485 (HAWC internal documents, 2024).

[354] J. Pretz, *DAQSim - Code and Parameter Tuning*, HAWC internal documents, (2018) `https://private.hawc-observatory.org/hawc.umd.edu/internal/doc.php?id=2397`.

[355] S. V. Ter-Antonyan and L. Haroyan, "About EAS size spectra and primary energy spectra in the knee region", arXiv preprint hep-ex/0003006 (2000).

[356] F. James, "MINUIT Reference Manual", CERN Program Library Long Writeup D506 (1994).

[357] P. Zyla et al. (Particle Data Group), "Review of Particle Physics", PTEP **2020**, 083C01 (2020).

[358] Z. Hampel-Arias, "Cosmic ray observations at the TeV scale with the HAWC observatory", PhD thesis, PhD thesis (University of Wisconsin-Madison, 2017).

[359] G. Cowan, "Monte Carlo Techniques", in M. Tanabashi et al. (Particle Data Group), Review of particle physics, Phys.Rev. D **98**, 030001 (2019).

[360] P. Abreuand, et al., [Pierre Auger], "The energy spectrum of cosmic rays beyond the turn-down around 10^{17} eV as measured with the surface detector of the Pierre Auger Observatory", The European Physical Journal C **81**, 1–25 (2021).

[361] P. Montini, et al., [ARGO-YBJ], "The bending of the proton plus helium flux in primary cosmic rays measured by the ARGO-YBJ experiment in the energy range from 20 TeV to 5 PeV", arXiv:1608.01389 [hep-ex] (2016).

[362] A. Surdo, "Observation of a knee in the cosmic ray p+He energy spectrum below 1 PeV with the ARGO-YBJ experiment", in Proceedings of the european physical society conference on high energy physics — pos(eps-hep2015), Vol. 234 (2016), p. 402.

[363] M. Kachelrieß, A. Neronov, and D. V. Semikoz, "Cosmic ray signatures of a 2–3 Myr old local supernova", Phys. Rev. D **97**, 063011 (2018).

[364] V. I. Zatsepin and N. V. Sokolskaya, "Three component model of cosmic ray spectra from 10 GeV to 100 PeV", Astron. Astrophys. **458**, 1 (2006).

[365] T. K. Gaisser, T. Stanev, and S. Tilav, "Cosmic ray energy spectrum from measurements of air showers", Front. Phys. **8**, 748 (2013).

[366] M. Malkov, P. Diamond, M. Cao, and I. Moskalenko, "On why the 10 TeV cosmic ray bump originates in the local interstellar medium", in Proc. of 38th International Cosmic Ray Conference — PoS(ICRC2023), 143 (2023).

[367] F. Alemanno, et. al., [DAMPE], "Measurement of the cosmic $p+$He energy spectrum from 50 GeV to 0.5 PeV with the DAMPE space mission", Phys. Rev. D **109**, L121101 (2024).

[368] J. A. Morales-Soto and J. C. Arteaga-Velázquez, "HAWC measurements on the total energy spectrum of cosmic rays", in Proc. of 38th International Cosmic Ray Conference — PoS(ICRC2023), 364 (2023).

[369] J. A. Morales-Soto and J. C. Arteaga-Velázquez, "The all-particle energy spectrum of cosmic rays from 10 TeV to 1 PeV measured with HAWC", in Scipost physics proceedings, 13 (2023), p. 039.

[370] J. A. Morales-Soto and J. C. Arteaga-Velázquez, "The all-particle cosmic ray energy spectrum measured with HAWC", in Proc. of 37th International Cosmic Ray Conference — PoS(ICRC2021), 330 (2021).

[371] H. Schoorlemmer, "A next-generation ground-based wide field-of-view gamma-ray observatory in the southern hemisphere", in Proceedings of 36th international cosmic ray conference — pos(icrc2019), Vol. 358 (2019), p. 785.

[372] D. Alvarado, et. al., [HAWC], "Cosmic-ray energy reconstruction using machine learning techniques", in Proceedings of 38th international cosmic ray conference — pos(icrc2023), Vol. 444 (2023), p. 402.

[373] J.C Díaz-Vélez, et al., [HAWC], *"HAWC Observations of the Spectrum, Composition and Anisotropy of Cosmic Rays Below the Knee" in SuGAR: Searching for the Sources of Galactic Cosmic Rays (SuGAR 2024)*, (2024) `https://events.icecube.wisc.edu/event/183/contributions/10594/`.

[374] Pengxiong Ma, et al., [DAMPE], *"The latest results from the DAMPE experiment" in 13th Cosmic-Ray International Studies and Multi-messenger Astroparticle Conference (CRIS-MAC 2024)*, (2024) `https://agenda.infn.it/event/36661/contributions/230433/attachments/121854/177754/DAMPE_CRIS-MAC_2024_PengxiongMa.pdf`.

[375] C. Perrina, et al., [HERD], "Attaining the PeV frontier of the cosmic ray spectrum in space with HERD", EPJ Web Conf. **280**, 01008 (2023).

[376] C. E. Shannon, "A mathematical theory of communication", The Bell system technical journal **27**, 379–423 (1948).

[377] E. T. Jaynes, "Prior probabilities", IEEE Trans. Syst. Sci. Cyb. **4**, 227–241 (1968).

[378] F. Spano, "Unfolding in particle physics: a window on solving inverse problems", EPJ Web Conf. **55**, 03002 (2013).

[379] J. A. Morales-Soto and J. C. Arteaga-Velázquez, "The all-particle cosmic ray energy spectrum measured with HAWC in the TeV region", in Proc. of 27th European Cosmic Ray Symposium — PoS(ECRS), 087 (2022).

Jorge Antonio Morales Soto

Espectro total de energía de rayos cósmicos medido con el observatorio HAWC.pdf

Universidad Michoacana de San Nicolás de Hidalgo

Detalles del documento

Identificador de la entrega

trn:oid:::3117:478793163

Fecha de entrega

6 ago 2025, 9:25 a.m. GMT-6

Fecha de descarga

6 ago 2025, 9:30 a.m. GMT-6

Nombre de archivo

Espectro total de energía de rayos cósmicos medido con el observatorio HAWC.pdf

Tamaño de archivo

7.3 MB

147 Páginas

52.431 Palabras

273.793 Caracteres

27% Similitud general

El total combinado de todas las coincidencias, incluidas las fuentes superpuestas, para ca...

Grupos de coincidencias

976 Sin cita o referencia 19%
Coincidencias sin una citación ni comillas en el texto

9 Faltan citas 0%
Coincidencias que siguen siendo muy similar al material fuente

232 Falta referencia 8%
Las coincidencias tienen comillas, pero no una citación correcta en el texto

0 Con comillas y referencia 0%
Coincidencias de citación en el texto, pero sin comillas

Fuentes principales

21%	Fuentes de Internet
25%	Publicaciones
0%	Trabajos entregados (trabajos del estudiante)

Marcas de integridad

N.º de alerta de integridad para revisión

Caracteres reemplazados
118 caracteres sospechosos en N.º de páginas
Las letras son intercambiadas por caracteres similares de otro alfabeto.

Los algoritmos de nuestro sistema analizan un documento en profundidad para buscar inconsistencias que permitirían distinguirlo de una entrega normal. Si advertimos algo extraño, lo marcamos como una alerta para que pueda revisarlo.

Una marca de alerta no es necesariamente un indicador de problemas. Sin embargo, recomendamos que preste atención y la revise.

Formato de Declaración de Originalidad y Uso de Inteligencia Artificial

Coordinación General de Estudios de Posgrado
Universidad Michoacana de San Nicolás de Hidalgo

A quien corresponda,

Por este medio, quien abajo firma, bajo protesta de decir verdad, declara lo siguiente:

- Que presenta para revisión de originalidad el manuscrito cuyos detalles se especifican abajo.
- Que todas las fuentes consultadas para la elaboración del manuscrito están debidamente identificadas dentro del cuerpo del texto, e incluidas en la lista de referencias.
- Que, en caso de haber usado un sistema de inteligencia artificial, en cualquier etapa del desarrollo de su trabajo, lo ha especificado en la tabla que se encuentra en este documento.
- Que conoce la normativa de la Universidad Michoacana de San Nicolás de Hidalgo, en particular los Incisos IX y XII del artículo 85, y los artículos 88 y 101 del Estatuto Universitario de la UMSNH, además del transitorio tercero del Reglamento General para los Estudios de Posgrado de la UMSNH.

Datos del manuscrito que se presenta a revisión		
Programa educativo	Doctorado en Ciencias en el área de Física	
Título del trabajo	Espectro total de energía de rayos cósmicos medido con el observatorio HAWC	
	Nombre texto	**Correo electrónico**
Autor/es	Jorge Antonio Morales Soto	jorge.morales@umich.mx
Director	Juan Carlos Artega Velázquez	juan.arteaga@umich.mx
Codirector		
Coordinador del programa	Umberto Cotti Gollini	doc.ciencias.fisica@umich.mx

Uso de Inteligencia Artificial		
Rubro	**Uso (sí/no)**	**Descripción**
Asistencia en la redacción	no	

Formato de Declaración de Originalidad y Uso de Inteligencia Artificial

Coordinación General de Estudios de Posgrado
Universidad Michoacana de San Nicolás de Hidalgo

CGEP
UMSNH

Uso de Inteligencia Artificial		
Rubro	**Uso (sí/no)**	**Descripción**
Traducción al español	no	
Traducción a otra lengua	no	
Revisión y corrección de estilo	no	
Análisis de datos	no	
Búsqueda y organización de información	no	
Formateo de las referencias bibliográficas	no	
Generación de contenido multimedia	no	
Otro	no	

Datos del solicitante	
Nombre y firma	[redacted]
Lugar y fecha	Morelia, Michoacán. A 4 de Agosto, 2025.